

UNIVERSITY OF ONTARIO INSTITUTE OF TECHNOLOGY

**Design of a Novel Ferrite Core based Highly Efficient
Wireless Resonant Inductive Power Transfer System**

by

Vamsi Krishna Pathipati

A THESIS

SUBMITTED TO THE FACULTY OF GRADUATE STUDIES

IN PARTIAL FULFILMENT OF THE REQUIREMENTS FOR THE

DEGREE OF MASTER OF APPLIED SCIENCE (M.A.Sc.)

GRADUATE PROGRAM IN ELECTRICAL AND COMPUTER ENGINEERING

OSHAWA, ONTARIO

MARCH, 2016

© Vamsi Krishna Pathipati, 2016

Abstract

Electric Vehicles (EVs) are changing the face of global transportation due to no tail pipe emissions and higher drive train efficiencies. Promising technological advancements in the areas of battery technologies, power electronics and motor drives is making EVs outnumber internal combustion engine (ICE) vehicles a reality. EVs use rechargeable batteries on-board the vehicles similar to a fuel tank in the ICE vehicles. These on-board batteries should be regularly charged similar to refueling an ICE vehicles. EV charging using a plug-in cable from the wall socket, where the medium of charging is through conducting cable is called conductive charging. Conductive charging technologies are predominantly being used in the present day EV market. To avoid handling of cables and associated potential hazards, wireless charging techniques are extensively investigated by the researchers around the globe. Wireless charging of an electric vehicle using resonant inductive power transfer is the topic-of-interest of this thesis.

The core component of the WIPT system is the magnetic power transfer system. Wireless charging using inductive power transfer utilizes high frequency magnetic field to transfer power from primary to secondary over a large airgap. Due to larger airgap, there exists a high leakage flux that produces magnetic radiation. In this thesis an approach to use ferrite core geometries and winding configurations to improve effectiveness for electric vehicle wireless charging systems using wireless resonant inductive power transfer (WRIPT) is explored. Using ferrite magnetic cores improves the efficiency of IPT and magnetic resonance based IPT systems, and can reduce unwanted stray magnetic radiation in addition to improving coupling efficiency. Performance of different ferrite geometries and various winding configurations are explored and their performance is studied using JMAG[®] FEA analysis. Experimental results are shown for each core and winding configuration. From the analysis and the experimental results, it is seen that the U-U core based ferrite geometry system with windings close to the air gap provides the most effective coupling in larger airgap WRIPT applications. A 1.0 kW, 10 cm prototype is developed and experimental results are presented for various operating conditions. Electrical model for this novel WRIPT system is developed and the simulation results very closely match with experimental results. It is seen that the designed system can transfer power with 94.7% DC to DC efficiency over 10 cm airgap. It is also experimentally verified that this system operates

with reduced magnetic radiation without an extra shielding design. Various control methods are presented to achieve required system voltage gain for charging an industrial electric vehicle (IEV) with 48 VDC battery pack from a 400 VDC DC link input. The efficiency of IEV charging using SS and SP compensated WRIPT system is also presented.

The designed novel magnetic power transfer system can be used for EV wireless charging application as well as in any industrial wireless power transfer applications.

ACKNOWLEDGEMENT

I would like to express my sincere gratitude and deepest appreciation to my supervisor, Dr. Sheldon S. Williamson for his continuous guidance, commitment and support throughout the course of this research. Also for his unconditional brotherly love in making me feel home always. Secondly, I would like to sincerely thank Mr. Nicholas Dohmeier and Mr. Chris Botting from Delta-Q Technologies, Burnaby, BC for being very supportive industrial partners. A special appreciation to Mr. Dohmeier for his throughout advices on the approach and project progress. Also I would like to thank Dr. Najath Abdul Azeez, Post-doctoral Fellow at UOIT for his timely advices and continuous support with technical discussions and helping me think on the technical hurdles and come up with solution ideas in this work.

I also thank NSERC Canada, and Dr. Williamson for funding this project work. A special thanks for Mr. Jarvis Asamoah, Jr. from Electro-Meters for his timely support on shipping measuring equipment. Also, a special appreciation and thanks to Mr. Raymond LaForge (my Canadian landlord) for making me never feel like I am away from my home. I would also like to thank UOIT for the facilities and my fellow lab mates at ASSET lab and STEER group members for their support and help in various aspects after coming to Canada.

Lastly, I would like to thank my family and friends for their continuous support and encouragement.

Dedicated to

All the wonderful people with beautiful and brave hearts in the world like my mother.

Table of Contents

Abstract.....	ii
Table of Contents	vi
List of Figures and Illustrations	viii
List of Tables	xii
List of Abbreviations	xiii
Chapter-1 Introduction	1
1.1 Contact-based/plugged/conductive Charging	2
1.1.1. Advantages and disadvantages of wired/conductive charging	4
1.2 Wireless Power Transfer (WPT)	4
1.2.1 History of wireless power transfer	5
1.2.2 Overview of the WPT	6
1.2.2.1 Commercialization of wireless power transfer.....	6
1.2.2.2 Advantages of wireless charging or power transfer	9
1.2.1 Wireless charging of electric transportation.....	10
1.2.1.1 Wireless charging system of an electric vehicle.....	11
1.3 Research Objectives and Contributions	15
1.4 Organization of Thesis.....	16
Chapter-2 Working principle of inductive power transfer system	17
2.1 Theory of Electromagnetics	17
2.2 Loosely coupled Inductive systems.....	20
2.3 Need for High Frequency in WIPT operation.....	23
2.2.1 Effects of high frequency operation and use of Litz wires.....	23
2.3. Need for Compensation	24
2.3.1 SS Compensated WRIPT System.....	27
2.3.1 SP Compensated WIPT System	29
2.1 Power Electronics Requirement	32
2.1.1 Analysis of the Class-D inverter circuit.....	34
2.1.2 Working of Class-D converter under various operating scenarios.....	35
Chapter-3 Design of a novel magnetic power transfer system	39
3.1 Introduction.....	39
3.2 State of the art MPTS	39
3.3 Ferrite core based WIPT options	42
3.3.1 Reluctance model of the core combinations	44
3.3.2. Influence of primary and secondary cores on self-inductances	45
3.3.3 FEA and signal power experimentation for identifying the best core combination for WIPT application	46

(1) <i>E-E core combination</i>	46
(2) <i>E-I core combination</i>	51
(3) <i>Planar E-E core combination</i>	53
(4) <i>ETD-ETD core combination</i>	55
(5) <i>I-I core combination</i>	55
(6) <i>U-I core combination</i>	57
(7) <i>U-U core combination</i>	59
3.3.4 Further investigations on the potential candidates identified in section 3.33.	60
3.3.4.1 Design criteria for lower leakage inductance and higher power transfer efficiency.	62
(1) <i>U-I core with multiple windings in parallel on U core central limb</i>	62
(2) <i>U-U core with multiple windings in parallel on primary and series on secondary, both placed on central limb</i>	64
(3) <i>U-I core with multiple windings in series on U core central limb</i>	65
(4) <i>U-U core with multiple windings in parallel connected on both cores on central limb</i>	67
(5) <i>U-U core with multiple windings in series connected on both cores on central limb</i>	68
(6) <i>U-U core with multiple windings in series connected on both cores on side limb</i>	69
(7) <i>U-I core with multiple windings in series on U core side limbs</i>	71
(8) <i>U-I core with multiple windings in parallel on U core side limbs</i>	72
(9) <i>U-U core with multiple windings in parallel connected on both cores on side limbs</i>	73
(10) <i>U-U core with multiple windings in parallel on primary and series on secondary on side limbs</i>	75
3.3.5 Conclusions and design recommendations for 1.0 KW, 10 cm system.....	76
 Chapter-5 Control of Class-D Amplifier in a Series-Parallel Compensated WRIPT System for Achieving Unity Voltage Gain	99
5.1 Fixed Frequency (ω_0) Firing Angle Control.....	100
5.1.1. α -DB control.....	100
5.1.2. α -DB- α control	102
5.2. Results and Comparison	103
5.3 Conclusion	104
 Chapter-6 Wireless charging of an IEV.....	105
 Chapter-7 Conclusion and Future Work.....	107
Conclusion	107
Future Work.....	108
 References	110
 Annexure-I Power Loss Calculation	117

List of Figures and Illustrations

Fig. 1.1 Electric Vehicle System Model -----	1
Fig. 1.2 Contact based EV charging-----	2
Fig. 1.3 On-board conductive charger topologies for an EV/PHEV-----	3
Fig. 1.4 Examples of commercially available wireless charging options for consumer electronics-----	8
Fig. 1.5 (a) IPT based wireless charging system (b) CPT based wireless charging system-----	11
Fig. 1.6 EV wireless charging using inductive power transfer-----	12
Fig. 2.1 Coupled magnetic coils-----	17
Fig. 2.2 Electrical Transformer-----	18
Fig. 2.3 Wireless Inductive system separated by an airgap “a”-----	19
Fig. 2.4 Electrical representation of the WIPT system-----	19
Fig. 2.5 Equivalent circuit model of the WIPT system-----	20
Fig. 2.6 4 basic compensation topologies of a WIPT system -----	23
Fig. 2.7 SS WIPT system (a) System circuit (b) Equivalent circuit model-----	24
Fig. 2.8 Voltage gain characteristics of the SS WIPT system-----	26
Fig. 2.9 SP WIPT system (a) System circuit (b) Equivalent circuit model-----	26
Fig. 2.10 Voltage gain characteristics of the SP WIPT system-----	28
Fig. 2.11 (a) Full bridge inverter circuit (b) Half bridge inverter circuit-----	30
Fig. 12 (a) Full-bridge inverter output voltage (b) half-bridge inverter output voltage-----	30
Fig. 2.13 (a) WIPT primary fed with a Class-D amplifier (b) Class-D inverter output voltage---	31
Fig. 2.14 Class-D circuit operating at $f_s=f_r$ -----	32
Fig. 2.15 Class-D circuit operation when $f_s>f_r$ -----	33
Fig. 2.16 Class-D circuit operation when $f_s<f_r$ -----	34
Fig. 3.1 Top view of the Circular/Spiral Coil -----	36
Fig. 3.2 (a) Double D coil topology (b) Unipolar rectangular coil (c) Unipolar square coil-----	37
Fig. 3.3 Off-the-shelf available popular ferrite cores-----	39
Fig. 3.4 Core structure combinations for WIPT performance study-----	39
Fig. 3.5 Winding with a core with airgap l_g (a) physical model (b) magnetic circuit model-----	40
Fig. 3.6 Reluctance paths for a E-E core based WIPT system-----	41

Fig. 3.7 E-E core WIPT system with various winding configurations-----	42
Fig. 3.8 FEA results for E-E core WIPT system with horizontal winding on the central limb at 1.5 cm airgap-----	43
Fig. 3.9 E-E experimental core with horizontal winding on central limb-----	44
Fig. 3.12 E-E experimental core with vertical winding on central limb-----	45
Fig. 3.17 E-E experimental core with horizontal winding on side limbs-----	46
Fig. 3.18 E-E experimental core with quadrature winding on central limb-----	46
Fig. 3.21 E-I core WIPT system-----	47
Fig. 3.22 FEA of E-I core WIPT system at 1.5 cm airgap-----	48
Fig. 3.23 E-E experimental core with quadrature winding on central limb-----	48
Fig. 3.26 Planar E-E core WIPT system-----	49
Fig. 3.27 FEA results for the Planar E-E core WIPT system at 1.5 cm airgap-----	50
Fig. 3.28 Planar E-E experimental core with vertical winding on window area-----	50
Fig. 3.31 I-I Core WIPT system-----	51
Fig. 3.32 FEA results for the I-I core WIPT system at 1.5 cm airgap-----	51
Fig. 3.33 I-I experimental cores with horizontal winding on window area-----	52
Fig. 3.36 U-I Core WIPT system-----	53
Fig. 3.37 FEA results of the U-I core WIPT system at 1.5 cm airgap-----	53
Fig. 3.38 U-I experimental core with horizontal winding-----	54
Fig. 3.41 U-U core WIPT system-----	55
Fig. 3.42 FEA results for U-U core WIPT systems-----	55
Fig. 3.43 U-I experimental core with horizontal winding-----	55
Fig. 3.46 U-U and U-I WIPT system combinations-----	57
Fig. 3.47 FEA results for the U-I WIPT system with split winding on U core connected in parallel-----	58
Fig. 3.48 U-I experimental core with parallel split winding on U-core central limb-----	59
Fig. 3.51 FEA results for the U-U WIPT system with parallel primary and series secondary split windings on U core-----	60
Fig. 3.52 U-U experimental core with split parallel and series windings-----	60
Fig. 3.55 FEA results for the U-I WIPT system with split winding on U core connected in series-----	61

Fig. 3.56 U-I experimental core with series split winding on U-core central limb-----	61
Fig. 3.59 FEA results for the U-U WIPT system with parallel primary and secondary split windings on U core-----	62
Fig. 3.60 U-U experimental core with split parallel windings-----	63
Fig. 3.63 FEA results for the U-U WIPT system with series primary and secondary split windings on U core-----	63
Fig. 3.64 U-U experimental core with split series windings-----	64
Fig. 3.67 FEA results for the U-U WIPT system with series primary and secondary split windings on U core-----	65
Fig. 3.68 U-U experimental core with split series windings on side limbs-----	65
Fig 3.71 FEA results for the U-I WIPT system with split winding on U core connected in series-- -----	66
Fig. 3.72 U-I experimental core with series split winding on U-core side limbs-----	67
Fig 3.75 FEA results for the U-I WIPT system with split winding on U core connected in series-- -----	67
Fig. 3.76 U-I experimental core with parallel split winding on U-core side limbs-----	68
Fig. 3.79 FEA results for the U-U WIPT system with parallel primary and secondary split windings on U core-----	69
Fig. 3.80 U-U experimental core with split parallel windings on side limbs-----	69
Fig. 3.83 FEA results for the U-U WIPT system with parallel primary and series secondary split windings on U core-----	70
Fig. 3.84 U-U experimental core with split parallel and series windings-----	70
Fig. 4.1 WIPT experimental block diagram-----	72
Fig. 4.2 Ferroxcube® 3F3 ferrite material properties-----	73
Fig. 4.3. Final U-core system design-----	73
Fig. 4.4 FEA results for U-U core-----	76
Fig. 4.5 FEA results for U-U core with split winding connected in parallel on primary and series on secondary-----	78
Fig. 4.6 Equivalent circuit model for $L_{pri} = L_{sec}$ -----	79
Fig.4.7 Equivalent circuit model for $L_{pri} = L_{sec}$ -----	79
Fig. 4.8 Final build of core with windings-----	80

Fig. 4.9 Electrical model and Simulation circuit-----	81
Fig. 4.10 Simulation Results for $L_{pri} = L_{sec}$ and @ 10 cm airgap without zero horizontal misalignment-----	82
Fig. 4.11 Simulation Results for $L_{pri} > L_{sec}$ and @ 10 cm airgap without zero horizontal misalignment-----	83
Fig. 4.12. Experimental circuit for WIPT system-----	84
Fig. 4.13. Experimental setup for $L_{pri} = L_{sec}$ and @ 10 cm airgap without zero horizontal misalignment-----	84
Fig. 4.14 Experimental Results for for $L_{pri} = L_{sec}$ and @ 10 cm airgap without zero horizontal misalignment-----	86
Fig. 4.15 Experimental results for for $L_{pri} > L_{sec}$ and @ 10 cm airgap without zero horizontal misalignment-----	88
Fig. 4.16 (a) Trend of mutual inductance with respect to airgap for both voltage gain systems (b) Power transfer vs airgap plot (c) DC to DC power transfer efficiency with variation in airgap----- -----	89
Fig. 4.17 Magnetic radiation measurement axis-----	91
Fig. 4.18 Magnetic flux density in XYZ direction from point O-----	91
Fig. 5.1 SP Voltage gain characteristics-----	93
Fig. 5.2 α -DB control operating waveforms-----	95
Fig. 5.3 α -DB- α control operating waveforms-----	96
Fig. 5.4 Power transfer efficiency plot with different control schemes-----	98
Fig. 6.1 Efficiency vs Load power for IEV charging-----	100

List of Tables

Table-I Standard EV charging levels-----	3
Table-3.1 E-E system specifications with horizontal winding on central limb-----	44
Table-3.2 E-E system specifications with vertical winding on central limb-----	45
Table-3.3 E-E system specifications with horizontal winding on side limbs-----	46
Table-3.4 E-E system specifications with quadrature winding on central limb-----	46
Table-3.5 E-I system specifications with horizontal winding on central limb-----	48
Table-3.6 Planar E-E system specifications with vertical winding on window area-----	50
Table-3.7 I-I core system specifications with horizontal winding on window area-----	52
Table-3.8 U-I core system specifications with horizontal winding on window area-----	54
Table-3.9 U-U core system specifications with horizontal winding on window area-----	56
Table-3.10 U-I core system specifications with split winding on U-core connected in parallel--	59
Table-3.11 U-U core system specifications with split parallel and series windings-----	60
Table-3.12 U-I core system specifications with split winding on U-core connected in series----	61
Table-3.13 U-U core system specifications with split parallel windings-----	63
Table-3.14 U-U core system specifications with split series windings-----	64
Table-3.15 U-U core system specifications with split series windings on side limbs-----	65
Table-3.16 U-I core system specifications with split winding on U-core connected in series----	67
Table-3.17 U-I core system specifications with split winding on U-core connected in parallel--	68
Table-3.17 U-U core system specifications with split series windings on side limbs-----	69
Table-3.18 U-U core system specifications with split parallel and series windings-----	70
Table-4.2 System design specifications-----	74
Table-4.3 Inductance design parameters-----	78
Table-4.4 Components used in experimental setup-----	80
Table-5.1 System design specifications-----	94
Table-5.2 Simulation results for achieving unity voltage gain-----	97
Table-6.1 Specification for IEV charging using WIPT-----	100

List of Abbreviations

EV	Electric Vehicle
PHEV	Plug-in Hybrid Electric Vehicle
ICE	Internal Combustion Engine
IEV	Industrial Electric Vehicle
EVSE	Electric Vehicle Supply Equipment
WIPT	Wireless Inductive Power Transfer
WRIPT	Wireless Resonant inductive Power Transfer
SoC	State of Charge
WPT	Wireless Power Transfer
MPTS	Magnetic Power Transfer System
ZVS	Zero Voltage Switching
ZCS	Zero Current Switching
APFC	Active Power Factor Correction
FFT	Fast Fourier Transform

Chapter-1 Introduction

Electric vehicles (EVs) are changing the face of global transportation. They are turning out to be the viable transportation solution due to zero tail pipe emissions, are more efficient, less noisy, and require very less maintenance compared to internal combustion engine (ICE) vehicles [1], [2]. EVs and PHEVs have rechargeable batteries on-board the vehicle as shown in the Fig. 1.1. This battery pack acts as an energy source responsible for the vehicle propulsion. Battery pack of an electric vehicle has to be recharged at regular intervals of time depending on the usage and the state-of-charge (SoC). Recharging of the batteries in an EV is similar to refueling of an ICE vehicle.

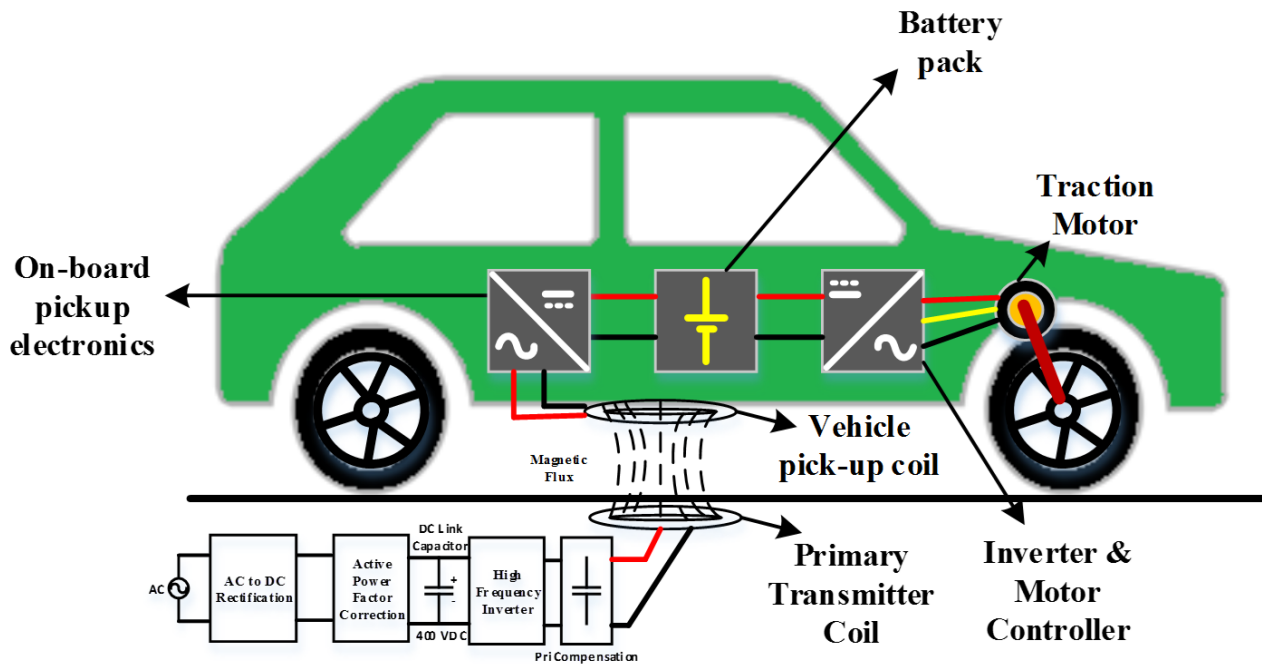


Fig. 1.1 Electric Vehicle System Model

Battery pack of an EV or PHEV is charged using an on-board or off-board charging equipment. On-board charging can be done using a contact based [3]–[7] or contact less [7]–[12] charging. An electric cable is used in charging the vehicle in the plug-in/contact charging method and in the contact less method, charging is done using wireless power transmitters and receivers avoiding the use of charging current carrying conductors.

1.1 Contact-based/plugged/conductive Charging

Plugged charging basically looks as shown in the Fig. 1.2 below. Depending on the charging c-rate level of the battery, there are two ways to charge the vehicle in the plugged charging method namely normal charging and fast charging.

In normal charging method, AC wall power from grid is supplied to the vehicle on-board charger which rectifies and charges the battery pack. This method charges EV in slower charge rates due to the limitation of on-board vehicle charger hardware and domestic wall socket power. The usual c-rates in normal charging is 0.2 C to 0.3 C.

On the other hand, in fast charging we use an off-board charging equipment that supplies rectified and controlled DC power that charges the vehicle battery pack. Here as the rectifier and charger hardware is off-board, it is possible to charge the vehicle at higher charge rates. The usual c-rates for fast charging are $>1C$. There will not be any power electronic hardware involved on-board the vehicle in this method of charging,

Basic system for the plugged charging is as shown in the Fig. 1.2. Here the electric vehicle supply equipment (EVSE) can be either normal charging supply equipment or off-board rectifier charger for fast charging.

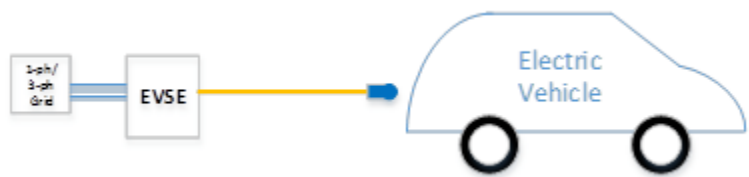


Fig. 1.2 Contact based EV charging

Lithium batteries are widely used in electric vehicle application. For safety and reliability reasons, these batteries should be charged and discharged in a very controlled fashion. There are several EV charging standards and communication protocols developed across the globe for achieving safe and human friendly charging. The EV charging standards across the globe for normal charging are;

Normal Charging Standards

- a) SAE J1772 (Type-1) – Predominant in the North America and Japan
- b) IEC 61851-1 (Type-2) - Predominant in the Europe

c) Chinese GB standards - Predominant in the Asian markets

Fast Charging Standards

- a) CHAdeMO – Most commonly used fast charging standards across the globe
- b) SAE J1772 (Type-3 and Combo) – Predominant in the North America and Japan
- c) IEC 61851-1 (Combo) - Predominant in the Europe
- d) Chinese GB standards - Predominant in the Asian markets

On a generic level, the EV conductive charging is broadly classified as shown in Table-I

Table-I Standard EV charging levels

Level	Voltage Rating	Phase	Power Level	Charging Type
Level 1	120 Vac	1-phase	1.6 kW	Normal Charging
Level 2	240 Vac	1- and split-phase	3.3 kW	
Level 3	208/415 Vac	3-phase	>10 kW (depending on vehicle can even go upwards of 100 kW)	Fast Charging

In the contact based on-board charging there exists an on-board power electronics hardware as shown in Fig. 1.1, that converts the grid supplied AC power into the controlled and regulated battery required DC power. Typical on-board charger block diagram is as shown in the Fig. 1.3. EV/PHEV charging regulations impose designers to use isolated charger topologies for the user safety if the charger input voltage is $>25 V_{rms}$ or $>60 V_{peak}$. There are two basic isolated topologies for a charger viz. hard-switched topology and soft-switched topology. Soft switching topologies work on basic principles of electric resonance, using reactive components for achieving resonance.

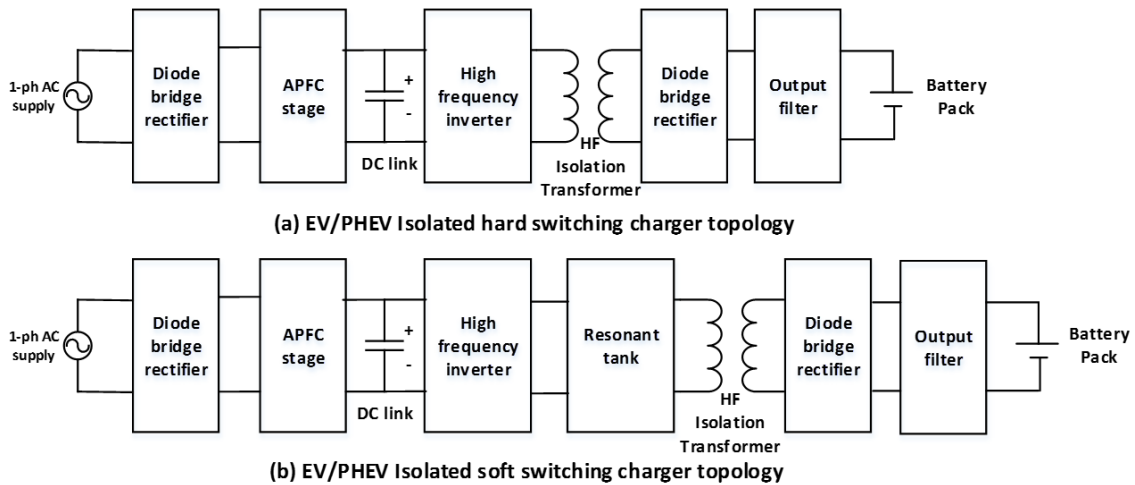


Fig. 1.3 On-board conductive charger topologies for an EV/PHEV

Soft switching topologies have an ability to operate at zero voltage switching (ZVS) and zero current switching (ZCS), which can reduce EMI issues at the source level in the design. Also they are very advantageous as they have very less switching losses thereby higher operating efficiencies. Due to reduced switching losses, they can be designed for higher operating frequencies which makes the design more power dense.

1.1.1. Advantages and disadvantages of wired/conductive charging

Advantages	Disadvantages
<ul style="list-style-type: none"> 1) Established and widely used charging technology. 2) Due to being in existence for long time, have developed highly efficient, reliable charging systems. 3) Less expensive. 4) Can be designed for any power level ranging from slow to fast charging. 	<ul style="list-style-type: none"> 1) Use of cables and human intervention while plugging and unplugging from charging. 2) Cable and connectors can be heavy for high power/fast charging. 3) Cables/connector damage while handling or due to rodent bites. 4) Possibility of unauthorised charging interruption when plugged in for charging at public places. 5) Possibility of cable or charging equipment theft at public places. 6) Electric hazard when operating in rainy or humid environment. 7) Damage to equipment and infrastructure if vehicle roll over or user drives when plugged in for charging.

1.2 Wireless Power Transfer (WPT)

Though the conductive/wired charging technology is very efficient and fully established, researchers are exploring wireless charging of electric vehicles to overcome the disadvantages of wired charging and increasing the charging comfort. Wireless power transfer is possible using

many technologies such as radio frequency, micro waves, electromagnetic, electro static, etc. Since early 19th century till date there has been many developments and commercialization of wireless power transfer technologies.

1.2.1 History of wireless power transfer

André-Marie Ampère developed Ampere's law that demonstrates the electric current producing a magnetic field in 1820. This was the triggering point to start the development of electromagnetic technologies. In 1831, Michael Faraday and Joseph Henry discovered electromagnetic induction. The classical electromagnetic theory was later formulated by James Clerk Maxwell. This combined all the previous observations, experiments and equations of electricity, magnetism and optics into a consistent theory [12]. This theory was later refined to the four famous equations known as Maxwell's equations by Oliver Heaviside [13].

In 1891, for the first time, Nikola Tesla demonstrated the wireless transmission of energy. Many revolutionary developments of Tesla in the field of electromagnetism were based on the Michael Faraday's theories of electromagnetic technology [14].

In the early 19th century wireless power transmission was researched for an alternative to transmission line power distribution. The theory of wireless power transmission was studied by both Heinrich Hertz and Nicola Tesla. In 1899, Nicola Tesla demonstrated wireless power transfer using radio waves by powering the fluorescent lamps 25 miles away from the power source [15].

The modern development of wireless transmission of microwave power transmission was contribution by William C. Brown. During 1964, he demonstrated powering a helicopter using microwave transmission using a "rectenna" he invented that converts microwaves into DC current.

In early 1980s, NASA scientists developed a thin film plastic rectenna using pcb technology [16] which weighted less than one-tenth of the then state of the art rectenna. This advancements led to the development of the the Stationary High Altitude Relay Platform (SHARP) technology that was used to develop unmanned aircrafts using microwave power transmission.

Recently wireless power transfer is researched extensively due to the scope of technology to be expanded in many different areas. Wireless charging of an electric vehicle has been considered as an extremely viable option for the EV charging due to their inherent advantages. Wireless charging

can be made very efficiency with the advantage of the present day semiconductor technology advancements.

1.2.2 Overview of the WPT

It is very confusing and at times frustrating to use wired devices like charging cables for various consumer electronics like cell phones, laptops, iPads, etc. Especially for a travelling individual, it is very painful to differentiate the different charging cables; in such situations, wireless charging is very advantageous. In the today's market, there are many electrical and electronics products and applications that support the wireless charging/wireless power transfer. At the top level, wireless power transfer can be classified as far-field wireless power transfer and near-field wireless power transfer systems.

Far-field systems utilizes radiative power transfer technologies like radio frequency, ultra sound, micro wave and alike technologies which operate on very high frequencies of orders ranging from MHz to GHz for transferring power wirelessly. It is mainly used in low power communications and sensor networks where efficiency of the power transfer is not a big concern. However this is not suitable for high power transfer and consumer electronics charging applications for efficiency and safety reasons.

Near-field systems utilizes electromagnetic field with or without resonance using inductive coupling and electrostatic/capacitive coupling power transfer technologies for wireless power transfer. Among inductive and capacitive coupling, inductive coupling can be operated at lower frequencies in the range of <100 kHz. Capacitive power transfer is operated at frequencies ranging from few hundred kHz to few MHz.

1.2.2.1 Commercialization of wireless power transfer

There are some companies that have come up with innovative solutions for powering or charging consumer electronic devices using near-field wireless power transfer technologies. They have proven that, it is possible to transfer power efficiently, safely, and over a considerable distance using inductive and capacitive power transfer by making the whole consumer product experience more convenient, reliable, and user friendly.

a) Small airgap consumer electronics

Consumer electronics like cell phones, laptops, etc., operate at low power levels and with smaller airgaps. Most popular of the recent consumer electronics that is equipped with wireless power transfer is the electrical toothbrushes by Philips Sonicare as seen in Fig. 1.4. Philips fitted the toothbrushes with rechargeable batteries that can be charged when placed in a toothbrush charging dock. Also, other companies like Witricity, Powermat Fujitsu, Solace Power, etc., are developing direct wireless power transfer solutions for stationary devices like televisions, computer monitors, speakers, kitchen appliances, etc. Also, these companies have a low power wireless charging products for mobile electronics like laptops, cellphones, etc. One of the first companies, Witricity, an MIT spinoff has recently developed software tool WiCAD™ which can be used to design and simulate small range of wireless charging system.

Very recently IKEA, a home furniture MNC introduced a wide range of home products [17] that supports wireless power transfer such as a night stand, a floor lamp, a table lamp and a work lamp with mobile charging option, mobile wireless charging pods, iPhone wireless charging option, as shown in Fig. 1.4.



(a)



(b)



(c)



(d)



(e)



(f)



(g)

Fig. 1.4 Examples of commercially available wireless charging options for consumer electronics (a) IKEA furniture with cell phone wireless charging (b) Powermat mobile phone wireless charger (c) Witricity mobile phone and laptop wireless chargers (d) Samsung mobile charging pad (e) Philips Sonicare toothbrush wireless charger (f) Apple wireless charger (g) Dell laptop wireless charging dock.

Wireless charging technology has a huge potential for very low power bio-medical applications. Wireless charging of human implantable medical devices like neuro stimulator, ventricular assist devices, defibrillators, pacemakers, etc. are being explored.

b) Large airgap high power applications

WPT also can be used to power or charge high power applications like electric vehicles, industry applications, military and aviation applications, etc., which usually require larger airgap design. However here, the efficiency of power transfer should be very high as compared to consumer electronics. Mass transit system like Shanghai Maglev Train uses principle of magnetic levitation for propulsion which is a high power wireless power transmission. In the industrial applications, where cables and contact making electric connections are not viable, wireless power transfer is well suited. In the underground mining works and exploration, where use of cables and electrical connections are not safe, a sliding transformer has been presented in [18]. In [19] Roberts and Hadfield proposed a satellite rotary connection in space application using wireless power transfer. Similarly, there is a huge market potential of wireless charging of electric vehicles.

There are two major alliances at present for near-field wireless power transfer systems viz.

- 1) Wireless Power Consortium that consists of 137 companies and
- 2) Alliance for Wireless Power (A4WP) which is newer and growing that consists of industry giants like Samsung, Powermat, NXP, Qualcomm, SanDisk, Broadcom, SK Telecom, etc.

1.2.2.2 Advantages of wireless charging or power transfer

Advantages	Disadvantages
<ul style="list-style-type: none"> 1) No cables, hence all the cable related electric hazards are mitigated. 2) Using wireless power transfer, more than one device can be charged in the secondary. 3) No worries about the charging interruption and theft as there is no plugging of cables involved. 4) Can be used even in the harsh environmental conditions. 5) Low maintenance due to no connectors or cables. 	<ul style="list-style-type: none"> 1) When inductive power transfer is used, magnetic shielding is required to avoid magnetic radiation and its hazardous effects. 2) Expensive compared to the conductive charging. 3) Distance of separation or airgap is a big concern, it is not efficient or feasible for very large airgaps. 4) Cannot be used for fast charging as the magnetic radiation in inductive power transfer and voltage between the power

6) No human intervention, therefore charging is convenient.	transfer plates in capacitive coupling are more.
7) In motion charging is possible which can reduce the energy storage on the vehicle and its cost.	5) Overall system efficiency is less compared to conductive charging as the system has a loosely coupled transformer.

1.2.1 Wireless charging of electric transportation

Due to the many advantages and development scope, EV wireless charging is considered to be a ground breaking innovation. For the first time in the EV market, during 1996, General Motors introduced the inductively coupled wireless charging system called “Magne Charge” in their EV1 and Chevrolet S-10 vehicles as seen in SAE J1773 standard. They used a ‘paddle’ that contains primary coil as a vehicle connector that can fit in the vehicle inlet that contains the secondary coil. When the paddle is plugged in, charging happens using inductive power transfer. However these pads were not really advantageous as they still involve cables and connectors. Recently Toyota demonstrated wireless charging of Prius hybrid car and announced that it will produce 2016 Prius with wireless charging facility. Qualcomm Halo has developed wireless charging for Renault ZOE vehicle platform and is licensing their WPT technology for various automotive OEMs. Other electric vehicle majors like Tesla Motors, Nissan, etc., are developing wireless charging technologies for their vehicles.

There have been many developments in wireless power transfer technology for transportation in Asia, Europe and North America. Bombardier is commercializing wireless inductive power transfer to feed continuous power to their trams across various parts of the world. At the moment, various wireless charging systems are demonstrated for power levels up to 10 kW with an overall system efficiencies between 85 – 95%. During mid-2015, UK came out with their plans for the dynamic or in-motion charging of electric cars with a separate electric car wireless charging lanes. South Korea has a proven 12 km road that charges electric buses as they drive [20].

When it comes to academia, University of Auckland in New Zealand has been upfront in the development of wireless charging of electric vehicles using inductive power transfer. Their technology has been patented and licensed through the University’s UniServices. KAIST

University in South Korea has also demonstrated their inductive WPT technology during early 2012.

Efforts for standardization of wireless charging in electric vehicles have been started internationally. The Society of Automotive Engineers (SAE) task force is defining and developing wireless charging standard SAE J2954 for electric vehicles. Clearly, with the many ongoing projects across academia and industry worldwide indicates that there is a rapidly increasing interest of wireless charging of electric vehicles. It is expected to have a \$17 Billion scope for wireless charging market by 2019 [21].

1.2.1.1 Wireless charging system of an electric vehicle

Wireless charging of electric vehicles is possible using electromagnetic power transfer and electric static power transfer [22],[23]. In the electromagnetic power transfer the power is transferred from the primary to secondary through a large airgap using high frequency magnetic field. On the other hand, in electrostatic field, the power is transferred using electro static field.

Wireless charging using inductive power transfer can be classified as a non-resonant IPT system and resonant IPT system. The basic difference between these two systems is the resonance phenomenon in the operation. Non-resonant IPT systems are best suited to very small airgap applications [24], [25] and found to be very efficient as seen in the GM EV1 Magne Charge. On the other hand, in RIPT systems, the primary transmitter and the secondary receiver coils resonate at the same frequency. The interaction of magnetic fields in both these cases is very different. RIPTs are best suited to operate at very high frequency for larger airgap applications [26]–[28].

It is extremely difficult to analyze or study the magnetic field of an WRIPT system as discussed in chapter-4. However, IPT system magnetic field can be studied using FEA tools. An efficient MPTS design for IPT application can also perform better in an WRIPT system for large airgap wireless charging applications as the coupling is much better during resonance [29].

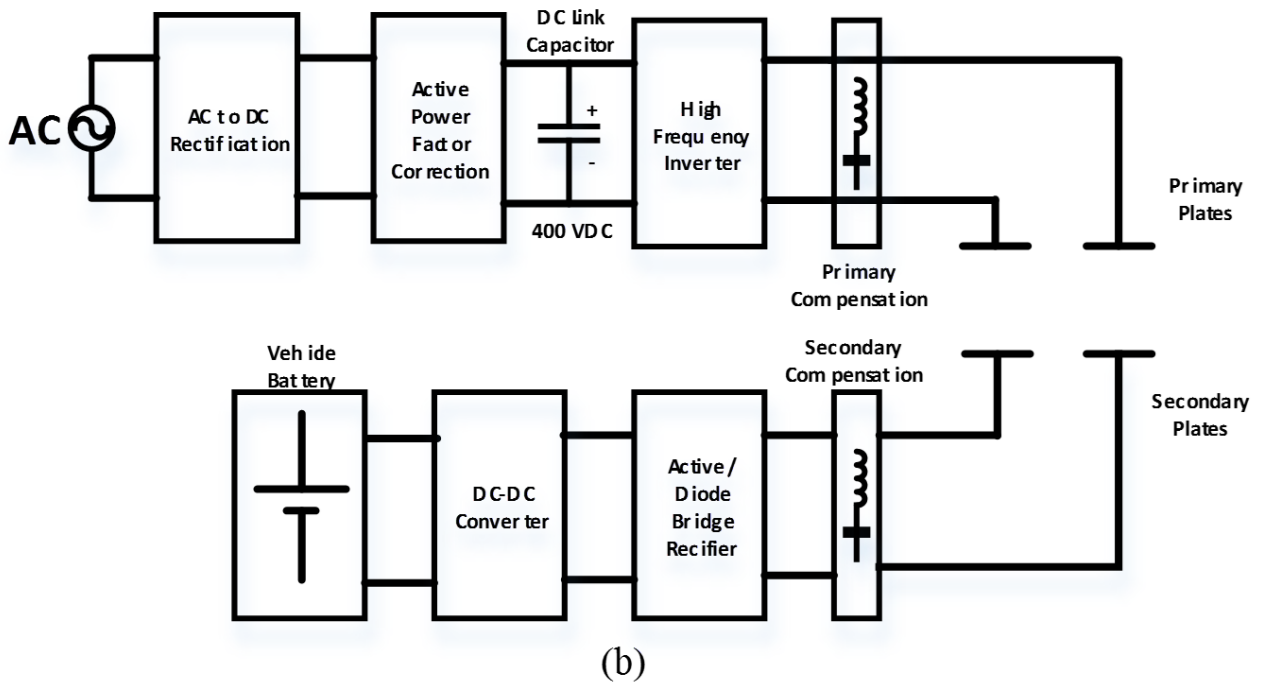
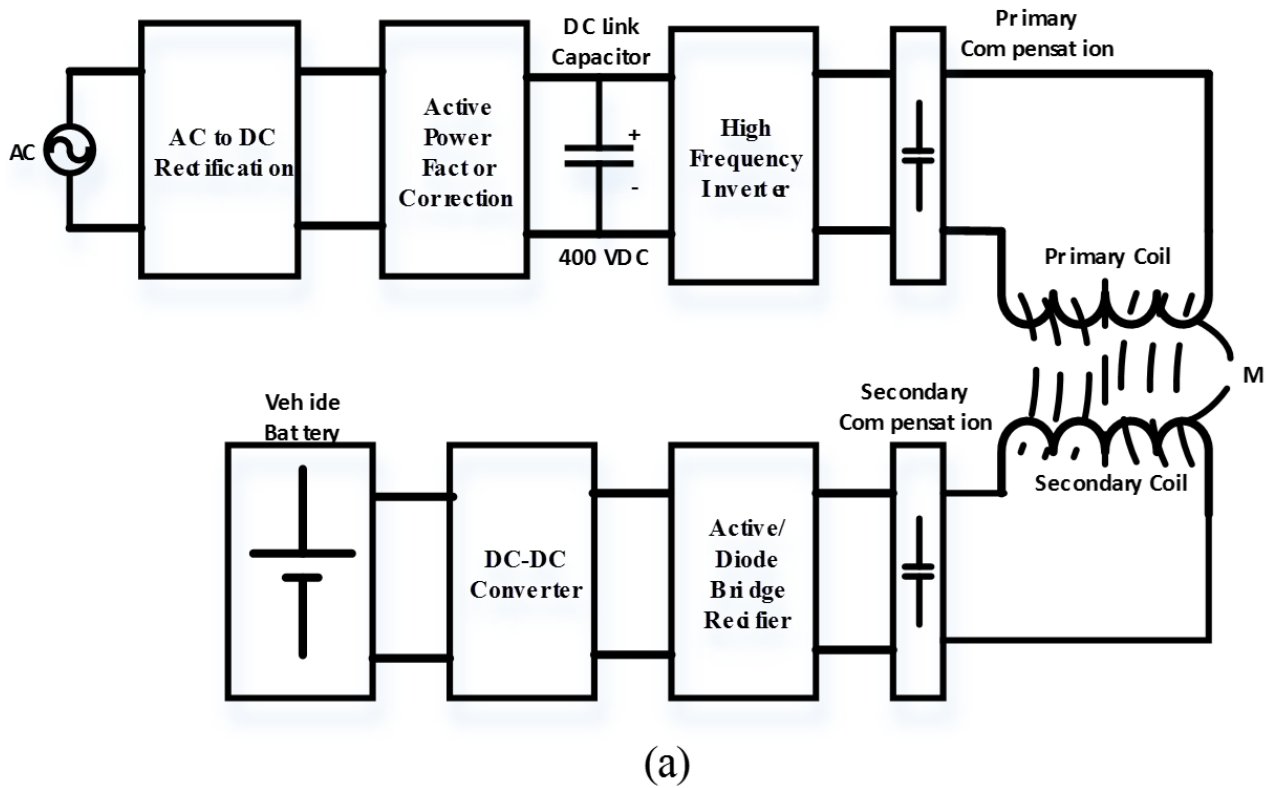
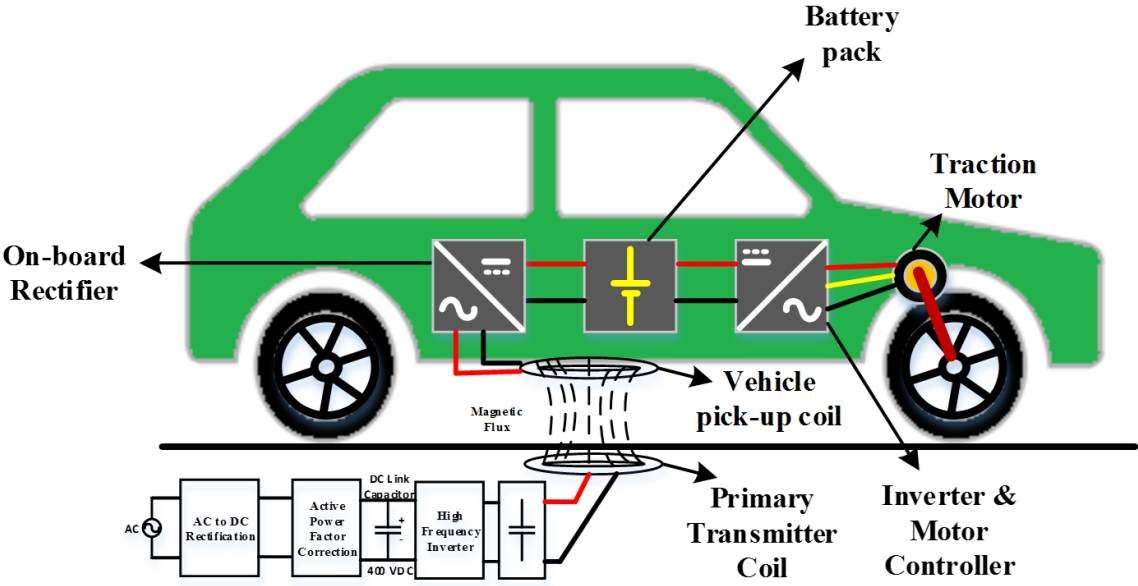
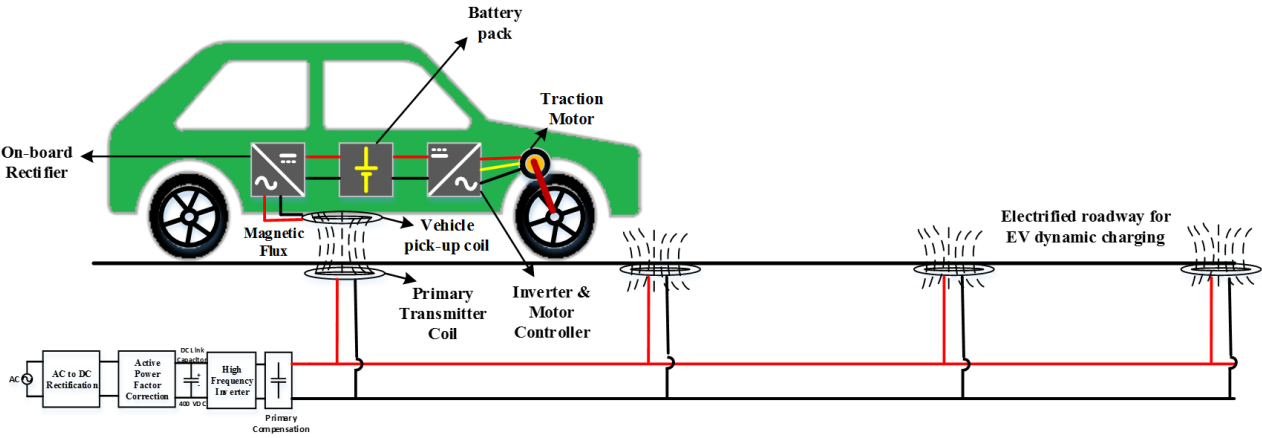


Fig. 1.5 (a) WRIPT based wireless charging system (b) CPT based wireless charging system

Fig. 1.5 shows the basic block diagram for the WRIPT and CPT based wireless charging system. It is seen from [11], [30], [31] that using inductive power transfer, higher powers can be transferred through larger airgaps.



(a)



(b)

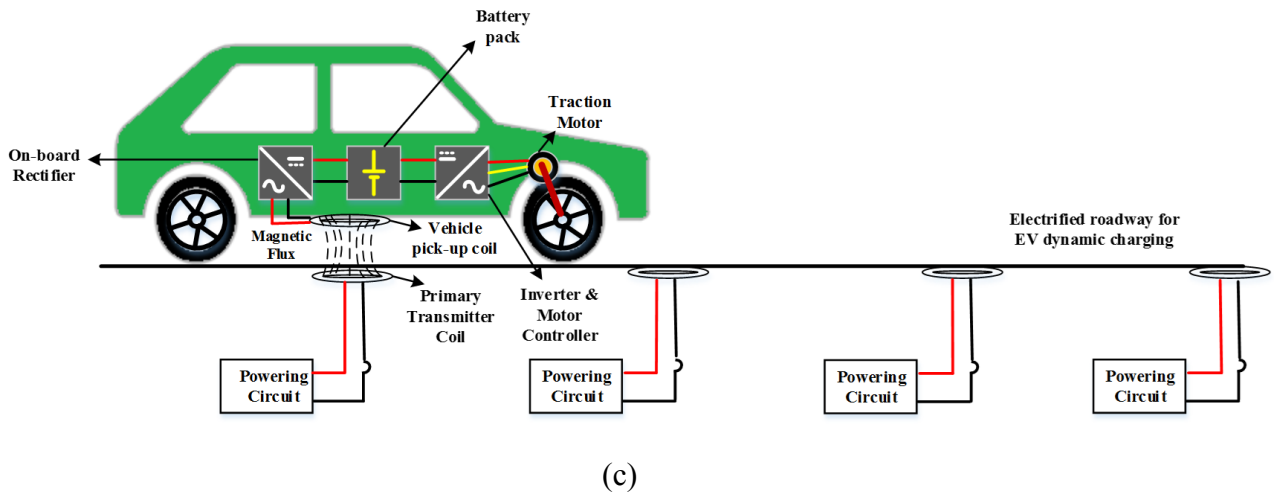


Fig. 1.6 EV wireless charging using inductive power transfer (a) stationary charging (b) Dynamic or in-motion charging powered by a single high power driver circuit (c) Dynamic charging powered by separate low power driver modules

As seen in the Fig. 1.6 (a), in the stationary wireless charging, vehicle is parked over a primary or transmitter coil that is located in the parking lot or a garage at home. It is powered by a 1- \emptyset or 3- \emptyset driver circuit depending on the power required [32]–[34]. There is a secondary or pickup coil on the vehicle that magnetically couples and receives the AC power from primary through this magnetic field. On-board rectifier electronics converts the AC Power into battery required DC power. In the case of stationary wireless charging, both primary and secondary coils are stationary. There needs a proximity communication between transmitter unit and vehicle to make sure that the vehicle pick-up coil and the primary transmitter coil are aligned accordingly for high efficiency power transfer. Also other mechanical designs can be made to take care of the alignment issues.

Fig. 1.6 (b) and (c) shows the system representation of the dynamic charging or in-motion charging which is made possible only due to wireless power transfer. From [27], [28], [35]–[37], it can be learnt that the in-motion wireless charging can be very advantageous. As there is a continuous power available for vehicle propulsion, there needs very less energy storage on-board the vehicle, therefore the required battery capacity reduces drastically which can result in the reduced price tag for buying an EV. There are two ways to design the inductive in-motion charging system; as seen in Fig. 1.6 (b), we can use only one unit of high power driver unit. However this is not an advisable design for many reasons; it is not reliable in case of any technical

issue, whole system stops working, secondly it is expensive as well. Also as the driver circuit is only one, all the primary coils receive power and will be floating which will cause wastage of power. Alternatively we can design the system with modular driver units as shown in Fig. 1.6 (c). We can turn on each driver module as the vehicle is running over it. This avoids wastage of power and being modular, the system is more reliable and is very less expensive.

1.3 Research Objectives and Contributions

The main goal of this research work is to design and develop a novel 1.0 kW resonant inductive wireless power transfer system for electric golf –kart charging.

Present day electric golf-karts are charged using regular conductive charging techniques. For the safety and convenience reasons of golfers, golf-kart wireless charging is a very good application.

- Firstly, the theory for wireless charging has been studied. At the heart of the WPT system, there exists a high frequency magnetic power transfer circuit. Initially literature study has been made on all the available inductive WPT magnetic circuits (coil designs).
- Power transfer capacity and power transfer efficiency of a wireless RIPT system at various airgaps and misalignment conditions are studied for different ferromagnetic cores combinations. This study is done using JAMG finite element analysis and experiments verification.
- From the results obtained, potential design combinations are selected and different winding configurations are studied with JMAG and verified experimentally for small power transfer.
- From the experiments a final best core and coil combination is selected and 1.0 kW system is designed.
- The designed system is modelled, simulated and experimentally verified for a 1.0 kW load power transfer. From the experimental results, it is seen that the designed system can operate with a 94.7% DC to DC power transfer efficiency at a 10 cm airgap.
- A control scheme presented along with convincing simulation results to charge an industrial electric vehicle which usually is equipped with a 48 V battery pack on-board the vehicle.

1.4 Organization of Thesis

Working principles of inductive power transfer for wireless applications are explained in chapter-2. It is followed by chapter-3 explaining the design investigations of a novel magnetic power transfer system for wireless RIPT applications. In chapter-4, the final design of a 1.0 kW system with 10 cm airgap is presented along with simulation and experimental results. Chapter-5 explains the control of the class-D amplifier for wireless RIPT application to achieve unity voltage gain. In chapter-6 industrial EV charging using wireless RIPT system is presented with simulation results and comparison. Finally conclusion chapter is presented that also gives the scope of future work for this thesis.

Chapter-2 Working principle of inductive power transfer system

The core component of the inductive WPT system is the magnetic power transfer circuit. This magnetic power circuit is an inductively coupled circuit that can transfer power over a large airgap from the primary to the movable or stationary secondary. The power transfer happens via high frequency magnetic field from primary winding to the secondary winding which forms a loosely coupled transformer. For understanding the working of a loosely coupled transformer, we need to understand the theory of electromagnetics.

2.1 Theory of Electromagnetics

We know that the Ampere's law is given by

$$\nabla \times B = \mu_0 \cdot J \quad (2.1)$$

Here, B is the magnetic field density with units Tesla or Wb/m^2

$\nabla \times$ is called as the curl which gives the measure of the strength of B

μ_0 is permeability of the medium

J is the current density

It states that the curl of the magnetic field (B) which gives the measure of magnetic field's strength is proportional to the electric current through the loop.

Ampere's law is modified by Maxwell, which states in addition to the Ampere's law, that the magnetic field strength is also proportional to the rate of change of the electric field. It is given as

$$\nabla \times B = \mu_0 \cdot J + \epsilon_0 \cdot \mu_0 \cdot \frac{dE}{dt} \quad (2.2)$$

Here, B is the magnetic field density with units Tesla or $Wb/unit\ area$

$\nabla \times$ is called as the curl which gives the measure of the strength of B

μ_0 is magnetic permeability of free space

ϵ_0 is electric permittivity of free space

J is the current density with units A/unit area

E is the electric field

From equation (2.2) it is clear that generation of magnetic field does not happen with just electric current but it requires a time varying electric field. That is an oscillating electric field produces a variable magnetic field.

Equation (2.2) can also be expressed as $\oint B \cdot dl = \mu_o \left(I + \epsilon_o \cdot \frac{dE}{dt} \right)$

This equation can be written as $\phi = \oint B \cdot dS$, where S is the surface through which magnetic flux ϕ flows.

The magnetic flux generated is proportional to the applied current $\phi \propto I$,

The proportionality can be reduced as $\phi = L \cdot I$, where L is the inductance of the current carrying conductor.

For a coil formed with N turns, the inductance is given by

$$L = \frac{N \cdot \phi}{I}, \text{ here } \phi \propto B \text{ and } B \propto N \text{ therefore } L \propto N^2$$

The magnetic flux density, flux and inductance of the current carrying conductor wound on a magnetic core is expressed as

$$B = \frac{\mu_o \cdot \mu_r \cdot N \cdot I}{l} \quad (2.3)$$

We know that $B = \phi \cdot A$ and self-inductance L can be given by $L = \frac{N \cdot \phi}{I}$

$$\text{Therefore, } L = \frac{\mu_o \cdot \mu_r \cdot N^2 \cdot A}{l} \quad (2.4)$$

Consider two coils as shown in Fig. 2.1. Here coil-1 and coil-2 with N_1 and N_2 as number of turns are supplied with currents I_1 and I_2 . Both the currents produces the magnetic field as shown. The direction of magnetic flux is given by the Fleming's right hand thumb rule. Each coil has a self-

inductance and leakage inductance. There is also a mutual inductance between these coils which is the inductance due to current in the other coils or inductors.

Here the self-inductance is given by

$$\phi_{11} = \oint B_1 \cdot dS_1, \text{ where } S_1 \text{ is the surface of the coil-1 magnetic field, similarly}$$

The self-inductance of the coil-1 is given by $\frac{N_1 \cdot \phi_{11}}{I_1} = L_{11}$, similarly for coil-2

$$\phi_{22} = \oint B_2 \cdot dS_2 \text{ and self-inductance is given by } \frac{N_2 \cdot \phi_{22}}{I_2} = L_{22}$$

Mutual inductance is given by

$$\phi_{12} = \oint B_1 \cdot dS_2 = L_{12} \cdot I_1$$

$$\phi_{21} = \oint B_2 \cdot dS_1 = L_{21} \cdot I_2$$

Realizing the equations (2.3) and (2.4), we get that the mutual inductances are equal and expressed as

$$M=L_{12}=L_{21} \tag{2.5}$$

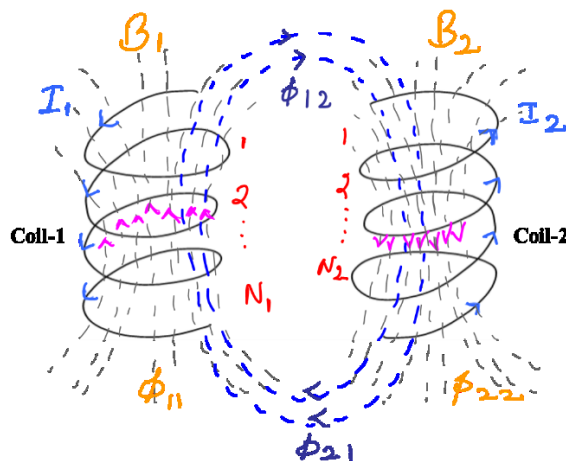


Fig. 2.1 Coupled magnetic coils

The relation between the self-inductances and the mutual inductance is given by the concept of coefficient of coupling. The coupling coefficient denoted by ‘k’ is expressed as

$$k = \frac{M}{\sqrt{L_{11} \cdot L_{22}}} \quad (2.6)$$

The coefficient of coupling is used to understand how well any the inductors are coupled. The value of k ranges between 0 and 1. Co-efficient of coupling is said to be 100% if the two coils are very tightly coupled and the leakage inductance is zero.

2.2 Loosely coupled Inductive systems

An electrical transformer as shown in Fig. 2.2 has primary and secondary coils wound on a magnetic core. The magnetic core acts as a low reluctance medium for the magnetic flux to link between the primary and secondary coils. Here the leakage flux thus leakage inductance is very minimal due the existence of core and hence it is a very tightly coupled magnetic system. As the leakage inductance is very less and mutual inductance is very large, the current required to generate the magnetic flux is very minimal in a regular transformer.

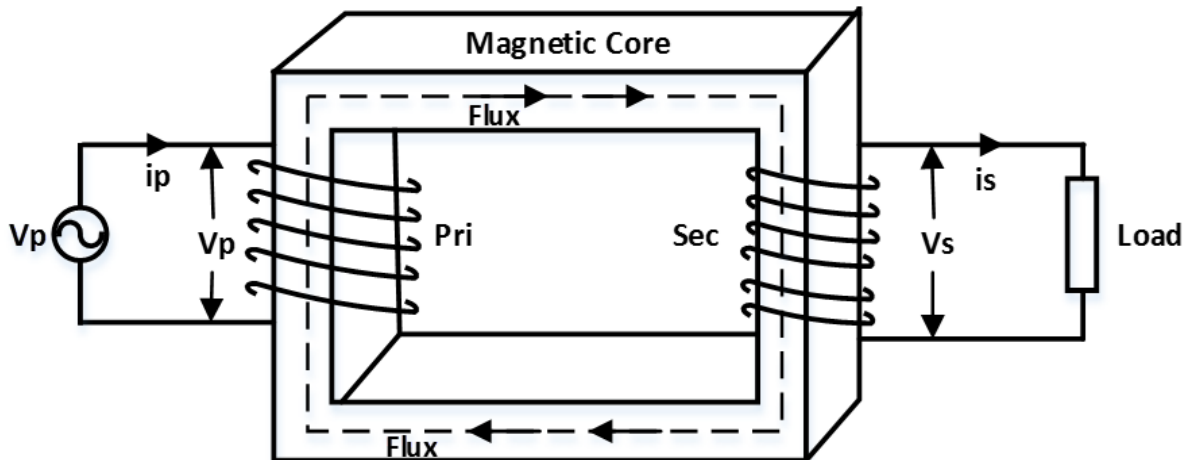


Fig. 2.2 Electrical Transformer

Contrarily, wireless inductive power transfer system is composed of a primary transmitter coil and a secondary receiver coil separated by a large airgap ‘a’ as shown in Fig. 2.3. As the two coils are separated by a relatively large airgap, the leakage inductance is very high and mutual inductance is

very low. Therefore, the inductive wireless power transfer system is called a loosely coupled system and the coupling coefficient is very less.

Due to the current i_p flowing in the primary a voltage V_s is induced in the secondary coil. When secondary coil is connected to a load, current i_s causes a magnetic flux in the secondary that opposes the mutual flux.

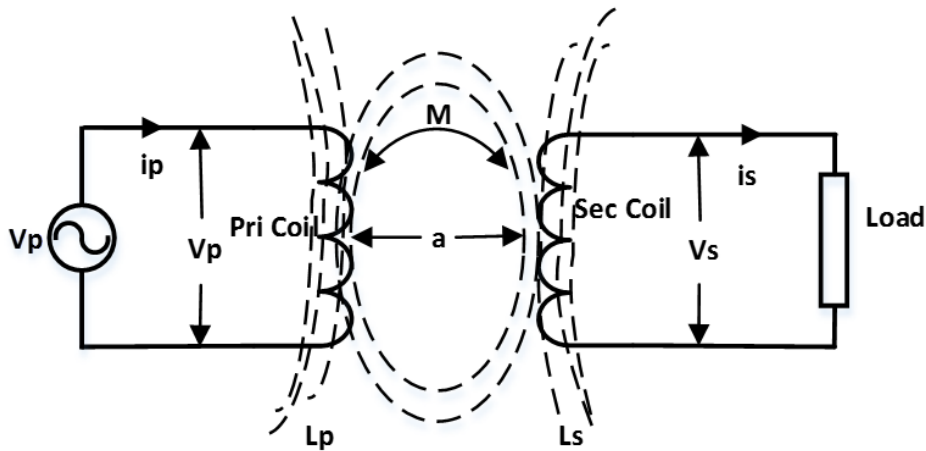


Fig. 2.3 Wireless Inductive system separated by an airgap “a”

The electrical circuit representation of the WIPT system delivering power to load R_L can be shown as seen in Fig. 2.4. Here L_p is the self-inductance of the primary coil, L_s is the self-inductance of the secondary coil and M is the mutual inductance between the primary and secondary coils. The primary transmitter is supplied with a voltage source operating at frequency of ‘ ω ’.

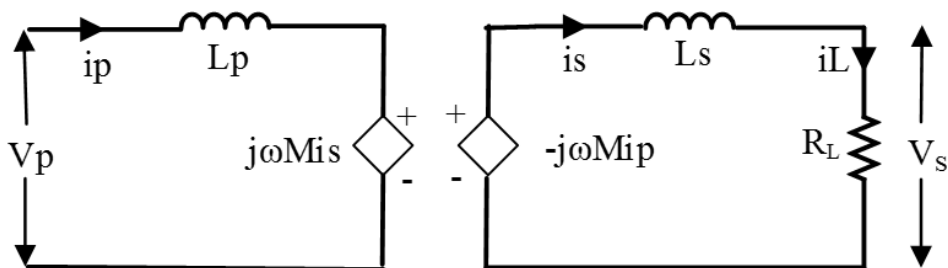


Fig. 2.4 Electrical representation of the WIPT system

The primary and secondary voltages are given by

$$V_p(t) = L_p \cdot \frac{di_p(t)}{dt} - M \cdot \frac{di_s(t)}{dt} \quad (2.7)$$

$$V_S(t) = M \cdot \frac{di_P(t)}{dt} - L_S \cdot \frac{di_S(t)}{dt} \quad (2.8)$$

Considering all the currents are sinusoidal waveforms and steady state equations are written as

$$V_P = j\omega L_P I_P - j\omega M I_S \quad (2.9)$$

$$V_S = j\omega M I_P - j\omega L_S I_S \quad (2.10)$$

Considering the non-ideal coil design with the coil resistance, the above voltage equations becomes

$$V_P = R_P I_P + j\omega L_P I_P - j\omega M I_S \quad (2.11)$$

$$V_S = j\omega M I_P - R_S I_S - j\omega L_S I_S \quad (2.12)$$

From the above equations, the electrical equivalent circuit of the WIPT system can be modelled as shown in the Fig. 2.5.

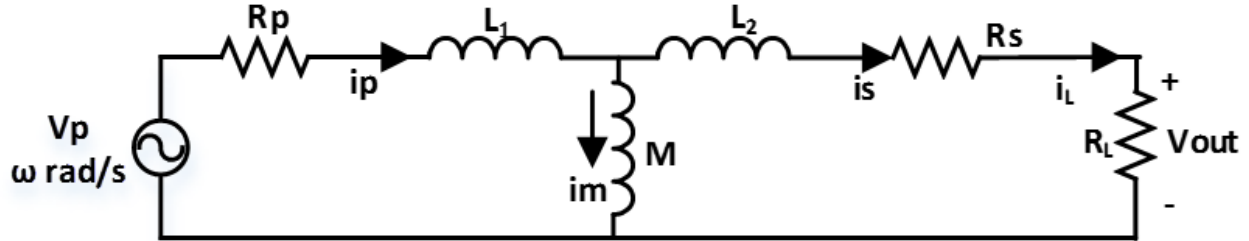


Fig. 2.5 Equivalent circuit model of the WIPT system

The self-inductance is the combination of the mutual inductance and the leakage inductance. Mutual inductance is the useful flux that links the primary and secondary coils and leakage inductance links to the same coil itself which is merely useless. Due to the existence of the large airgap, in the WIPT system there will be very large leakage inductance due to which the coupling coefficient is very low [38], [39]. The self-inductances are given by

$L_p = L_1 + M$ and $L_s = L_2 + M$, where L_1 and L_2 are the leakage inductances of the primary and secondary coils respectively.

2.3 Need for High Frequency in WIPT operation

In the WIPT system, the power transfer from the primary and secondary is mainly due to the mutual inductance that links the primary and the secondary coils.

As seen from the Fig. 2.4, the voltage induced in the secondary coil is given by

$$V_S = -j\omega M I_P$$

Here, for a given design, to generate the steady magnitude of the secondary voltage, we need to have a large mutual inductance or large magnitude of the primary current or we need to feed the input with a very high frequency.

As we have seen in the previous sections, in a WIPT system, due to large airgap the mutual inductance is very low, hence for a given magnetic circuit design, mutual inductance of the system is fixed and we cannot increase it. Primary current I_P cannot be increased after a certain extent as it mainly depends on the load and type of the compensation of the system as explained in subsequent sections. One other adverse effect of increasing the primary current is the increase in device switching losses and Ohmic losses which will make the system very inefficient.

The only variable to play around to transfer power efficiently is the operating frequency. With the higher operating frequencies, one can transfer higher power to a larger airgaps.

As seen from the above analysis and equations, in the WIPT system, where the primary and secondary are loosely coupled, the primary should be fed by a high frequency source.

2.2.1 Effects of high frequency operation and use of Litz wires

Due to the use of high frequency, in WIPT system we have to deal with related conductor losses due to high frequency. Material conductivity σ is the ability to carry electric current measured in Siemens/meter. It is very high in metals like copper, aluminum, silver, etc., and very poor in insulators like rubber, glass, paper, etc. Resistance is the opposite of the conductivity measured in Ohms.

The DC resistance in a material is expressed in terms of the material resistivity ρ , area of cross section A , and length of the conductor l as $R_{DC} = \frac{\rho \cdot l}{A}$

From the theory of electromagnetism, we know that a current carrying conductor induces a magnetic field. When the current is DC, the magnetic field is almost constant in the conductor. But when a high frequency current is passed through a conductor, conductor experiences its own magnetic field and field in the neighboring conductors, which induces eddy currents. These eddy currents oppose current in the conductor. These are classified as two effects viz. skin effect and proximity effect.

In DC currents the current density is considered uniform across the cross section area A of the conductor. However, in the high frequency operation, the current density is not uniform in a conductor, it is more concentrated at the surface of the conductor and least at the center of the conductor. This effectively increases the conductor resistance for AC current. This effect is called “Skin Effect.” The skin depth δ is the depth at which the current density falls to $1/e$ times the

current density of the surface. It is expressed as $\delta = \sqrt{\frac{2\rho}{\omega\mu}}$, ρ is the material resistivity, ω is the operating frequency and μ is the material permeability.

Here the skin effect is very negligible if the skin depth is much larger than the conductor thickness due to lower resistance. However for high frequency WIPT operation, we cannot use larger conductor sizes.

One more effect that increases the conductor resistance for the high frequency currents is proximity effect. In this effect, the time varying magnetic fields in one conductor induces the voltage in the surrounding conductors and which produces the eddy currents which opposes the main current.

To avoid the power losses due to high frequency operation, we use Litz wire that is constructed with multiple thin insulated strands which reduces the proximity and skin effects at higher frequency operations [40].

2.3. Need for Compensation

Due to larger airgaps, WIPT system has a very poor coupling between primary and secondary coils. WIPT system is a loosely coupled system, it inherently is an inductive system due to large leakage and magnetizing inductance. As the WIPT system is operated using a high frequency

power supply, the source sees larger inductive reactance. Due to this, the source operates at a very poor power factor [41]. Due to very low power factor, for a given load, the system should be designed with a very higher VA rating, which requires higher rated source side power electronics converter. Also due to larger inductive reactance and circulating currents, there will be more Ohmic losses that reduces the system efficiency.

Therefore, the primary coil is compensated with the capacitor that produces equal and opposite capacitive reactance to nullify the system inductive reactance.

Let us consider the un-compensated WIPT circuit as shown in the Fig. 2.4. Using maximum power transfer theorem, here the maximum power transferred to the load is given as

$$P_{\max} = \frac{V_{oc} \cdot I_{sc}}{2} \quad (2.13)$$

Where, V_{oc} is the secondary open circuit voltage, given by $V_{oc} = \omega M I_P$ and I_{sc} is the secondary

short circuit current, given by $I_{sc} = \frac{\omega M I_P}{\omega L_s}$

Substituting V_{oc} and I_{sc} , (2.13) becomes,

$$P_{\max} = \frac{\omega^2 M^2 \cdot I_P^2}{2\omega L_s} \quad (2.14)$$

As shown in [41], to transfer maximum power to the load, the secondary has to be compensated and the power transfer in the compensated system is maximum if the secondary is operated at the same frequency as the primary.

As seen in [42]–[44] the primary coil is compensated just for its self-inductance, however the source also sees the secondary inductance reflected to the primary. Therefore, the primary coils should be compensated for the total system inductance. To conclude, for an efficient power transfer from primary to secondary, both the primary coil and secondary coils should be compensated with capacitors and should operate at the same frequency.

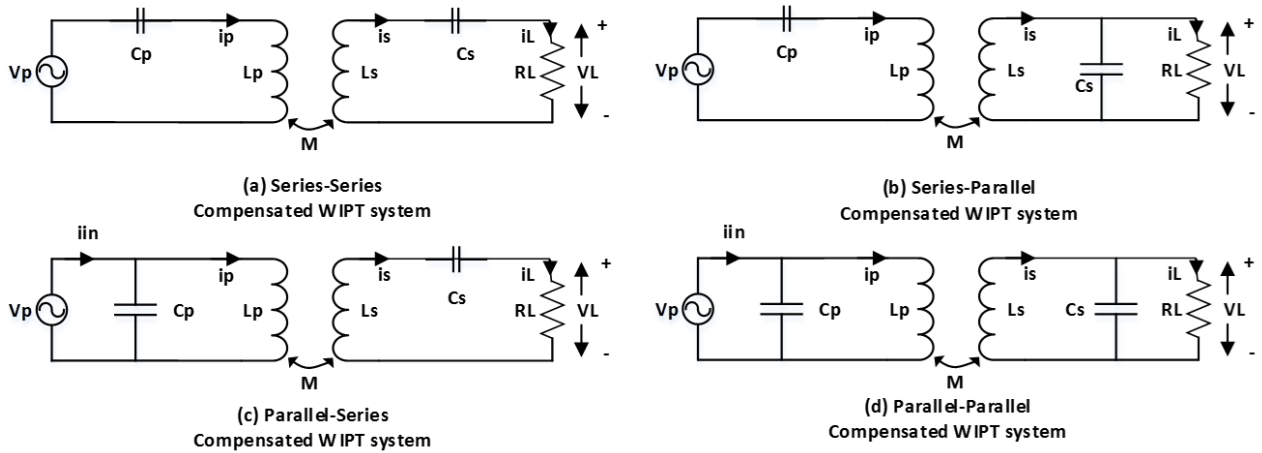


Fig. 2.6 4 basic compensation topologies of a WRIPT system

In general there are 4 basic compensation techniques as shown in the Fig. 2.6. These are commonly used as SS, SP, PS, PP topologies, where first and second letters represents the primary side and secondary side capacitor connection type respectively. Among these basic techniques, the SS topology is very popular, next to that is SP topology. As seen in [40]–[44], various works present the merits and de-merits of the both these topologies. On the other hand, the parallel compensated primary topologies are found to be very poor for WRIPT applications due to very bad efficiencies at higher quality factors and complexity in control.

Recently, as seen in [11], [49]–[51], LCC compensation topology using multiple resonant components is developed which reduces the reactive losses in the primary side and claims to achieve better efficiencies at very large airgaps.

In this thesis work, only SS and SP compensations are considered. In particular, this work concentrates on using SP compensation. The main reason for choosing the SP topology is to avoid any voltage stress or voltage swings on the secondary capacitor.

2.3.1 SS Compensated WRIPT System

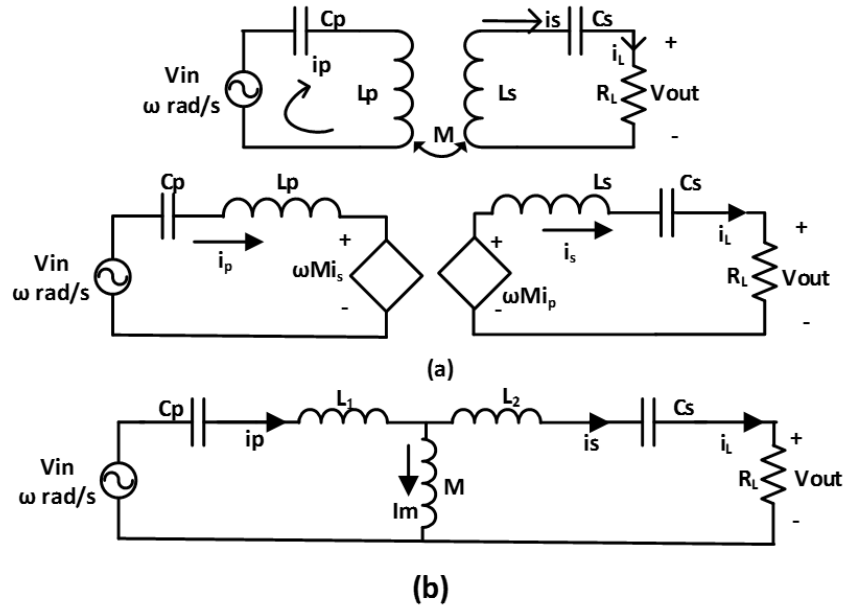


Fig. 2.7 SS WIPT system (a) System circuit (b) Equivalent circuit model

The electrical circuit representation of the SS WRIPT system is as shown in Fig. 2.7 (a). As discussed in section 2.2, we can represent the equivalent circuit model for SS system as seen in Fig. 2.7 (b). Here, $L_p = L_1 + M$ and $L_s = L_2 + M$

$$\text{Resonant tank frequency, } \omega = \frac{1}{\sqrt{L_p \cdot C_p}} = \frac{1}{\sqrt{L_s \cdot C_s}} \text{ rad/s}$$

From the equivalent circuit shown above, we get

$$Z_{\text{sec}} = j\omega L_s + \frac{1}{j\omega C_s} + R_L \quad (2.15)$$

$$Z_{\text{pri}} = \frac{1}{j\omega C_p} + j\omega L_p \quad (2.16)$$

The equivalent impedance seen by the primary source is given by

$$Z_{\text{ss}} = \frac{\omega^2 M^2}{Z_{\text{sec}} + R_L} \quad (2.17)$$

The imaginary part of the equivalent impedance seen by the input source is given as

$$\text{Im}(Z_{ss}) = \left(\left((\omega \cdot L_p) - \frac{1}{\omega \cdot C_p} \right) - \frac{\omega^2 M^2 \left((\omega \cdot L_s) - \frac{1}{\omega \cdot C_s} \right)}{R_L^2 + \left((\omega \cdot L_s) - \frac{1}{\omega \cdot C_s} \right)^2} \right) \quad (2.18)$$

To obtain the unity power factor, the imaginary part of the input impedance should be equal to zero, by solving (2.18) and equating it to zero, we can obtain the capacitor value required to compensate the primary inductance.

$$C_p = \frac{1}{\omega_o^2 \cdot L_p} \quad (2.19)$$

As seen from (2.19), the primary capacitor value is independent of any other system parameter expect for the resonant frequency and the primary self-inductance.

Primary and secondary currents are given by

$$i_p = \frac{V_{in}}{Z_{pri} + Z_{ss}} \text{ and } i_L = \frac{j\omega M i_p}{Z_{sec} + R_L} \quad (2.20)$$

Now, the voltage gain is calculated as

$$G_v = \frac{V_o}{V_{in}} = \frac{i_L \cdot R_L}{(Z_{pri} + Z_{ss}) \cdot i_p} = \frac{j\omega M}{\frac{Z_{pri} \cdot Z_{sec} + \omega^2 M^2}{R_L} + Z_{pri}} \quad (2.21)$$

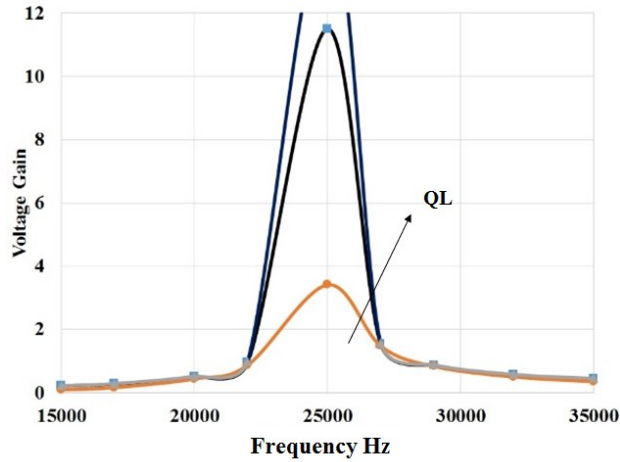


Fig. 2.8 Voltage gain characteristics of the SS WIPT system

Further simplification of (2.21) by solving with the load independent value of ω , we get

$$\text{Voltage gain at resonant frequency} = G_v = \frac{V_o}{V_{in}} = \sqrt{\frac{L_{sec}}{L_{pri}}} \quad (2.22)$$

The voltage gain curve can for normalized frequency ratio is as shown in Fig. 2.8.

$$\text{Here the secondary load quality factor can be expressed as } Q_{ss} = \frac{\omega_o \cdot L_s}{R_L} \quad (2.23)$$

2.3.1 SP Compensated WIPT System

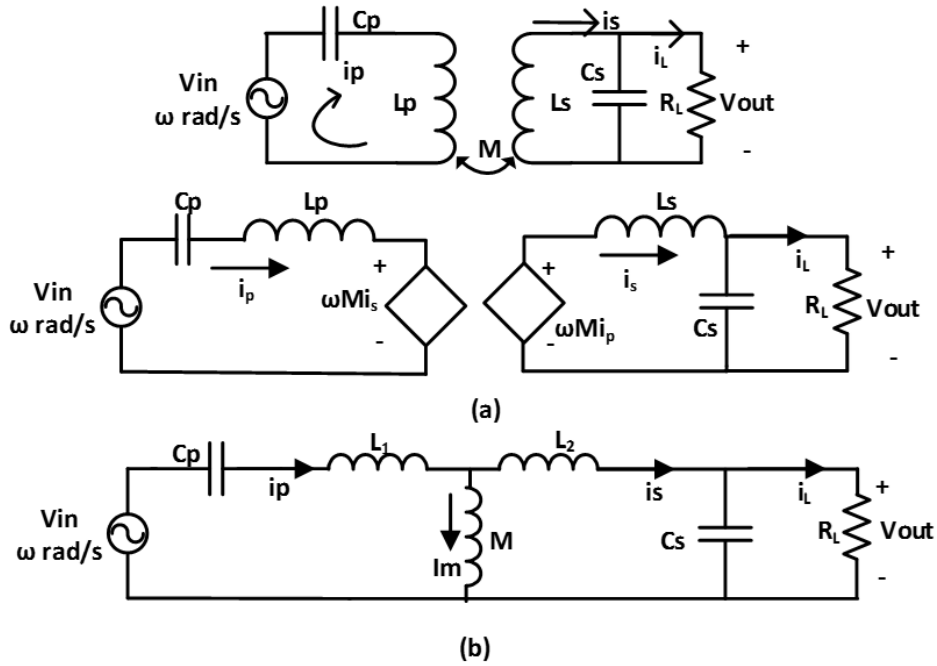


Fig. 2.9 SP WIPT system (a) System circuit (b) Equivalent circuit model

The electrical circuit representation of the SP WIPT system is as shown in Fig. 2.9 (a). As discussed in section 2.2, we can represent the equivalent circuit model for SP system as seen in Fig. 2.7 (b). Here, $L_p = L_1 + M$ and $L_s = L_2 + M$

From the equivalent circuit shown above, we get

$$Z_{sec} = j\omega L_s + \left[\frac{1}{j\omega C_s} // R_L \right] \quad (2.24)$$

$$Z_{pri} = \frac{1}{j\omega C_p} + j\omega L_p \quad (2.25)$$

The equivalent impedance seen by the primary source is given by

$$Z_{sp} = \frac{M^2\omega^2}{j\omega L_s + \frac{R_L}{1 + jR_L C_s \omega}} + j\omega L_p - \frac{j}{\omega C_p} \quad (2.26)$$

The imaginary part of the (2.26) can be obtained as

$$\text{Im}(Z_{sp}) = \left(\left(\omega \cdot L_p \right) - \frac{1}{\omega \cdot C_p} \right) - \frac{\omega^2 M^2 \left(C_s R_L^2 \left(\omega^2 L_s C_s - 1 \right) + L_s \right)}{\left(R_L - \omega^2 \cdot L_s C_s R_L \right)^2 + \omega^2 \left(L_s + C_s R_L \right)^2} \quad (2.27)$$

To obtain the unity power factor, the imaginary part of the input impedance should be equal to zero, by solving (2.27) and equating it to zero, we can obtain the capacitor value required to compensate the primary inductance.

$$C_p = \frac{L_s^2 \cdot C_s}{L_s L_p - M^2} \quad (2.28)$$

From (2.28), it is evident that the primary capacitor is very sensitive to the changes in the mutual inductance of the system.

Primary and secondary currents are given by

$$i_p = \frac{j\omega L_s \cdot i_s + V_{out}}{j\omega M} \quad \text{and} \quad i_s = i_L + i_{C_s} = \frac{V_{out}}{R_L} + j\omega C_s \cdot V_{out} \quad (2.29)$$

Input and output voltages are given by

$$V_{in} = \left(j\omega L_p + \frac{1}{j\omega C_p} \right) \cdot i_p - j\omega M i_s \quad (2.30)$$

$$V_{out} = R_L \cdot i_L \quad (2.31)$$

Taking the ratio of V_{out} to V_{in} , we get

$$\frac{V_{out}}{V_{in}} = \frac{i_L \cdot R_L}{\left(j\omega L_p + \frac{1}{j\omega C_p} \right) \cdot i_p - j\omega M i_s} \quad (2.32)$$

Solving equation (2.32) and by substituting above obtained equations, we get

$$\frac{V_{out}}{V_{in}} = \frac{j\omega M}{\left(j\omega L_p + \frac{1}{j\omega C_p} \right) \cdot Z_{sec} + \omega^2 M^2} \cdot \frac{R_L}{1 + j\omega C_s \cdot R_L} \quad (2.33)$$

Solving above equations, we obtain

$$\text{Voltage gain at resonant frequency} = \left| \frac{V_{out}}{V_{in}} \right| = \frac{1}{k} \cdot \sqrt{\frac{L_s}{L_p}} \quad (2.34)$$

$$\text{Also, resonant tank frequency, } \omega = \frac{1}{\sqrt{1-k^2}} \cdot \frac{1}{\sqrt{L_p \cdot C_p}} = \frac{1}{\sqrt{L_s \cdot C_s}} \text{ rad/s}$$

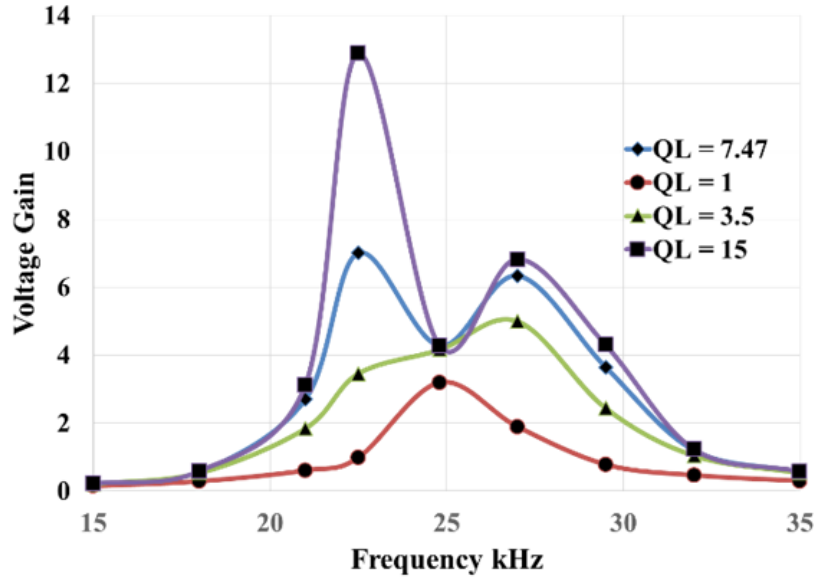


Fig. 2.10 Voltage gain characteristics of the SP WIPT system

The voltage gain characteristics as per (2.31) can be plotted as shown in Fig. 2.10.

$$\text{Here the secondary load quality factor is given as } Q_{sp} = \frac{R_L}{\omega_o \cdot L_s}$$

2.1 Power Electronics Requirement

As learnt in the previous sections, the WRIPT system utilizes a high frequency power source to drive the primary transmitter circuit. The regular domestic power supply operates at either 50/60 Hz frequency. We make use of high frequency inverter circuit for generating the WRIPT required kHz range frequency from the available 50/60 Hz power supply. The basic power electronic system for driving the WRIPT system is as shown in Fig. 1.4 (a). The usual range of operating frequency for a WRIPT charging application is between 10 kHz and 200 kHz. But as per the latest SAE J2954 standard, it is restricted to not more than 85 kHz. As the conduction losses and the switching loss are very high at the higher frequency operation, for better system efficiency, we should operate the inverter in soft-switching conditions. Soft switching conditions are when the power electronic device in the converter is turned on when the voltage across the device is zero (Zero Voltage Switching) or turned off when the current through the device is (Zero Current Switching).

In a high frequency inverter circuit, the output voltage is a square wave. However due to resonance in the WRIPT system design with resonating capacitor, the currents are sinusoidal. With the help of sinusoidal current in the resonant inductive coupling system, inherently we can achieve the soft-switching.

There are numerous switch mode power inverters which can be used to in WRIPT applications. As seen in the Fig. 1.4 (a), from the 50/60 Hz AC wall power, we rectify and use an active power factor correction (APFC) stage to reduce system losses and produce a stiff DC voltage as the input to the high frequency inverter. This inverter further converts the DC into a required high frequency AC supply. This is a very commonly used two stage conversion. However, researchers are exploring single stage AC-AC conversion, where power can be converter from 50/60 Hz wall AC power to required high frequency AC power with PFC and control in the same stage.

The very commonly used inverter circuits are full bridge, half bridge converters [21]-[45] as seen in the Fig. 2.11.

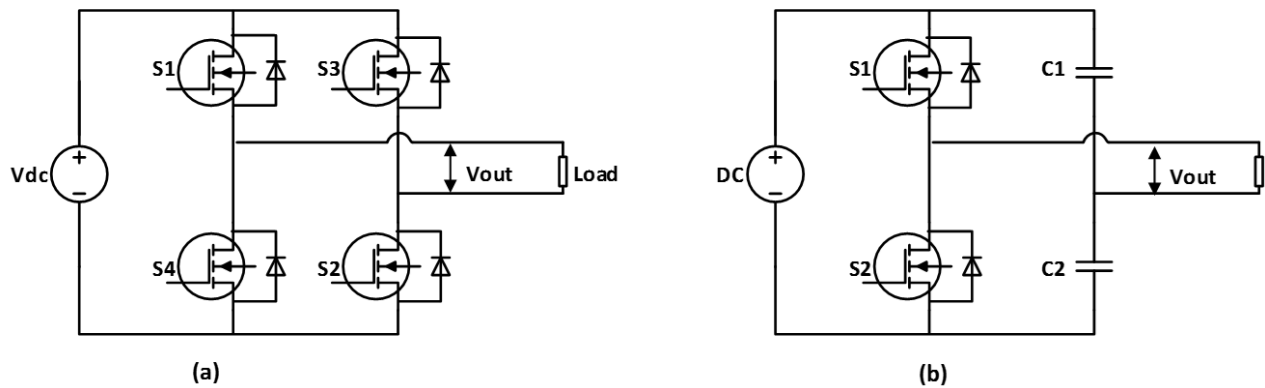


Fig. 2.11 (a) Full bridge inverter circuit (b) Half bridge inverter circuit

Depending on the power requirements, we select either full bridge topology for high power applications or half bridge topology for low power applications. Commonly MosFETs are chosen for the frequency requirements greater than 25 kHz and for up to 25 kHz operation, IGBTs are used as switching devices. The output voltage of the above shown inverters is an AC square wave, whose frequency depends on the switching frequency as shown in Fig. 2.12.

Besides this, a very popular Class-D resonant amplifier circuit as shown in Fig. 2.13 (a) is used in inductive heating applications. Unlike the half bridge inverter circuit as shown in the Fig. 2.11 (b), class-D amplifier circuit has no split capacitors connected to the DC link. The output voltage of the class-D amplifier circuit is a DC square wave with a frequency of operation equal to the switching frequency. The output voltage waveform is taken across the bottom device and the waveform is as shown in Fig. 2.13 (b).

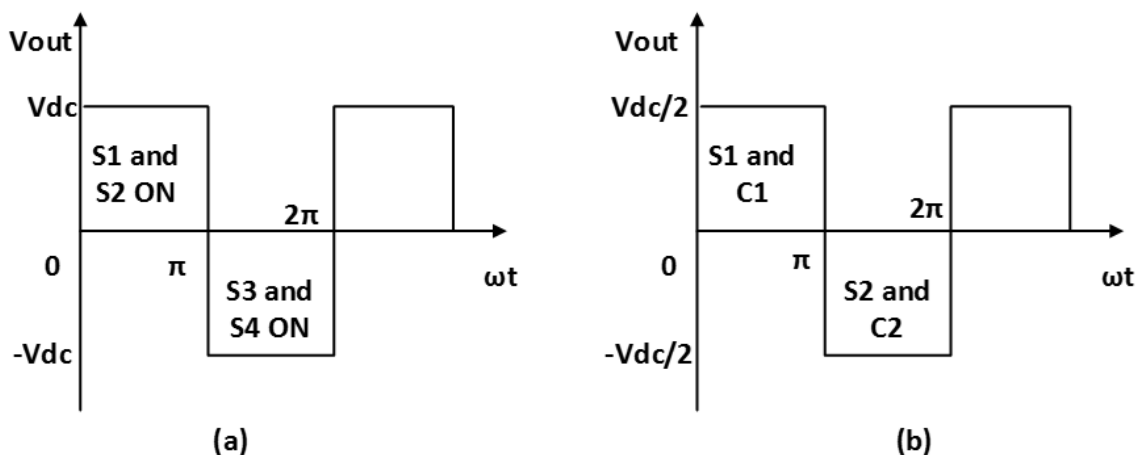


Fig. 2.12 (a) Full-bridge inverter output voltage (b) half-bridge inverter output voltage

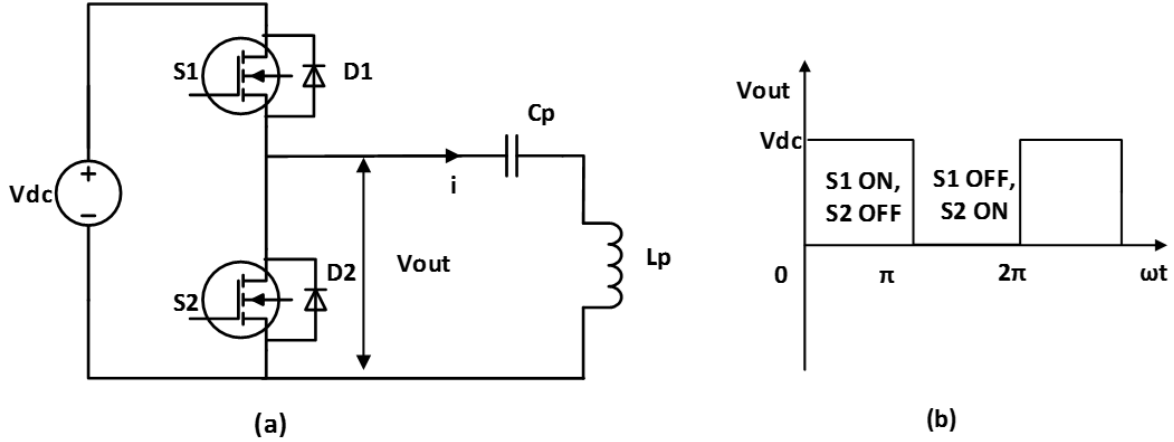


Fig. 2.13 (a) WIPT primary fed with a Class-D amplifier (b) Class-D inverter output voltage

Class-D amplifier circuit can be used for low power applications ranging up to few kW. More emphasis is given to the analysis and the soft-switching operation conditions for this inverter circuit as class-D inverter is used in this thesis work.

2.1.1 Analysis of the Class-D inverter circuit

From the Fig. 2.13 (b), the output voltage can be represented as

$$V_{out} = V_{dc} \text{ for } 0 < \omega t \leq \pi \text{ and}$$

$$0 \text{ for } \pi < \omega t \leq 2\pi \quad (2.35)$$

When we take the Fourier transform for the (2.35), we obtain

$$v_{out} = \frac{V_{dc}}{2} + \frac{2 V_{dc}}{\pi} \sum_{n=1}^{\infty} \frac{1 - (-1)^n}{2n} \sin(n\omega t) \quad (2.36)$$

Expanding the equation (2.36), we get

$$v_{out} = V_{dc} \left(\frac{1}{2} + \frac{2}{\pi} \sin\omega t + \frac{2}{3\pi} \sin 3\omega t + \frac{2}{5\pi} \sin 5\omega t + \dots \right) \quad (2.37)$$

The fundamental component of the inverter output voltage V_{out} is

$$v_{out}(\text{fundamental}) = V_m \sin \omega t, \text{ where } V_m = \frac{2 \cdot V_{dc}}{\pi} = 0.637 V_{dc} \quad (2.39)$$

If the inverter switching frequency f_s is around the value of the resonant tank frequency f_r then the impedance of the resonant circuit is very large for the higher harmonic components, therefore the current through the circuit is a sinusoidal waveform due to the fundamental voltage as given by equation (2.39). The fundamental component of the current is given as

$$i = I_m \sin (\omega t - \phi) \quad (2.40)$$

2.1.2 Working of Class-D converter under various operating scenarios

The circuit operation can be better understood with the help of the circuit waveforms under various conditions such as at $f_s=f_r$, $f_s<f_r$ and $f_s>f_r$. Where resonant frequency $f_r = \frac{1}{2\pi\sqrt{L_p * C_p}}$

Case-1: When switching frequency is equal to the resonant frequency ($f_s=f_r$)

When the class-D inverter is switched at the frequency equal to the resonant tank frequency, there exists two modes of operation as shown in the Fig. 2.14.

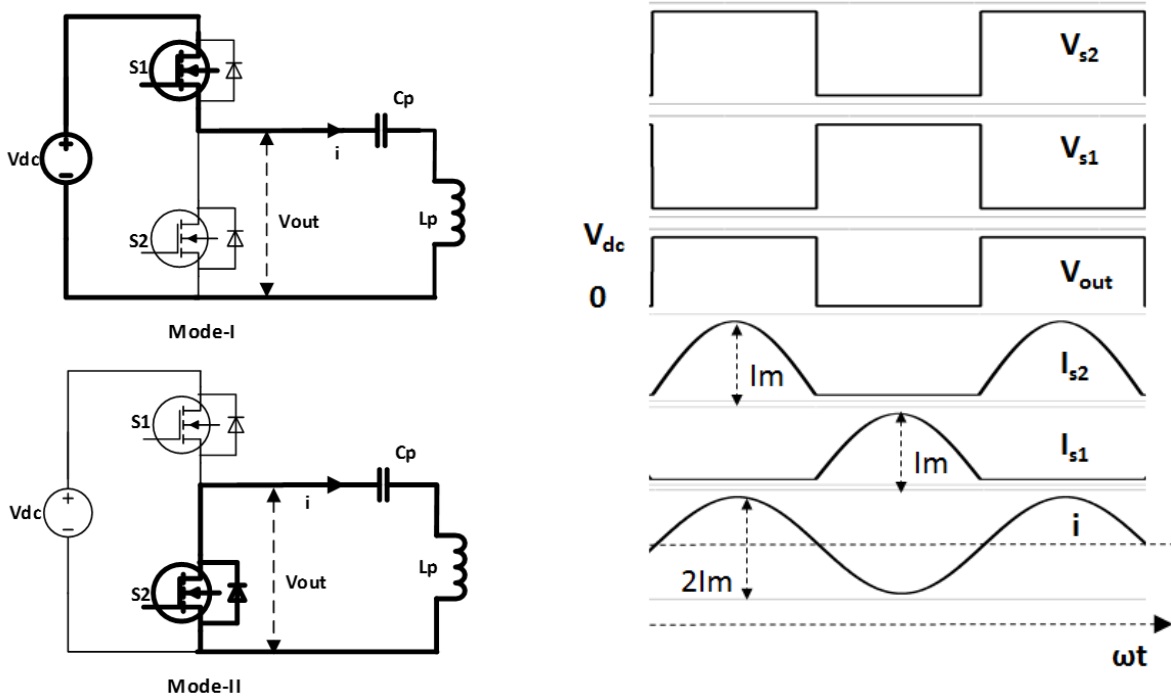


Fig. 2.14 Class-D circuit operating at $f_s=f_r$

Mode-I: In mode-I, the top switch S_1 in the inverter circuit is turned ON with a gate pulse V_{s1} . During this mode, the input voltage V_{dc} is applied at the primary tank circuit and the circuit current

path is through the device S_1 , capacitor C_p and primary coil L_p . During this mode, the capacitor will be charged.

Mode-II: In mode-II, the bottom switch S_2 in the inverter is turned ON with a gate pulse V_{s2} . During this mode, the input capacitor C_p will discharge through S_2 and L_p . Thus the current path is reversed in this mode of operation resulting in an alternating current. After the mode, S_2 is opened and S_1 is turned ON at the same time and the pattern repeats at the switching frequency.

Case-2: When switching frequency is greater than the resonant frequency ($f_s > f_r$)

When the class-D inverter is switched at the frequency greater than the resonant tank frequency, there exists four modes of operation as shown in the Fig. 2.15. As the switching frequency is higher than the resonant tank frequency, the circuit impedance becomes more inductive.

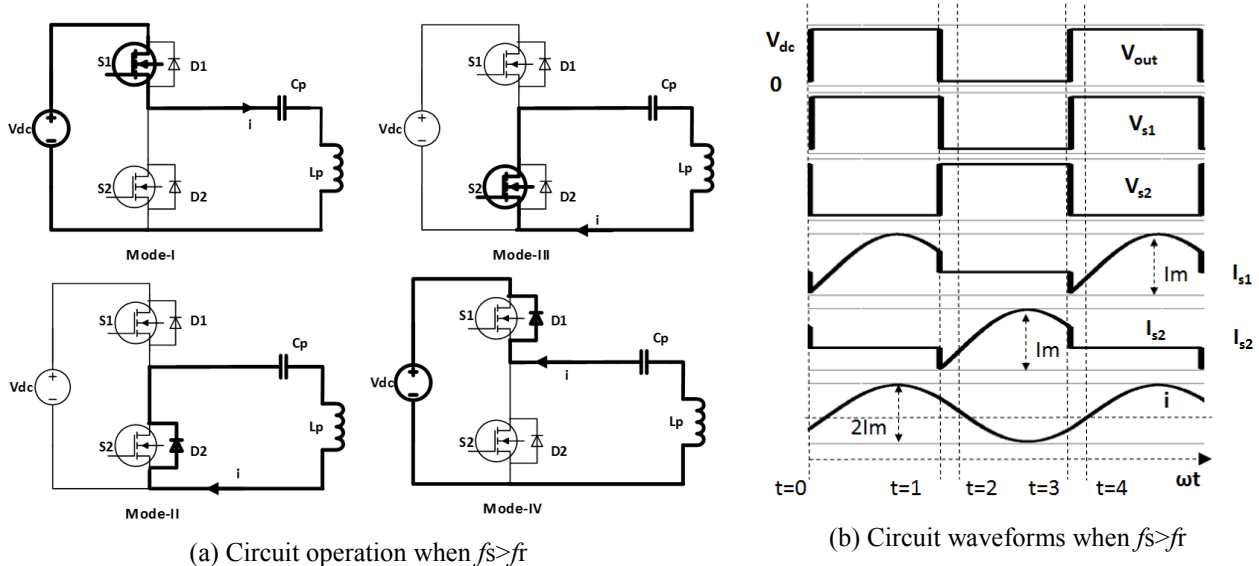


Fig. 2.15 Class-D circuit operation when $f_s > f_r$

Mode-I: In this mode of operation, the top switch S_1 in the inverter is turned ON at $t=0$ and the input voltage V_{dc} is applied to the primary tank. As the tank is more inductive, the inductor dominates the capacitor and gets charged due to current 'i' till the S_1 is turned off.

Mode-II: At $t=1$, the device S_1 is turned off. As the circuit is inductive, it will not allow the sudden change in the current path. Therefore the current flows through the diode D_2 to maintain the same current direction. During this stage, switch S_2 is turned ON while the voltage across it is almost

zero due to diode conduction. This way we can achieve zero voltage turn on (ZVS). The current flows through diode till the switch S_2 is turned ON.

Mode-III: In this mode, the inductor L_p will discharge through S_2 , and in the process charges the capacitor C_p until the switch S_2 is turned OFF.

Mode-IV: The switch S_2 is turned OFF at $t=3$. As the capacitor is fully charged, it will not allow the sudden change in the voltage. Therefore the capacitor finds its path to discharge through the diode D_1 . During this stage, the switch S_1 is turned ON again achieving the ZVS condition. After the S_1 is turned ON, the operation goes into the mode-I.

Case-3: When switching frequency is lower than the resonant frequency ($f_s < f_r$)

When the class-D inverter is switched at the frequency less than the resonant tank frequency, there exists four modes of operation as shown in the Fig. 2.16. As the switching less than the resonant tank frequency, the circuit impedance becomes more capacitive.

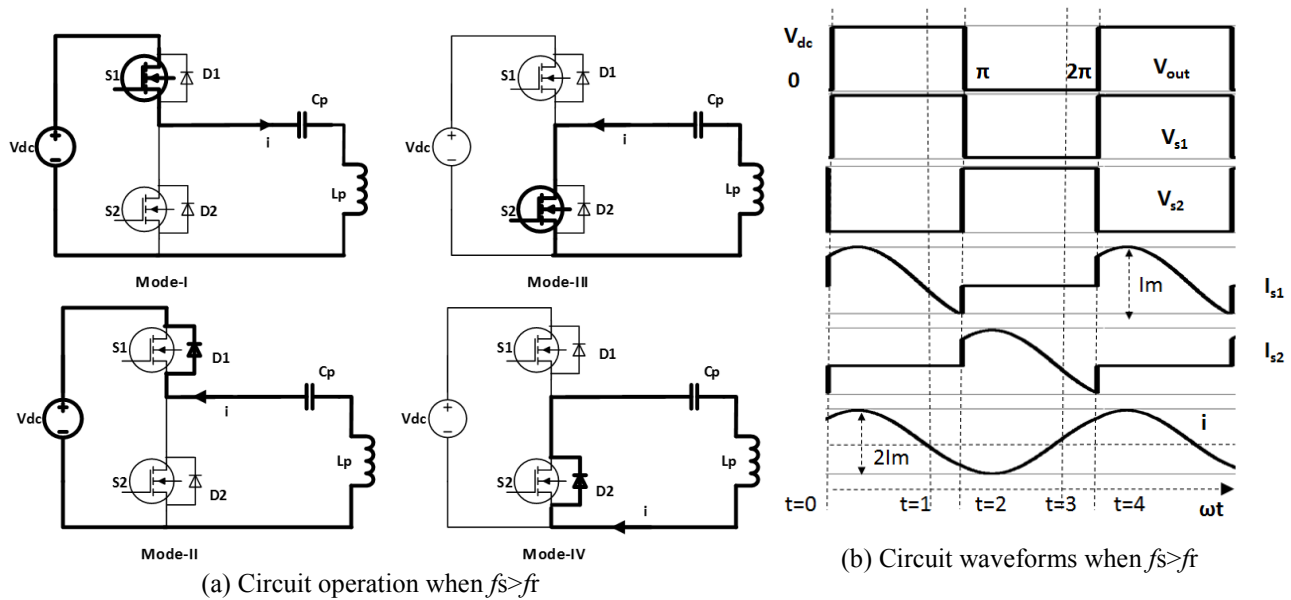


Fig. 2.16 Class-D circuit operation when $f_s < f_r$

Mode-I: In this mode of operation, the top switch S_1 in the inverter is turned ON at $t=0$ and the input voltage V_{dc} is applied to the primary tank. As the tank is more capacitive, the capacitor dominates the inductor and gets charged fully charged till $t=1$.

Mode-II: After $t=1$, the capacitor C_p will start discharging in the opposite direction through S_1 and source and charge the inductor L_p . During this stage, the switch S_1 can be turned off as the current find its path through D_1 without any interruption in the current path thus forming a zero current turn off (ZCS).

Mode-III: In this mode, the switch S_2 is turned ON. During this mode, the fully charged inductor L_p will discharge through the switch S_2 and the inductor C_p . During this process, the capacitor will get charged until the inductor is fully discharged at $t=3$. After the inductor is fully discharged, the capacitor will start discharging in the opposite detection.

Mode-IV: Here the capacitor C_p will discharge through D_1 and L_p . During this stage, the switch S_2 is turned OFF again achieving the ZCS condition. After the S_1 is turned ON, the operation goes into the mode-I.

Operating the power converter in the ZVS or ZCS conditions is very advantageous as this will reduce the switching losses and make the system more efficient. One more advantage of ZVS switching is the radiated EMI issues in the power converter will be nullified.

Chapter-3 Design of a novel magnetic power transfer system

3.1 Introduction

In the WRIPT system, energy is transferred from primary to secondary through a large airgap via high frequency magnetic field. The core component for generating this magnetic field is the magnetic power transfer system. Magnetic power transfer system is designed to have a primary or transmitter circuit that generates the high frequency magnetic flux and a secondary or receiver circuit that picks up the magnetic field from the primary and induces an EMF. The very important aspects of the design of magnetic system are

- a) To achieve highest possible coefficient of coupling between the primary and secondary.
- b) To achieve better performance in various misalignment conditions.
- c) To achieve low magnetic radiation in the operation.
- d) To have a very high power transfer efficiency.

There exists few designs of the magnetic power transfer systems in the literature that are as explained in the below section.

3.2 State of the art MPTS

Non-polarized circular electromagnetics which are derived from the pot cores are normally used for EV charging applications as proposed [32], [52], [53]. These are spiral coils or circular coils, cannot concentrate magnetic field in the confined area. Further evolutions as shown in [54][30][52] uses circular coils with ferrite disks and ferrite spokes. The optimization in use of ferrite cores and their layout are proposed [55]–[58]. The circular coil with ferrite plate is as shown in the Fig. 3.1. These circular coils work at higher frequencies and can give at best 90% efficiency as shown in [32]. The circular geometries and variants all suffer a poor mutual inductance between the primary and secondary coil compared to some other core geometries of the same diameter. The circular pads requires greater diameter as the separation or airgap between them increases. This is a bottleneck as the design requires larger real estate on the vehicle and pathway.

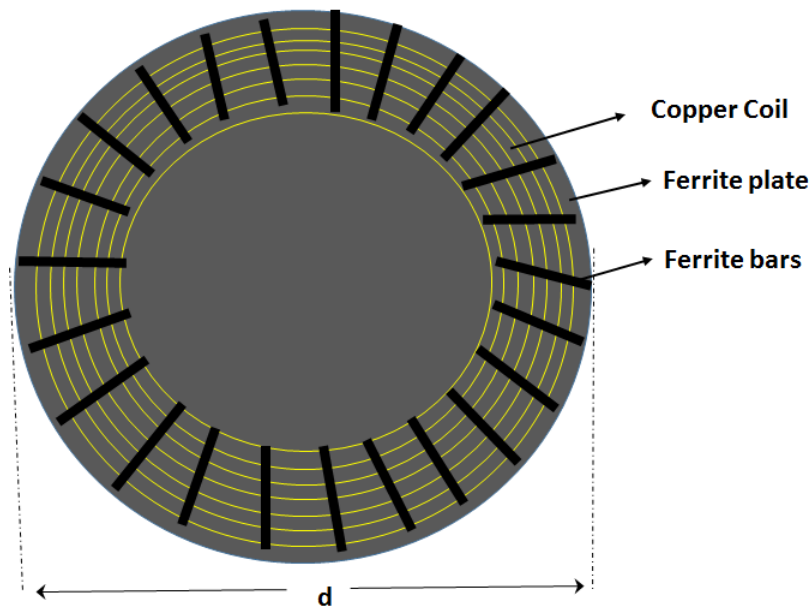


Fig. 3.1 Top view of the Circular/Spiral Coil

Flux-pipe pads are investigated as discussed in [59], [60], here the coils are wound along the H-shape formed by ferrite bars as shown in [61]. As shown, these geometries improve mutual inductance and has impressive results for power transfer efficiency upwards of 94% at 1.5 kW power transfer and 75 mm airgap. This coil topology uses a double sided flux path as discussed in the literature. Also, this coil structure has a better performance in slight misalignment conditions. However this coil geometry has a disadvantage limiting its' practical use near a substantially metal vehicles and human users due to magnetic radiation as the flux path on the outer side is radiating the non-useful flux which reduces the efficiency and increases cost due to shielding.

Besides the above discussed MPTS, there are two more popular coil topologies as shown in Fig. 3.2 Both these double D and unipolar coils with rectangular and square shapes are studied in [52], [62]–[64].

As seen in [65] the coupling coefficient and efficiency of the DD coil is better than unipolar coil. Also in the misalignment conditions, the DD coil's performance is better than the unipolar coils designs for increased secondary coil size. However both unipolar and DD coils compromise their performance for unexpected misalignment conditions and have poor pole to pole spacing, which

decreases mutual conductance compared to a U-U core of the same diameter. Coil design for better performance can be done only for misalignment assumed to certain extent.

Other bipolar geometries called DDQ and DD-DDQ coils are investigated in [66]. The proposed coil designs have a better misalignment tolerance and efficiency and has much lesser leakage flux compared to its counter parts. As discussed in [61] the power transfer efficiencies are upwards of 95% for a power transfer of >8.0 kW.

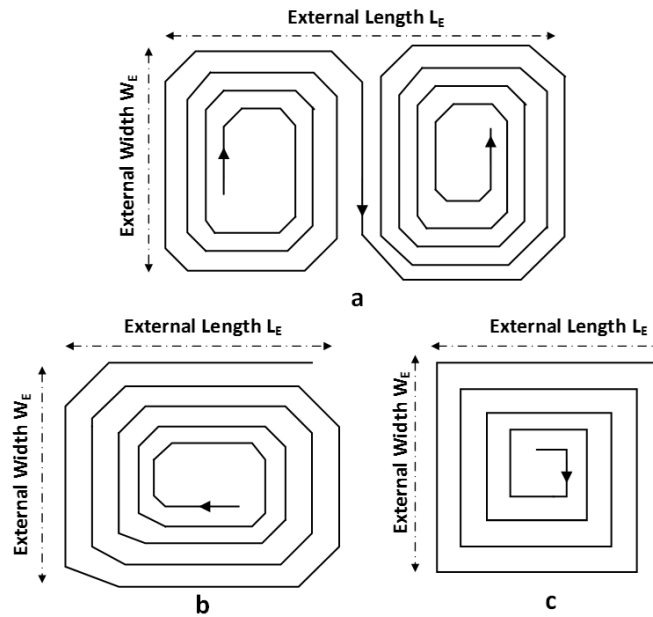


Fig.3.2 (a) Double D coil topology (b) Unipolar rectangular coil (c) Unipolar square coil

Due to large leakage magnetic flux in the system, and it being high frequency flux, it will radiate into the surrounding space. This magnetic radiation is very dangerous as it might couple with any metal part and induces an EMF that produces eddy currents. It is extremely dangerous when humans are exposed to this high frequency magnetic radiation, especially people with implanted pacemakers, etc. The radiation for any magnetic circuit design should be in a very controlled limits. The International Commission on Non-Ionizing Radiation Protection (ICNIRP) is the control body that imposes the limits for the maximum limits and frequency for the magnetic fields that a human can safely expose to.

With respect to the WRIPT, there are few standards like SAE-J2954, ISO/IEC PT 61980 that impose the safe design considerations. The main design considerations for meeting the magnetic

safety requirements is the design of coil, shielding requirement if required, maximum operating frequency.

In all the coil topologies thus far in the literature uses ferrite plates and ferrite bars to concentrate the flux between the primary and secondary coils. Also shielding techniques are proposed in few papers. For all the above seen coil designs, there exists a combination of the ferrite cores and shielding for reducing the magnetic radiation.

Ferrites can be used to concentrate the magnetic flux path and reduce the leakage flux, hence magnetic power transfer system design using ferrite materials is very advantageous. Ferrite core geometries optimized for maximum mutual inductance with a wide air gap and minimal diameter (maximum pole to pole spacing) are not explored much in the literature. As seen in [67]–[70] only very few core based designs were investigated in the literature and they have a limitation of the airgap or separation distance.

Design of a novel magnetic power transfer system is investigated in this thesis. The proposed final design helps in achieving higher power transfer efficiencies and lower magnetic radiation for larger airgaps.

3.3 Ferrite core based WRIPT options

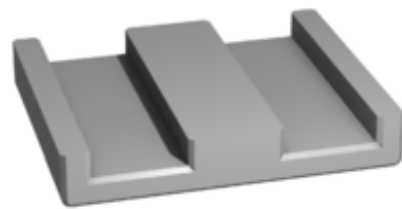
Most popularly used and off-the-shelf available ferrite core structures like E-core, I-core, ETD core, C/U core, planar E-core as shown in Fig. 3.3 are considered for initial study.



(a) E-Core



(b) I-Core



(c) Planar E Core



(d) ETD Core



(e) C/U Core

Fig. 3.3 Off-the-shelf available popular ferrite cores

Various primary and secondary combinations of the above shown core structures are considered for the study purpose as shown in the Fig. 3.4.

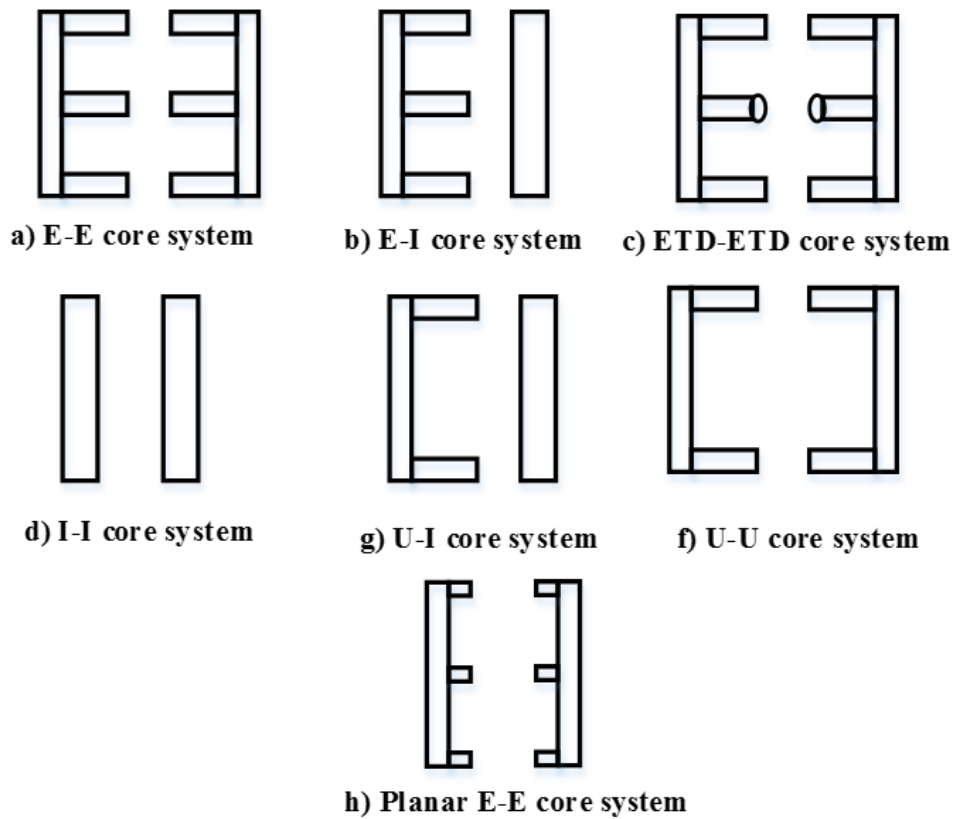


Fig. 3.4 Core structure combinations for WRIPT performance study

3.3.1 Reluctance model of the core combinations

To design the magnetic circuit for a large airgap WRIPT application with maximized mutual inductance between primary and secondary, it is very important to understand the reluctance model of the above shown core structure combinations. This helps in designing the system with actual number of turns to obtain the required self-inductance. Consider the winding on a core as shown in the Fig. 3.5.

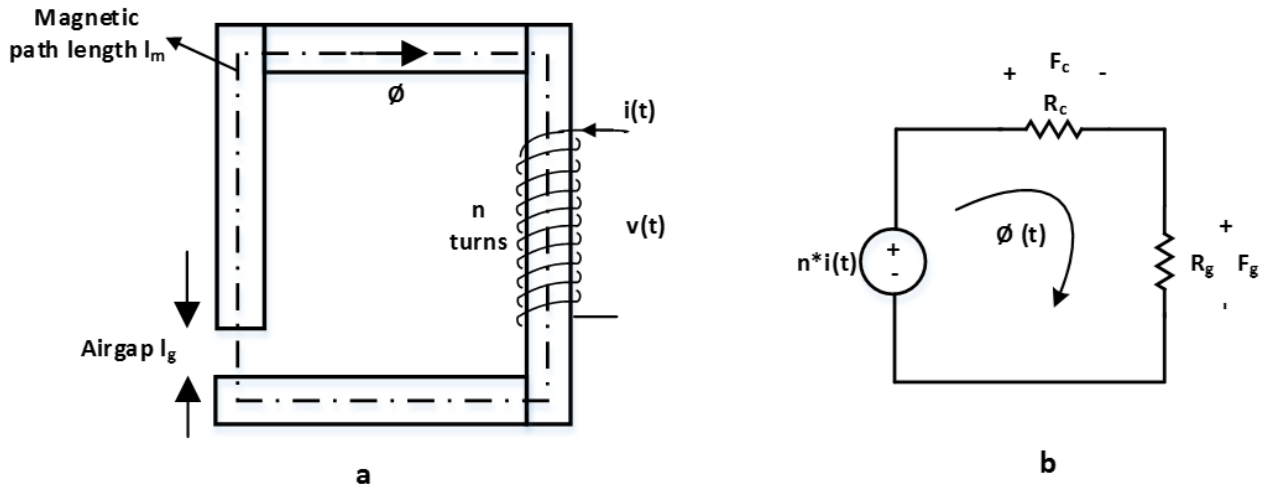


Fig. 3.5 Winding with a core with airgap l_g (a) physical model (b) magnetic circuit model

Let us consider a core with cross section area of A_c and permeability μ as shown in Fig. 3.5. Let us consider a winding with ‘n’ turns wound on one limb of the core as shown and supplied by a voltage source $v(t)$. This voltage source generates current $i(t)$ which in turn generates magnetic flux ϕ . Let the length of the magnetic path is l_m and airgap length in the core is l_g .

$$\text{We know that MMF is given by } F = H \cdot l \quad (3.1)$$

Where H is the magnetic field strength and l is the length of the magnetic path.

$$\text{But } H = B/\mu \text{ and } B = \phi/A_c \quad (3.2)$$

$$\text{Now (3.1) becomes } F = \frac{l}{\mu A_c} \phi \quad (3.3)$$

$$\text{We know that the MMF can also be expressed as } F = \phi \cdot R \quad (3.4)$$

Where R is the reluctance seen by the magnetic path.

From (3.3) and (3.4), we can express the reluctance as

$$R = \frac{l}{\mu A_c} \quad (3.5)$$

From the magnetic equivalent circuit as shown in the Fig. 3.5, we have two reluctances seen by the MMF source, one offered by the core and other due to airgap in the core.

We know that the total MMF is $n \cdot i = \phi \cdot (R_g + R_c)$

We know the self-inductance can be calculated as $L = \frac{n \cdot \phi}{i}$

Therefore inductance required can be calculated as $L = \frac{n^2}{R_c + R_g}$ (3.6)

Where, R_g is airgap reluctance, given by $R_g = \frac{l_g}{\mu_0 A_c}$ and R_c is magnetic core reluctance can be

given by $R_c = \frac{l_c}{\mu_0 \mu_r A_c}$

From the equation (3.6), we can easily design the inductor with required inductance for a given material and physical dimensions. The above design method is very easily applicable to systems with very less airgap.

3.3.2. Influence of primary and secondary cores on self-inductances

For a WRIPT system with core structures, as there are not just one but several flux paths, it is very difficult to find the length of magnetic paths. As shown in the Fig. 3.6 for an E-E core structure, there exists more than 9 reluctance paths. Mutual and self-inductances of these various winding locations is difficult to predict using conventional magnetics design formula. More importantly, the primary and secondary self-inductance are influenced by the secondary and primary cores respectively. The inductance value influence is because, the flux finds the least reluctance path through the secondary ferrite core and vice versa. Also the airgap between the two cores plays an important role determining the self and mutual inductances.

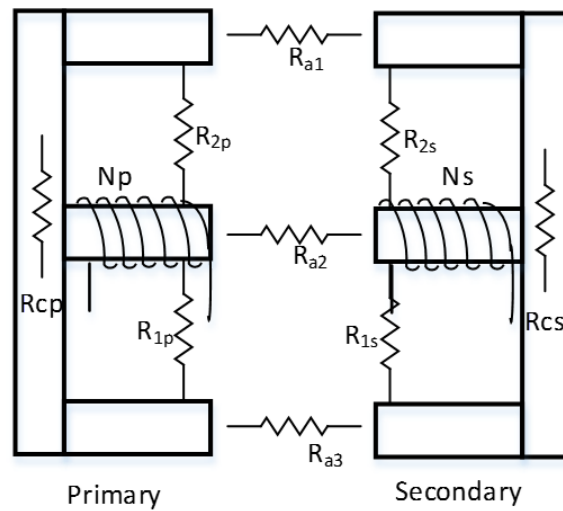


Fig. 3.6 Reluctance paths for a E-E core based WIPT system

Hence, we use finite element based software tools to understand the magnetic leakage and mutual inductance of these winding and core geometry variations. Once the mutual inductance has been maximized the coil is designed for the required inductance and the number of turns required to achieve the desired inductance. Each WRIPT combination as shown in Fig. 3.4 are considered for FEA using JMAG software package and off-the shelf available cores are used for signal power level experimental verification. Different winding combinations are also tried out and at the end of this chapter, a best candidate from the Fig. 3.4 is obtained to further proceed for 1.0 kW design requirement.

3.3.3 FEA and signal power experimentation for identifying the best core combination for WRIPT application

(1) E-E core combination

E-E core WRIPT system is explored with various winding configurations as shown in the Fig. 3.7 below.

In the FEA results, we can only see the performance of the WIPT system. This means that the magnetic leakage or flux seen is when the system is not resonating. If we can design a WIPT system that can have lower mutual inductance in the WIPT conditions, it will perform much better in WRIPT conditions as the flux interaction between primary and secondary is much better and very high during resonance.

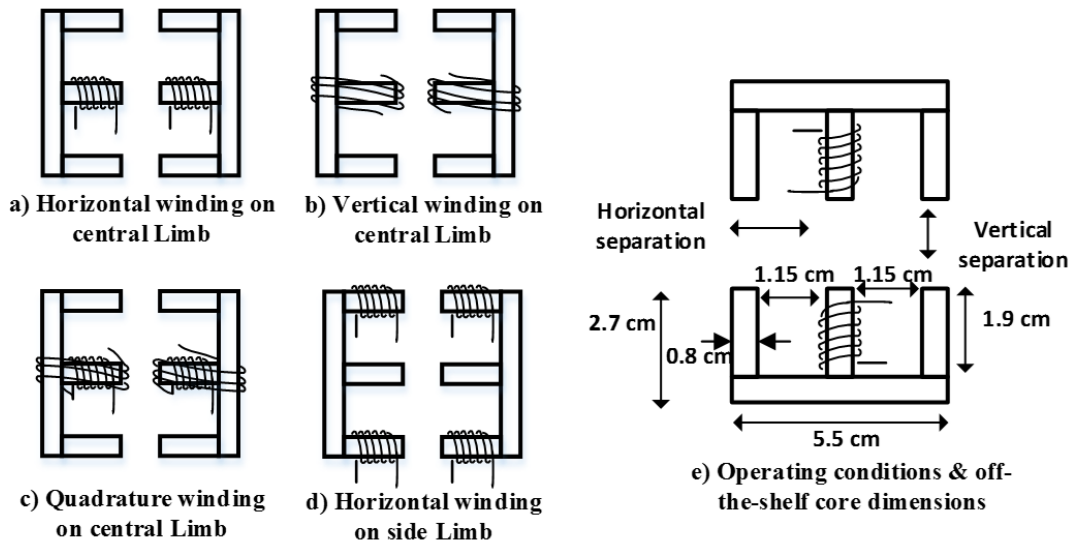


Fig. 3.7 E-E core WIPT system with various winding configurations

FEA is carried out using JMAG to analyze the self-inductance and mutual inductance of the off-the-shelf bought core structures for various airgap and misalignment conditions as shown in Fig. 3.7 (e).

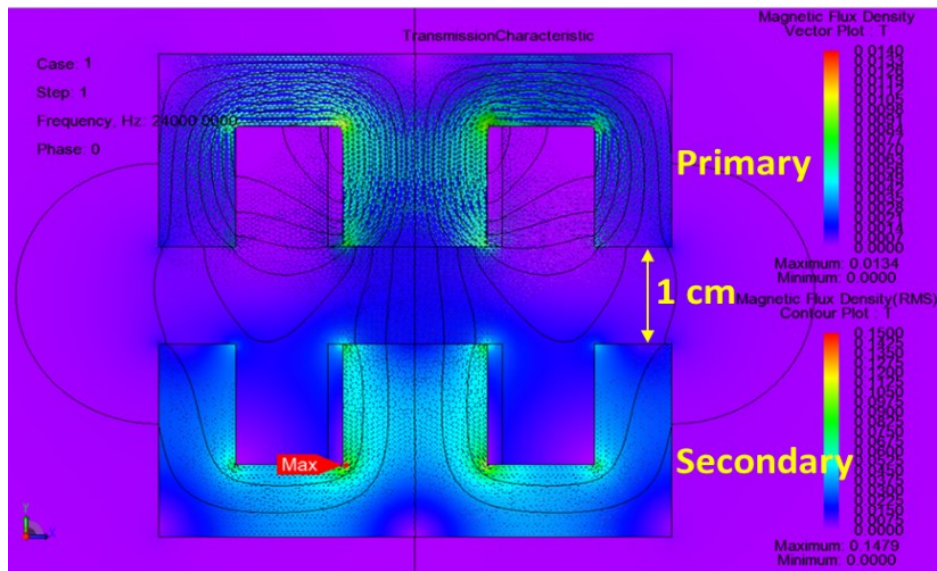


Fig. 3.8 FEA results for E-E core WIPT system with horizontal winding on the central limb at 1 cm airgap

As seen in the FEA results, for a, E-core construction and at 1 cm airgap as per Fig. 3.7 (e), the flux produced in the primary will have a very low reluctance path from its own side limbs, hence very little flux links to the secondary core. As this is the property of the E-E core construction, this

combination will be more efficient if the airgap between primary and secondary is smaller than the gap between the central and side limbs in the E-core construction. Signal power experimental verification results for various winding combinations on the E-E cores is as follows. Single strand 23 AWG magnet wire is considered for all the experiments neglecting the proximity and skin effects in all cases.

(1.a) E-E core WRIPT experimental verification

i) E-E core with horizontal winding on the central limb

E-E core with horizontal winding as per the FEA design parameters as listed in the Table-3.1 are considered for experiments at various airgaps and horizontal misalignment conditions. The self-inductance of the primary and secondary listed in Table-3.1 are measured without the secondary or primary core influence with LCR meter. All the horizontal misalignment conditions are evaluated at a fixed 1 cm vertical separation.

Table-3.1 E-E system specifications with horizontal winding on central limb

Parameter	Specification
Primary Self-Inductance	47 μ H
Primary Resistance (DC)	93 m Ω
Secondary Self-Inductance	47 μ H
Secondary Resistance (DC)	93 m Ω
Primary Compensation Capacitance	0.33 μ F
Secondary Compensation Capacitance	0.33 μ F
Operating Frequency	41.5 kHz
Load Power	10 W
Primary no. of turns	18
Secondary turns	18

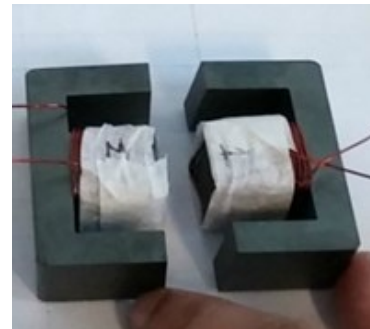


Fig. 3.9 E-E experimental core with horizontal winding on central limb

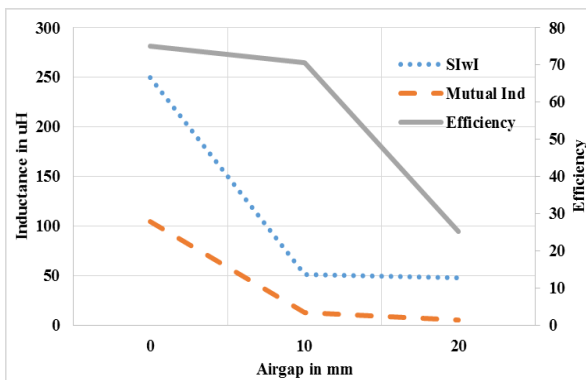


Fig. 3.10 Experimental results for vertical separation

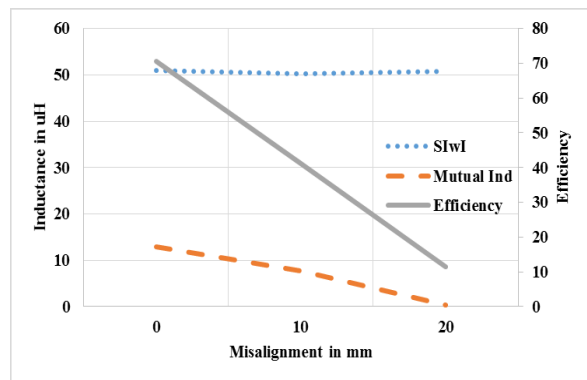


Fig. 3.11 Experimental results for horizontal misalignment at 1 cm vertical separation

SIwI refers to the self-inductance of the core with the influence of either secondary or primary cores. As seen in the above plot, the mutual inductance and power transfer efficiency are maximum at less airgap. As seen, after 10 mm, the effect of influence is almost negligible, which means that the system will have poor coupling and poor operating efficiency after this airgap. Performance is also very poor in misalignment conditions.

ii) E-E core with vertical winding on the central limb

E-E core with vertical winding as per the FEA design parameters as listed in the Table-3.2 are considered for experiments at various airgaps and horizontal misalignment conditions. The self-inductance of the primary and secondary as listed in Table-3.2 are measured without the secondary or primary core influence with LCR meter. All the horizontal misalignments are evaluated at a fixed 1 cm vertical separation.

Table-3.2 E-E system specifications with vertical winding on central limb

Parameter	Specification
Primary Self-Inductance	47 μ H
Primary Resistance (DC)	90 m Ω
Secondary Self-Inductance	47 μ H
Secondary Resistance (DC)	89 m Ω
Primary Compensation Capacitance	0.33 μ F
Secondary Compensation Capacitance	0.33 μ F
Operating Frequency	41.5 kHz
Load Power	10 W
Primary no. of turns	17
Secondary turns	17

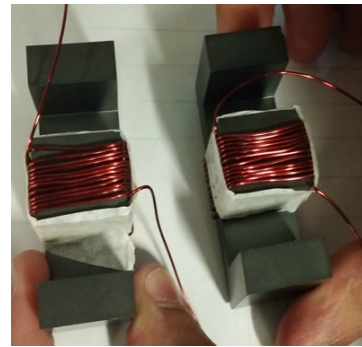


Fig. 3.12 E-E experimental core with vertical winding on central limb

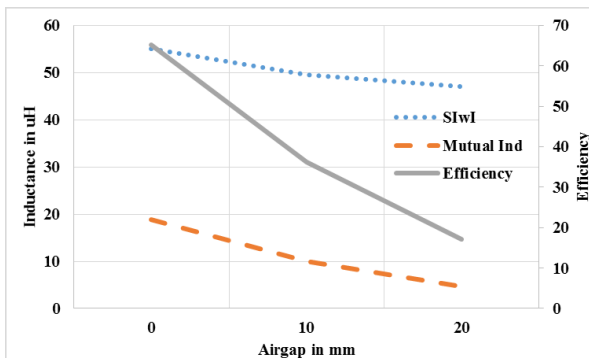


Fig. 3.13 Experimental results plot for vertical separation

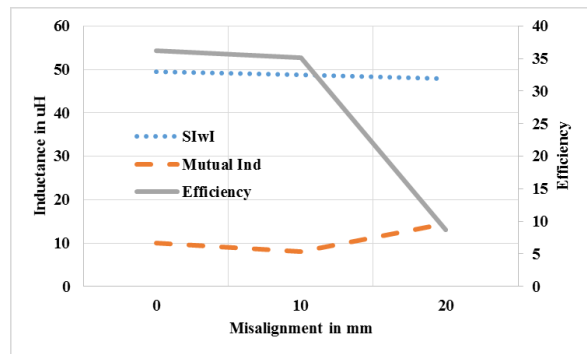


Fig. 3.14 Experimental results for horizontal misalignment at 1 cm vertical separation

iii) E-E core with horizontal winding on the side limbs

E-E core with horizontal winding as per the FEA design parameters as listed in the Table-3.3 are considered for experiments at various airgaps and horizontal misalignment conditions.

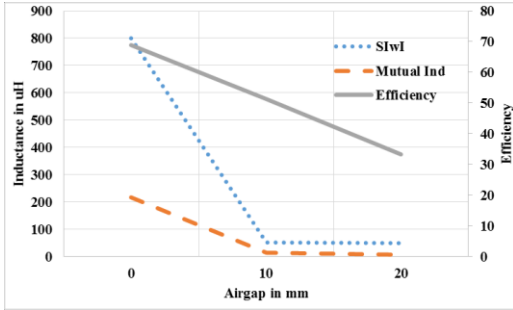


Fig. 3.15 Experimental results plot for vertical separation

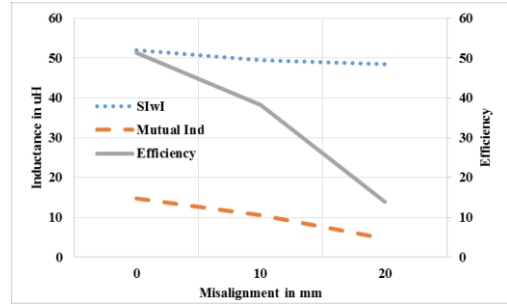


Fig. 3.16 Experimental results for horizontal misalignment at 1 cm vertical separation

Table-3.3 E-E system specifications with horizontal winding on side limbs

Parameter	Specification
Primary Self-Inductance	47 μ H
Primary Resistance (DC)	132 m Ω
Secondary Self-Inductance	47 μ H
Secondary Resistance (DC)	136 m Ω
Primary Compensation Capacitance	0.33 μ F
Secondary Compensation Capacitance	0.33 μ F
Operating Frequency	41.5 kHz
Load Power	10 W
Primary no. of turns	11 on left +12 on right
Secondary turns	11 on left +12 on right

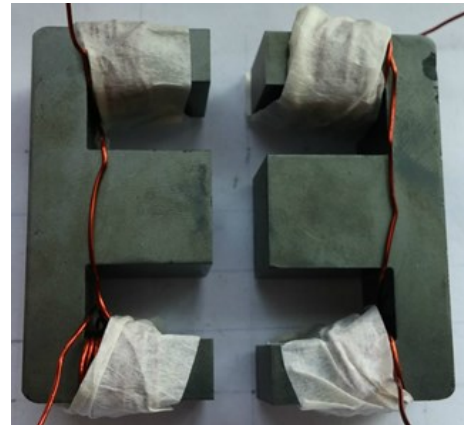


Fig. 3.17 E-E experimental core with horizontal winding on side limbs

iv) E-E core with quadrature winding on the central limb

E-E core with horizontal winding as per the FEA design parameters as listed in the Table-3.4 are considered for experiments at various airgaps and horizontal misalignment conditions.

Table-3.4 E-E system specifications with quadrature winding on central limb

Parameter	Specification
Primary Self-Inductance	47 μ H
Primary Resistance (DC)	93 m Ω
Secondary Self-Inductance	47 μ H
Secondary Resistance (DC)	103 m Ω
Primary Compensation Capacitance	0.33 μ F
Secondary Compensation Capacitance	0.33 μ F
Operating Frequency	41.5 kHz
Load Power	10 W
Primary no. of turns	11 vertical + 11 horizontal
Secondary turns	11 vertical + 11 horizontal



Fig. 3.18 E-E experimental core with quadrature winding on central limb

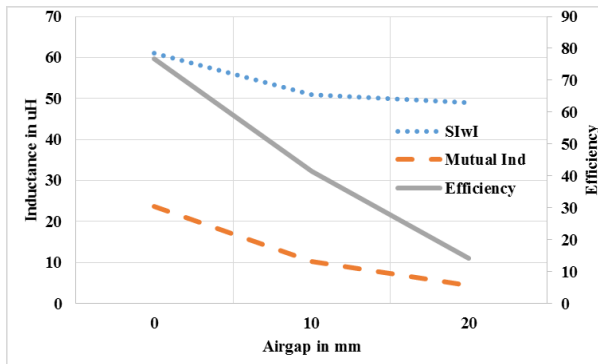


Fig. 3.19 Experimental results plot for vertical separation

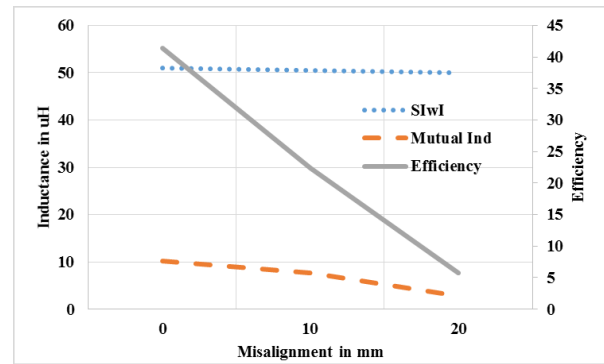


Fig. 3.20 Experimental results for horizontal misalignment at 1 cm vertical separation

(1.b) Conclusions on E-E core WRIPT system

As observed from the FEA results and the experimental results, the E-E WRIPT system has a larger leakage flux at larger airgaps. It cannot perform well in the larger airgaps and misalignment conditions. For larger airgap the E core design required is very large which is very expensive and calls for more real estate in the design.

If we were to use E-E core system, system with horizontal winding on the central limb is better choice. However only for a very small distance applications depending on the physical size of the core.

(2) E-I core combination

E-I core system here consists of an E-core with a horizontal winding on the central limb and I core also with a horizontal winding on the center of the core as shown in the Fig. 3.21 (a).

FEA is carried out using JMAG to analyze the self-inductance and mutual inductance for the off-the-shelf bought core structures for various airgap and misalignment conditions as shown in Fig. 3.21 (b).

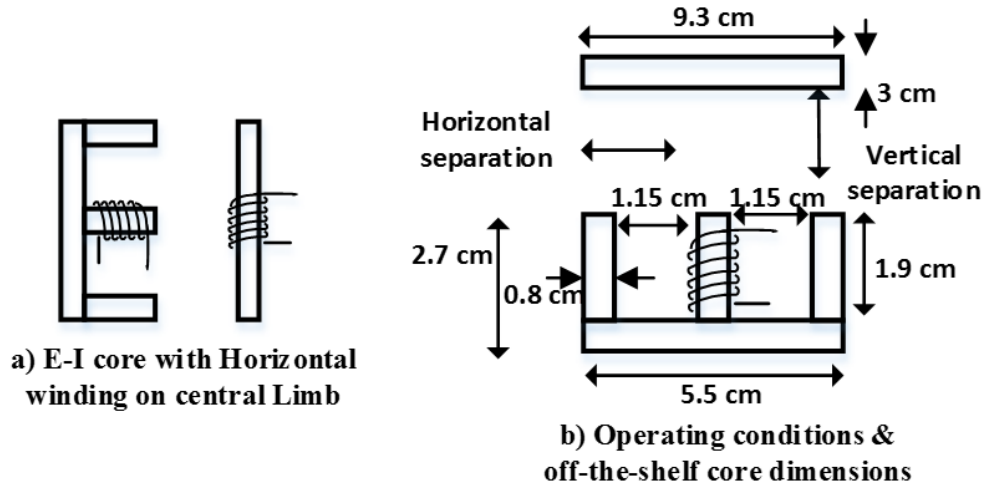


Fig. 3.21 E-I core WIPT system

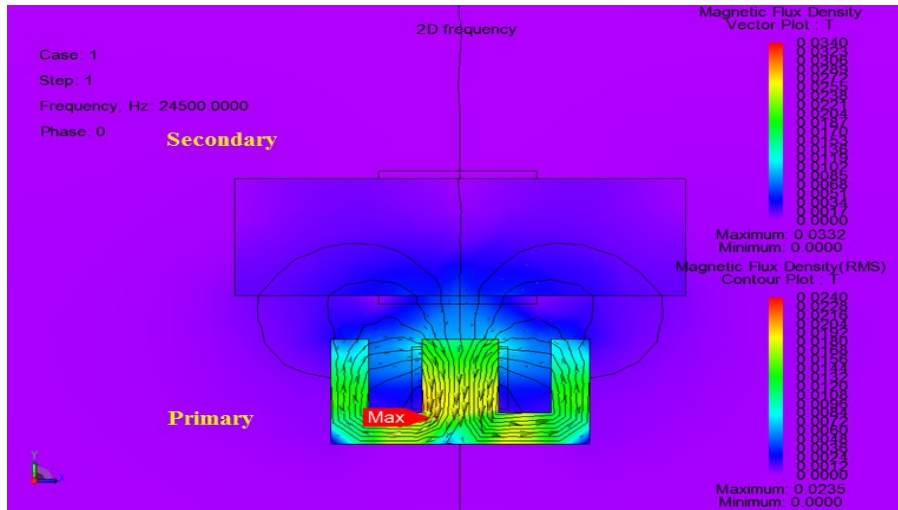


Fig. 3.22 FEA of E-I core WIPT system at 1.5 cm airgap

(2.a) E-I core WRIPT experimental verification

i) E-I core with horizontal winding on the central limb

E-I core with horizontal winding as per the FEA design parameters as listed in the Table-3.5 are considered for experiments at various airgaps and horizontal misalignment conditions. The self-

inductance of the primary and secondary listed in Table-3.5 are measured without the secondary or primary core influence with LCR meter. All the horizontal misalignments are evaluated at a fixed 1 cm vertical separation.

Table-3.5 E-I system specifications with horizontal winding on central limb

Parameter	Specification
Primary Self-Inductance	47 μ H
Primary Resistance (DC)	101 $m\Omega$
Secondary Self-Inductance	47 μ H
Secondary Resistance (DC)	104 $m\Omega$
Primary Compensation Capacitance	0.33 μ F
Secondary Compensation Capacitance	0.33 μ F
Operating Frequency	41.5 kHz
Load Power	10 W
Primary no. of turns	17 turns on E-core
Secondary turns	14 turns on I-core



Fig. 3.23 E-E experimental core with quadrature winding on central limb

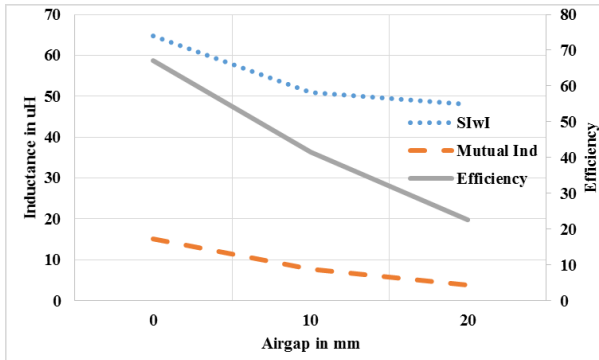


Fig. 3.24 Experimental results plot for vertical separation

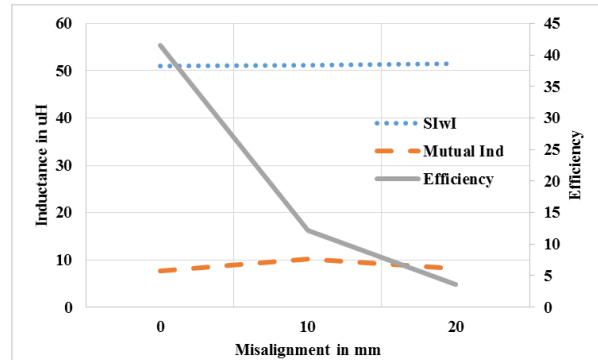


Fig. 3.25 Experimental results for horizontal misalignment at 1 cm vertical separation

(2.b) Conclusions on E-I core system

From the FEA results, we can observe that the leakage inductance is high for even a smaller airgap. At the larger airgaps, the leakage flux is larger as due to the primary being E-core. Also, from the the experimental results, the efficiency of the system is very poor at the larger airgaps. In the misalignment conditions the system system efficiency is very bad.

It is very clear from the above conclusions that the E-I core is not a potential candidate for the future investigation.

(3) Planar E-E core combination

Planar E-E core system here consists of a planar E-core having a vertical winding wound on the window area of the core as shown in the Fig. 3.26. FEA is carried out using JMAG to analyze the

self-inductance and mutual inductance of the off-the-shelf bought core structures for various airgap and misalignment conditions.

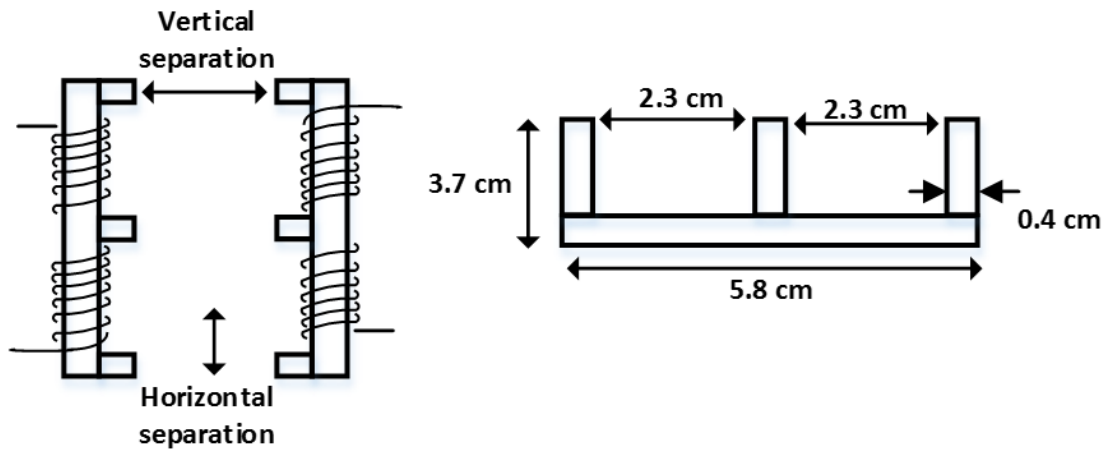


Fig. 3.26 Planar E-E core WIPT system

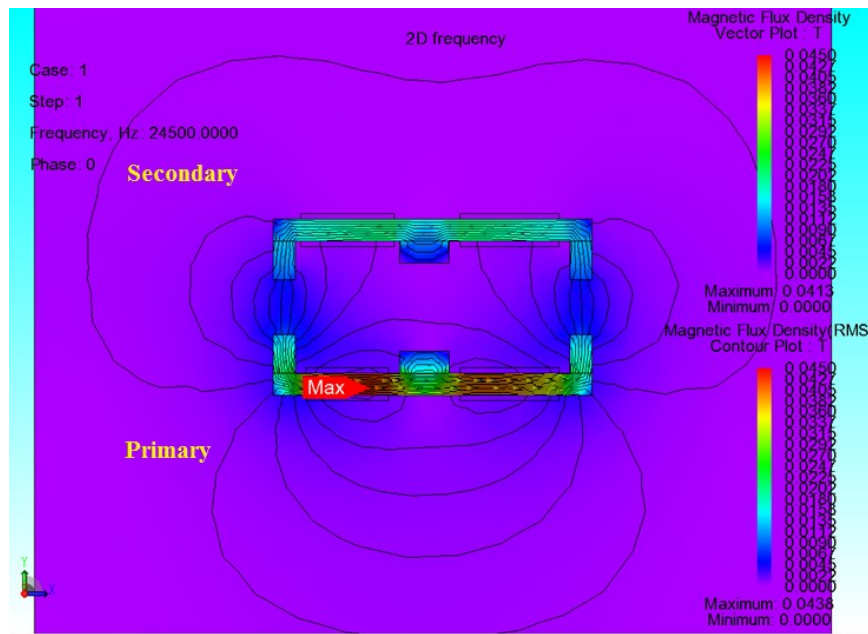


Fig. 3.27 FEA results for the Planar E-E core WIPT system at 1.5 cm airgap

(3.a) Planar E-E core WRIPT experimental verification

The self-inductance of the primary and secondary listed in Table-3.6 are measured without the secondary or primary core influence with LCR meter. All the horizontal misalignments are evaluated at a fixed 1 cm vertical separation.

Table-3.6 Planar E-E system specifications with vertical winding on window area

Parameter	Specification
Primary Self-Inductance	47 μ H
Primary Resistance (DC)	110 m Ω
Secondary Self-Inductance	47 μ H
Secondary Resistance (DC)	107 m Ω
Primary Compensation Capacitance	0.33 μ F
Secondary Compensation Capacitance	0.33 μ F
Operating Frequency	41.5 kHz
Load Power	10 W
Primary no. of turns	19
Secondary turns	19

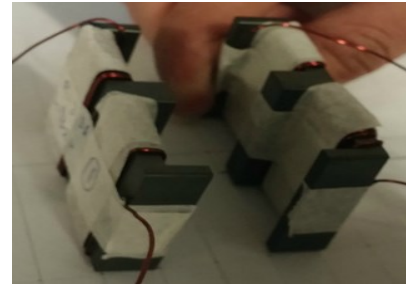


Fig. 3.28 Planar E-E experimental core with vertical winding on window area

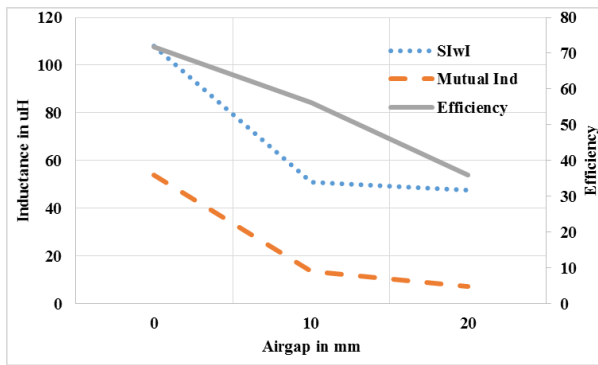


Fig. 3.29 Experimental results plot for vertical separation

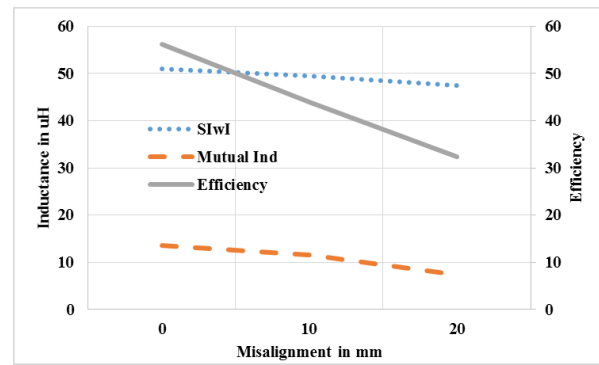


Fig. 3.30 Experimental results for horizontal misalignment at 1 cm vertical separation

(3.b) Conclusions on Planar E-E core system

The planar E-E WRIPT system has a fairly reduced leakage flux, however the leakage increases at larger airgaps. Depending on the physical dimensions, planar E-E structure is good for the smaller distances.

(4) ETD-ETD core combination

ETD-ETD core is similar to the E-E WIPT system. ETD-ETD system results are more or less very close to the E-E system results. As seen, for adopting this system, the physical size will be huge for the given airgap separation. Also the performance in misalignment conditions are very poor as seen from below compiled results.

(5) I-I core combination

I-I core WIPT system with horizontal winding is wound on the center of the core as shown in the Fig. 3.31. FEA is carried out using JMAG to analyze the self-inductance and mutual inductance of the off-the-shelf bought core structures for various airgap and misalignment conditions.

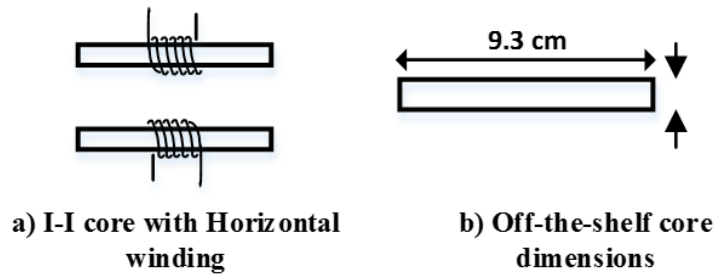


Fig. 3.31 I-I Core WIPT system

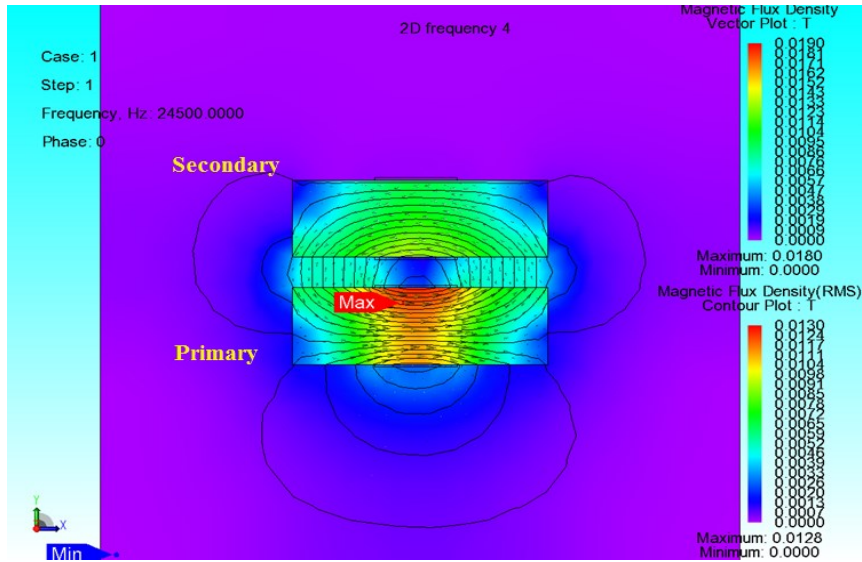


Fig. 3.32 FEA results for the I-I core WIPT system at 1.5 cm airgap

(5.a) I-I core WRIPT experimental verification

The self-inductance of the primary and secondary listed in Table-3.7 are measured without the secondary or primary core influence with LCR meter. All the horizontal misalignments are evaluated at a fixed 1 cm vertical separation.

Table-3.7 I-I core system specifications with horizontal winding on window area

Parameter	Specification
Primary Self-Inductance	47 μ H
Primary Resistance (DC)	104 m Ω
Secondary Self-Inductance	47 μ H
Secondary Resistance (DC)	102 m Ω
Primary Compensation Capacitance	0.33 μ F
Secondary Compensation Capacitance	0.33 μ F
Operating Frequency	41.5 kHz
Load Power	10 W
Primary no. of turns	14
Secondary turns	14

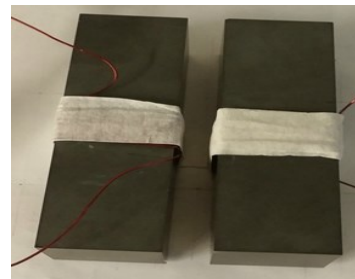


Fig. 3.33 I-I experimental cores with horizontal winding on window area

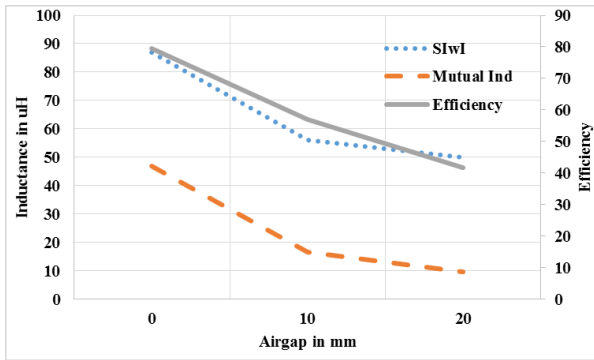


Fig. 3.34 Experimental results plot for vertical separation

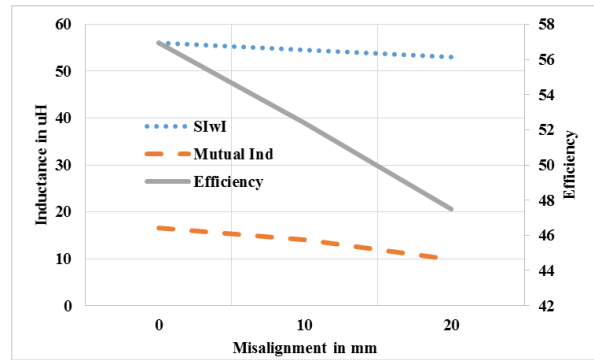


Fig. 3.35 Experimental results for horizontal misalignment at 1 cm vertical separation

(5.b) Conclusions on I-I core system

As observed from the FEA results and the experimental results, I-I WIPT system seems to be a potential candidate for the final design, however the size required for the required airgap is very big as seen from experiments. From the FEA results we can see that the leakage inductance is very less. This is due to the very large core cross section area.

For low airgap applications, this system is ideal.

(6) U-I core combination

U-I core combination with horizontal winding as shown in the Fig. 3.36 is considered for the FEA and experimental verifications.

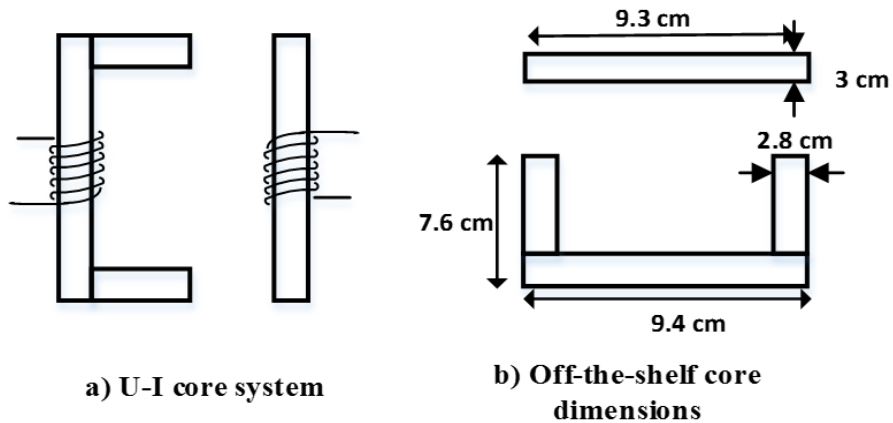


Fig. 3.36 U-I Core WIPT system

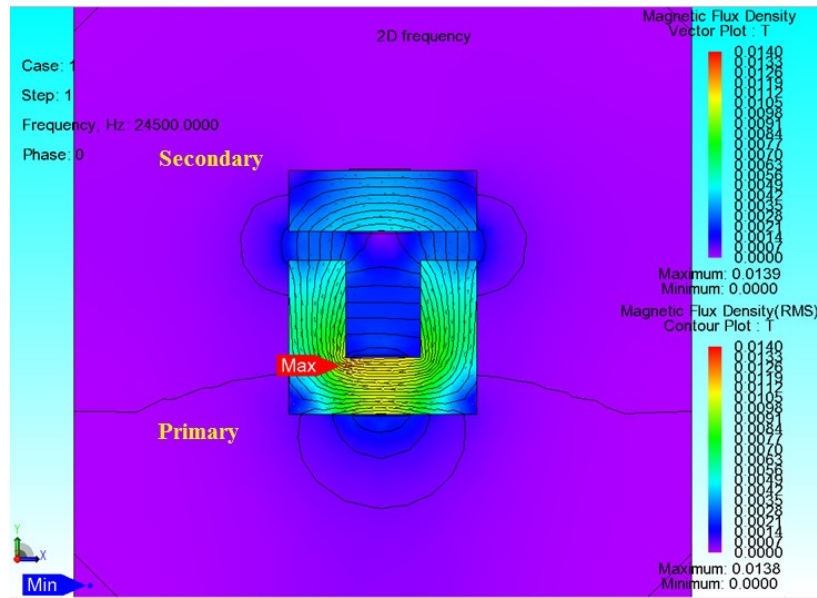


Fig. 3.37 FEA results of the U-I core WIPT system at 1.5 cm airgap

(6.a) U-I core WRIPT experimental verification

The self-inductance of the primary and secondary listed in Table-3.8 are measured without the secondary or primary core influence with LCR meter. All the horizontal misalignments are evaluated at a fixed 1 cm vertical separation.

Table-3.8 U-I core system specifications with horizontal winding on window area

Parameter	Specification
Primary Self-Inductance	47 μ H
Primary Resistance (DC)	104 m Ω
Secondary Self-Inductance	47 μ H
Secondary Resistance (DC)	102 m Ω
Primary Compensation Capacitance	0.33 μ F
Secondary Compensation Capacitance	0.33 μ F
Operating Frequency	41.5 kHz
Load Power	10 W
Primary no. of turns	14
Secondary turns	14

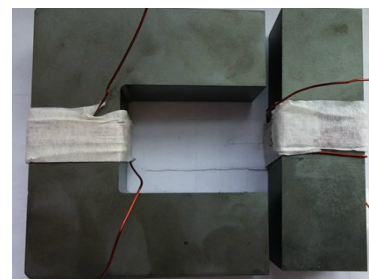


Fig. 3.38 U-I experimental core with horizontal winding

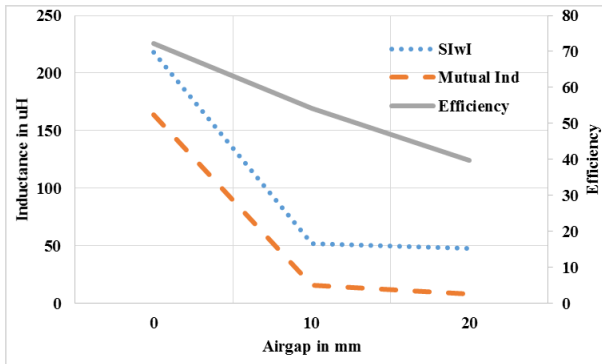


Fig. 3.39 Experimental results plot for vertical separation

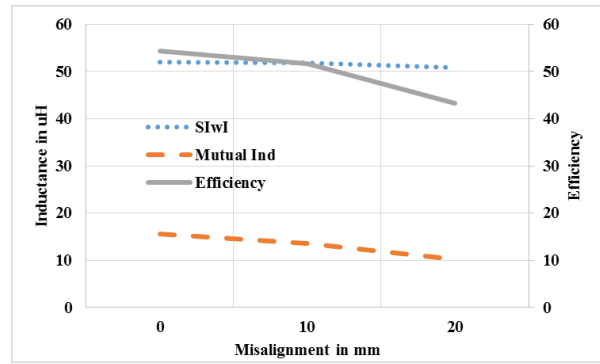


Fig. 3.40 Experimental results for horizontal misalignment at 1 cm vertical separation

(6.b) Conclusions on U-I core system

From FEA results, the leakage flux is not very much and the experimental results show that the performance in misalignment conditions and efficiency at the larger airgaps is better than the previous core systems.

(7) U-U core combination

U-U core combination with horizontal winding on the central limb as shown in the Fig. 3.41 is considered for the FEA and experimental verifications.

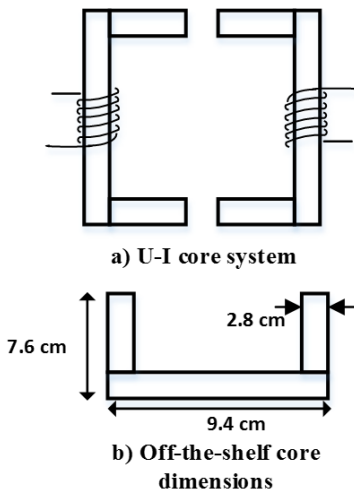


Fig. 3.41 U-U core WIPT system

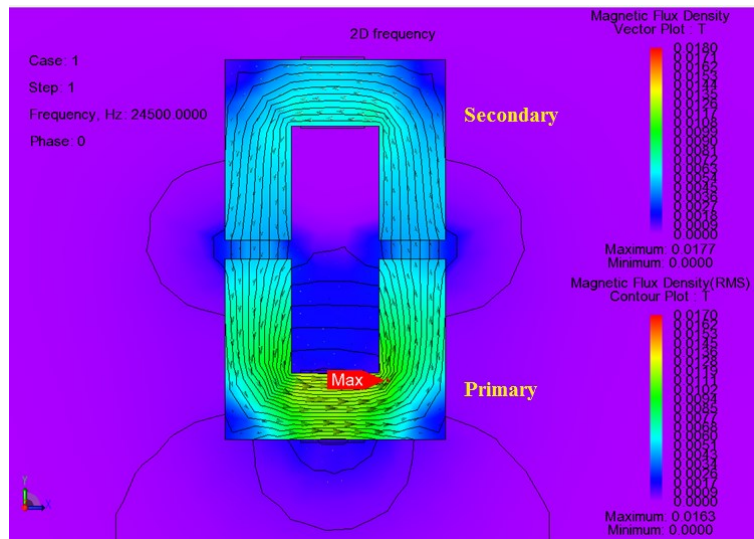


Fig. 3.42 FEA results of U-U core WIPT systems

(7.a) U-U core WRIPT experimental verification

The self-inductance of the primary and secondary listed in Table-3.9 are measured without the secondary or primary core influence with LCR meter. All the horizontal misalignments are evaluated at a fixed 1 cm vertical separation.

Table-3.9 U-U core system specifications with horizontal winding on window area

Parameter	Specification
Primary Self-Inductance	47 μ H
Primary Resistance (DC)	94 m Ω
Secondary Self-Inductance	47 μ H
Secondary Resistance (DC)	92 m Ω
Primary Compensation Capacitance	0.33 μ F
Secondary Compensation Capacitance	0.33 μ F
Operating Frequency	41.5 kHz
Load Power	10 W
Primary no. of turns	11
Secondary turns	11

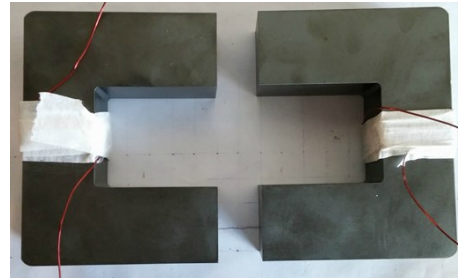


Fig. 3.43 U-I experimental core with horizontal winding

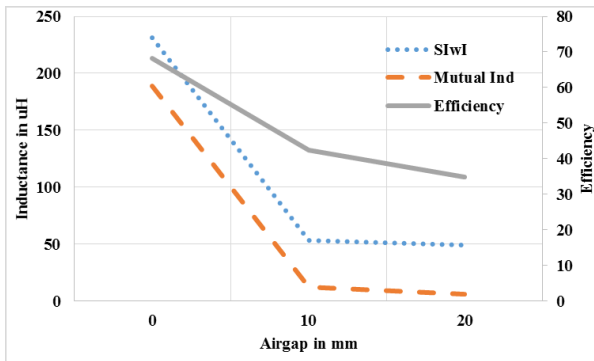


Fig. 3.44 Experimental results plot for vertical separation

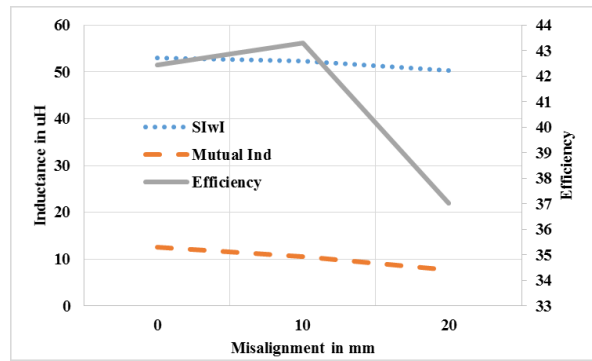


Fig. 3.45 Experimental results for horizontal misalignment at 1 cm vertical separation

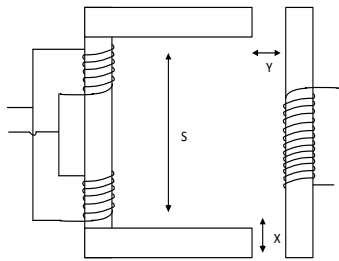
(7.b) Conclusions on U-U core system

From FEA results, the leakage flux is not very much and the experimental results show that the performance in misalignment conditions and efficiency at the larger airgaps is better than the previous core systems.

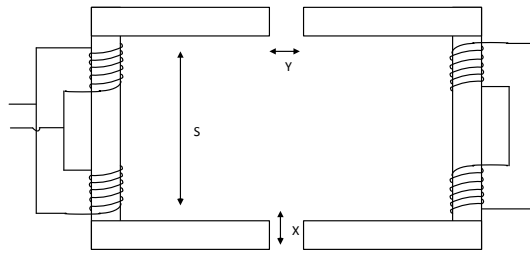
3.3.4 Further investigations on the potential candidates identified in section 3.33.

From the FEA and experimental analysis in section 3.33, we can conclude that the U-I and U-U core structures perform well for long distance WRIPT applications. Also they show a better performance in the misalignment conditions. Further investigations are carried out to conclude on the final 1.0 kW system design.

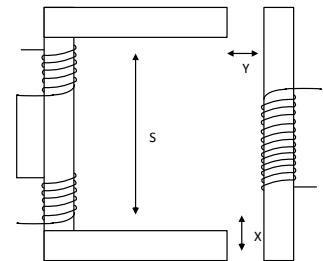
The U-I and U-U core WRIPT combinations are further investigated with the different possible split winding combinations. When the primary and secondary coils are split into two groups each, they form two separate magnetic poles each of the primary and secondary. As the two split windings are connected in series, the net leakage inductance per strand will increase while when connected in parallel, this effect decreases. Here, we study the filed shaping to maximize the coupling of the primary and secondary in WRIPT applications. Thus helping to develop a strategic winding combination for more mutual flux and less leakage inductance for higher efficiencies.



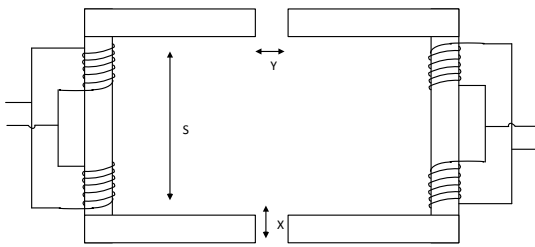
(a) U-I core with multiple windings in parallel on U core central limb



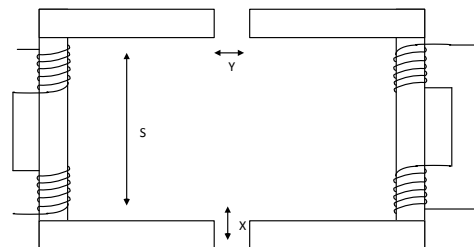
(b) U-U core with multiple windings on central limb in parallel on primary and series on secondary



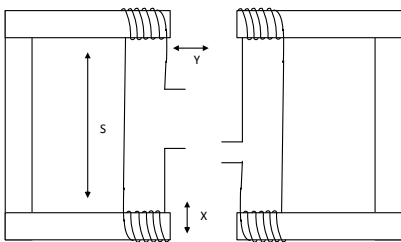
(c) U-I core with multiple windings in series on U core central limb



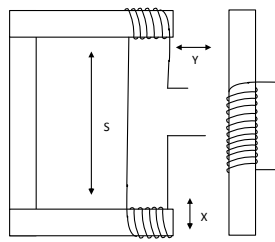
(d) U-U core with multiple windings in parallel on central limbs



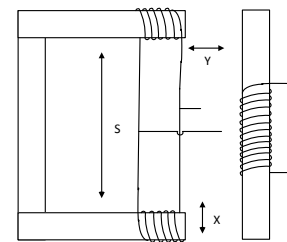
(e) U-U core with multiple windings in series on central limbs



(f) U-U core with multiple windings in series on side limbs



(g) U-I core with multiple windings on U core in series on side limbs



(h) U-I core with multiple windings in parallel on U core side limbs



(i) U-U core with multiple windings in parallel in primary and series in secondary on side limbs

(j) U-U core with multiple windings in parallel on both primary and secondary on side limbs

Fig. 3.46 U-U and U-I WRIPT system combinations.

Various possible winding combinations are tried out on the same off-the-shelf U and I cores used in section 3.33. From the possible configurations as seen in the Fig. 3.46, the best candidate with higher power transfer efficiency and better performance in misalignment conditions is identified based on FEA analysis and experimental results.

3.3.4.1 Design criteria for lower leakage inductance and higher power transfer efficiency.

The amount of useful flux linkage depends on the separation of pole facing 's' as shown in Fig. 3.46. If the pole facing separation 'S' is greater than at least 2 times the vertical air gap 'Y', the power transfer will be very efficient. This way one can design the air gap between vehicle secondary and pathway primary. The horizontal air gap can be handled using proximity sensors and advanced control strategies.

As there will be an influence of secondary core on primary, the self-inductance, leakage inductance and mutual inductance keep changing as the air gap varies. This effect is true for primary as well. Hence the air gap distances 'X', 'Y' and pole separation 'S' are very crucial in design. As there is an air gap between the primary and secondary cores, the core loss due to core saturation like in conventional transformers is eliminated.

(1) U-I core with multiple windings in parallel on U core central limb

U-I core combination consists of primary U-core with split winding wound horizontally on central limb, connected in parallel and horizontal winding wound on I-core as shown in the Fig. 3.46(a) is considered for the FEA and experimental verifications.

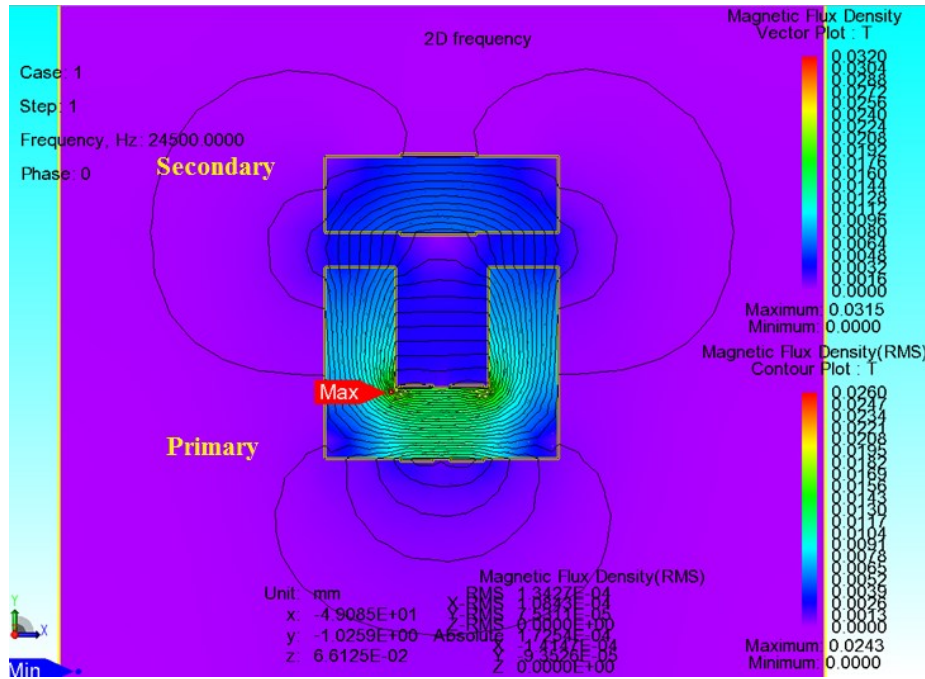


Fig. 3.47 FEA results for the U-I WIPT system with split winding on U core connected in parallel

(1.a) Experimental verification in WRIPT scenario

The self-inductance of the primary and secondary listed in Table-3.10 are measured without the secondary or primary core influence with LCR meter. All the horizontal misalignments are evaluated at a fixed 1 cm vertical separation.

Table-3.10 U-I core system specifications with split winding on U-core connected in parallel

Parameter	Specification
Primary Self-Inductance	48 μ H
Primary Resistance (DC)	48 m Ω
Secondary Self-Inductance	47 μ H
Secondary Resistance (DC)	93 m Ω
Primary Compensation Capacitance	0.33 μ F
Secondary Compensation Capacitance	0.33 μ F
Operating Frequency	41.5 kHz
Load Power	10 W
Primary no. of turns	12+13
Secondary turns	14

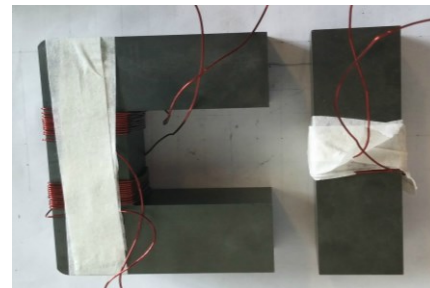


Fig. 3.48 U-I experimental core with parallel split winding on U-core central limb

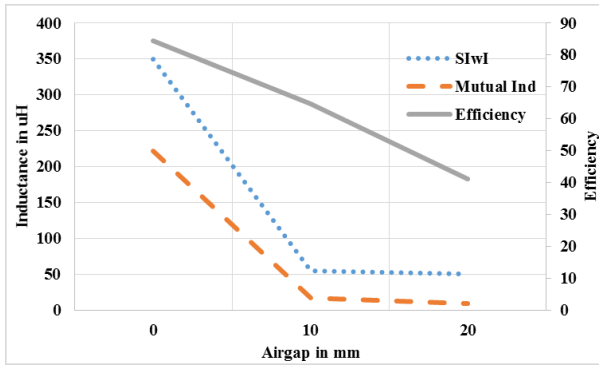


Fig. 3.49 Experimental results plot for vertical separation

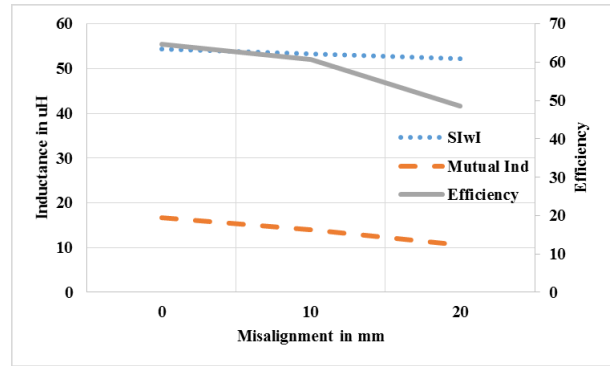


Fig. 3.50 Experimental results for horizontal misalignment at 1 cm vertical separation

(2) U-U core with multiple windings in parallel on primary and series on secondary, both placed on central limb

U-U core combination consists of primary U-core with split winding wound horizontally on central limb, connected in parallel and split horizontal winding wound in series on secondary U-core as shown in the Fig. 3.46 (b) is considered for the FEA and experimental verifications.

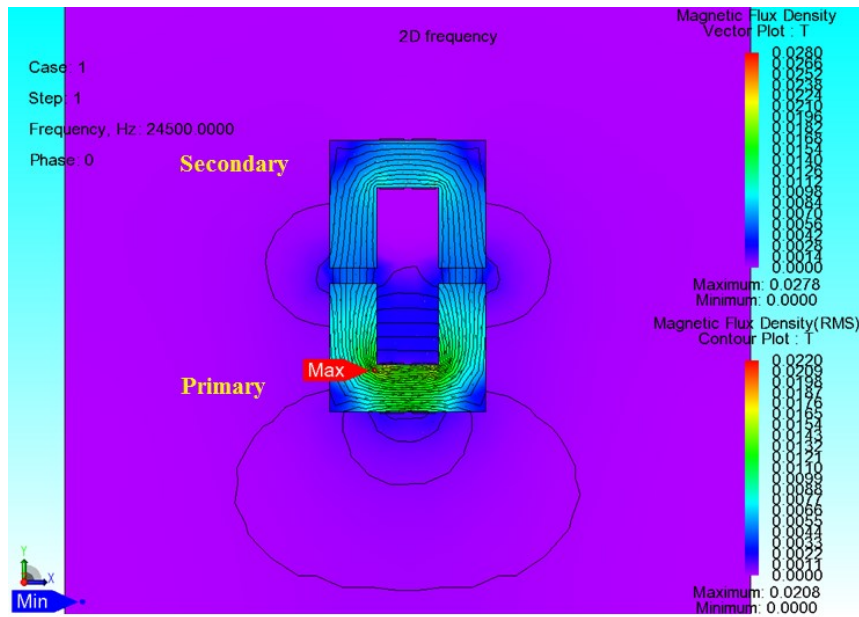


Fig. 3.51 FEA results for the U-U WIPT system with parallel primary and series secondary split windings on U core

(2.a) Experimental verification in WRIPT scenario

The self-inductance of the primary and secondary listed in Table-3.11 are measured without the secondary or primary core influence with LCR meter. All the horizontal misalignments are evaluated at a fixed 1 cm vertical separation.

Table-3.11 U-U core system specifications with split parallel and series windings

Parameter	Specification
Primary Self-Inductance	48 μ H
Primary Resistance (DC)	48 m Ω
Secondary Self-Inductance	47 μ H
Secondary Resistance (DC)	95 m Ω
Primary Compensation Capacitance	0.33 μ F
Secondary Compensation Capacitance	0.33 μ F
Operating Frequency	41.5 kHz
Load Power	10 W
Primary no. of turns	12+13
Secondary turns	6+5

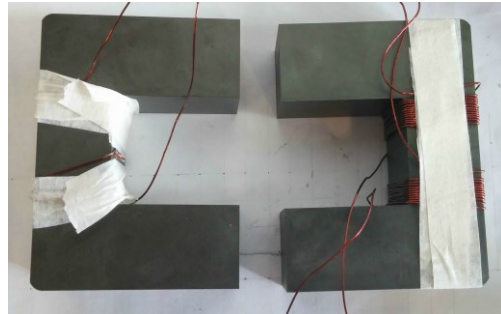


Fig. 3.52 U-U experimental core with split parallel and series windings

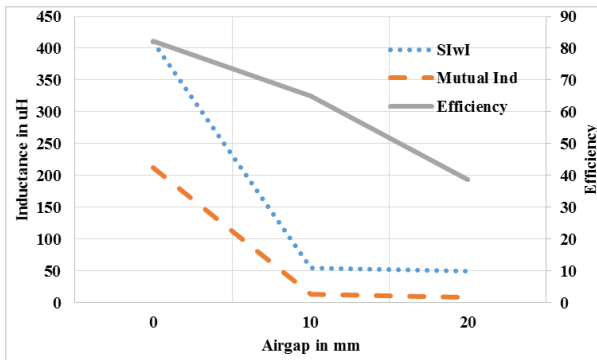


Fig. 3.53 Experimental results plot for vertical separation

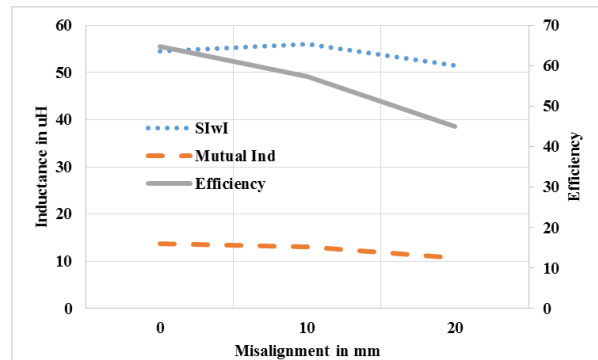


Fig. 3.54 Experimental results for horizontal misalignment at 1 cm vertical separation

(3) U-I core with multiple windings in series on U core central limb

U-I core combination consists of primary U-core with split winding wound horizontally on central limb, connected in series and horizontal winding wound on I-core as shown in the Fig. 3.46 (c) is considered for the FEA and experimental verifications.

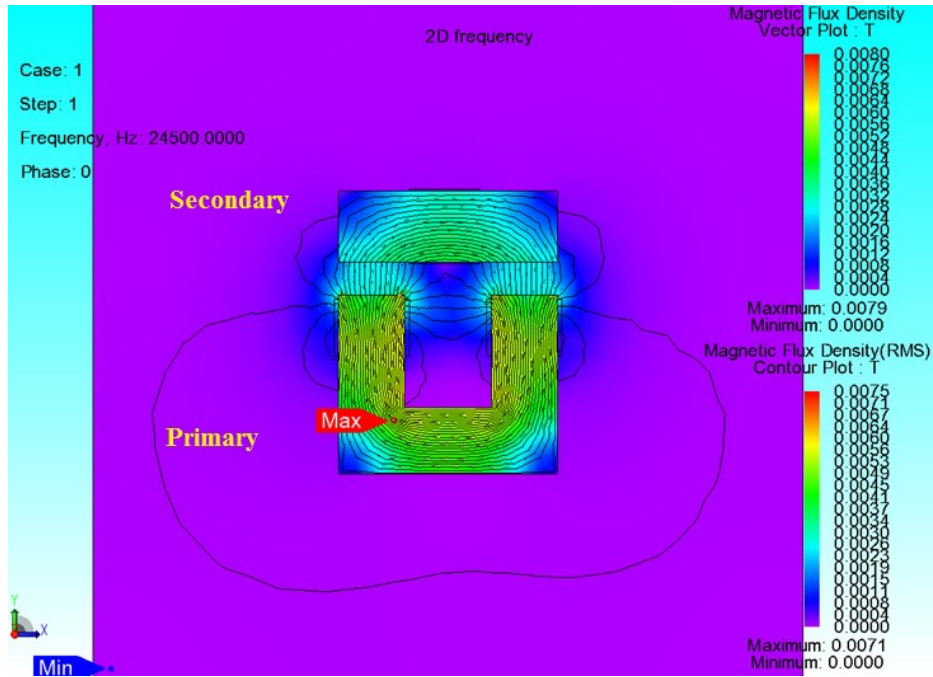


Fig. 3.55 FEA results for the U-I WIPT system with split winding on U core connected in series

(3.a) Experimental verification in WRIPT scenario

The self-inductance of the primary and secondary listed in Table-3.12 are measured without the secondary or primary core influence with LCR meter. All the horizontal misalignments are evaluated at a fixed 1 cm vertical separation.

Table-3.12 U-I core system specifications with split winding on U-core connected in series

Parameter	Specification
Primary Self-Inductance	48 μ H
Primary Resistance (DC)	93 m Ω
Secondary Self-Inductance	47 μ H
Secondary Resistance (DC)	96 m Ω
Primary Compensation Capacitance	0.33 μ F
Secondary Compensation Capacitance	0.33 μ F
Operating Frequency	41.5 kHz
Load Power	10 W
Primary no. of turns	5+6
Secondary turns	14

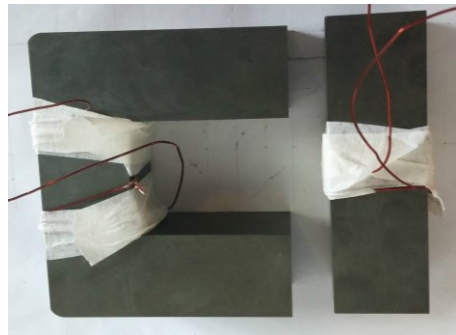


Fig. 3.56 U-I experimental core with series split winding on U-core central limb

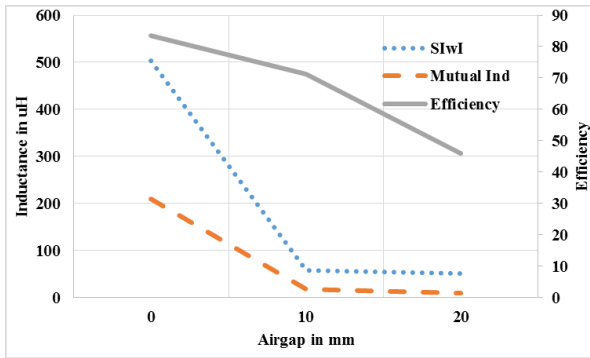


Fig. 3.57 Experimental results plot for vertical separation

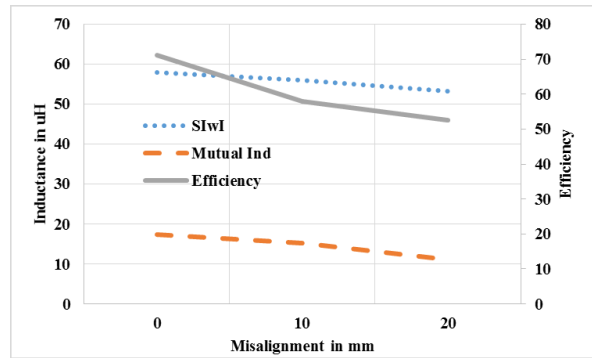


Fig. 3.58 Experimental results for horizontal misalignment at 1 cm vertical separation

(4) U-U core with multiple windings in parallel connected on both cores on central limb

U-U core combination consists of primary U-core with split winding wound horizontally on central limb, connected in parallel on both primary and secondary as shown in the Fig. 3.46(d) is considered for the FEA and experimental verifications.

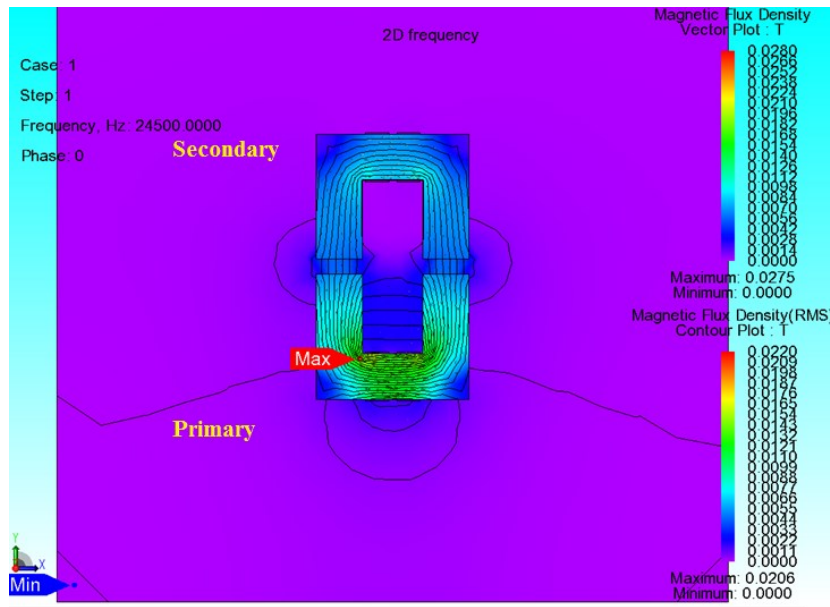


Fig. 3.59 FEA results for the U-U WIPT system with parallel primary and secondary split windings on U core

(4.a) Experimental verification in WRIPT scenario

The self-inductance of the primary and secondary listed in Table-3.13 are measured without the secondary or primary core influence with LCR meter. All the horizontal misalignments are evaluated at a fixed 1 cm vertical separation.

Table-3.13 U-U core system specifications with split parallel windings

Parameter	Specification
Primary Self-Inductance	48 μ H
Primary Resistance (DC)	48 m Ω
Secondary Self-Inductance	47 μ H
Secondary Resistance (DC)	48 m Ω
Primary Compensation Capacitance	0.33 μ F
Secondary Compensation Capacitance	0.33 μ F
Operating Frequency	41.5 kHz
Load Power	10 W
Primary no. of turns	12+13
Secondary turns	12+13

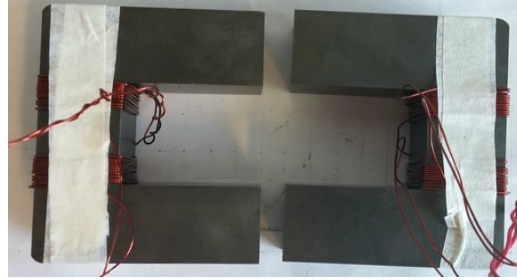


Fig. 3.60 U-U experimental core with split parallel windings

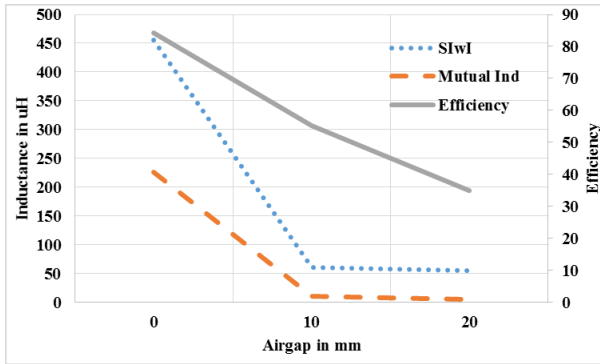


Fig. 3.61 Experimental results plot for vertical separation

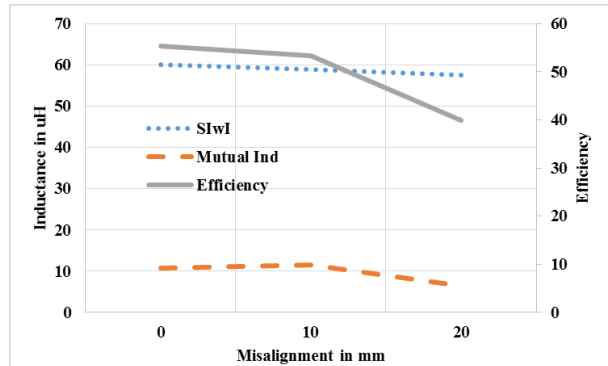


Fig. 3.62 Experimental results for horizontal misalignment at 1 cm vertical separation

(5) U-U core with multiple windings in series connected on both cores on central limb

U-U core combination consists of primary U-core with split winding wound horizontally on central limb, connected in series on both primary and secondary as shown in the Fig. 3.46 (e) is considered for the FEA and experimental verifications.

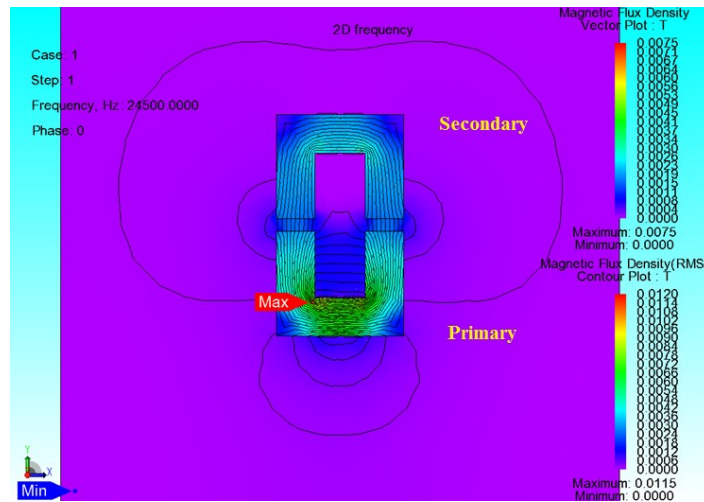


Fig. 3.63 FEA results for the U-U WIPT system with series primary and secondary split windings on U core

(5.a) Experimental verification in WRIPT scenario

The self-inductance of the primary and secondary listed in Table-3.14 are measured without the secondary or primary core influence with LCR meter. All the horizontal misalignments are evaluated at a fixed 1 cm vertical separation.

Table-3.14 U-U core system specifications with split series windings

Parameter	Specification
Primary Self-Inductance	48 μ H
Primary Resistance (DC)	96 $m\Omega$
Secondary Self-Inductance	47 μ H
Secondary Resistance (DC)	97 $m\Omega$
Primary Compensation Capacitance	0.33 μ F
Secondary Compensation Capacitance	0.33 μ F
Operating Frequency	41.5 kHz
Load Power	10 W
Primary no. of turns	5+6
Secondary turns	5+6

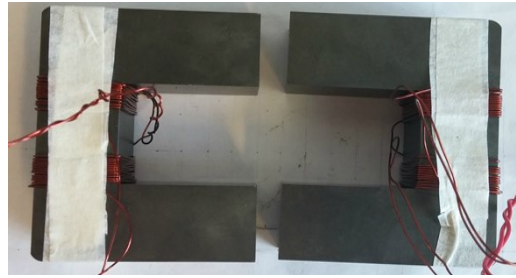


Fig. 3.64 U-U experimental core with split series windings

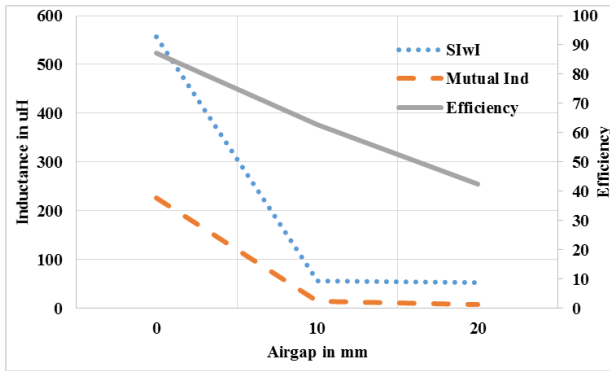


Fig. 3.65 Experimental results plot for vertical separation

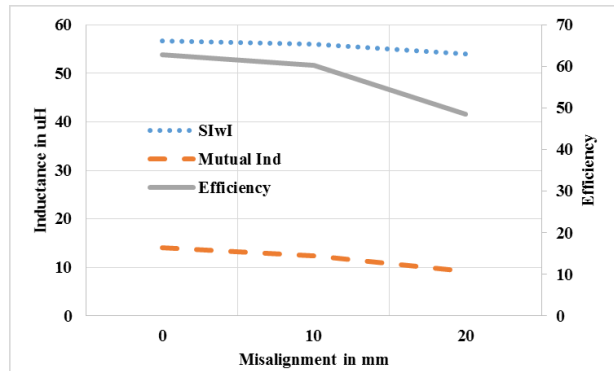


Fig. 3.66 Experimental results for horizontal misalignment at 1 cm vertical separation

(6) U-U core with multiple windings in series connected on both cores on side limb

U-U core combination consists of primary U-core with split winding wound horizontally on side limbs, connected in series on both primary and secondary as shown in the Fig. 3.46 (f) is considered for the FEA and experimental verifications as shown below.

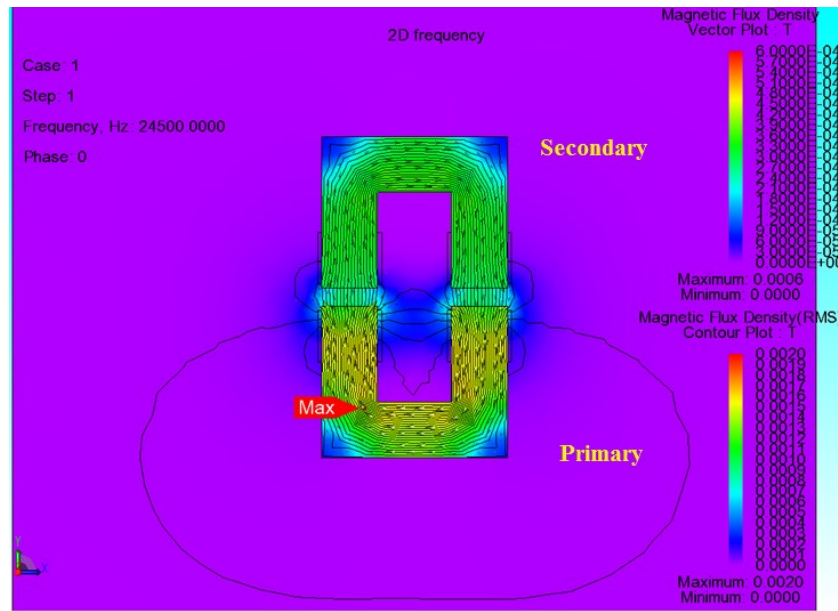


Fig. 3.67 FEA results for the U-U WIPT system with series primary and secondary split windings on U core

(6.a) Experimental verification in WRIPT scenario

The self-inductance of the primary and secondary listed in Table-3.15 are measured without the secondary or primary core influence with LCR meter. All the horizontal misalignments are evaluated at a fixed 1 cm vertical separation.

Table-3.15 U-U core system specifications with split series windings on side limbs

Parameter	Specification
Primary Self-Inductance	48 μ H
Primary Resistance (DC)	186 m Ω
Secondary Self-Inductance	47 μ H
Secondary Resistance (DC)	180 m Ω
Primary Compensation Capacitance	0.33 μ F
Secondary Compensation Capacitance	0.33 μ F
Operating Frequency	41.5 kHz
Load Power	10 W
Primary no. of turns	11+11
Secondary turns	11+11



Fig. 3.68 U-U experimental core with split series windings on side limbs

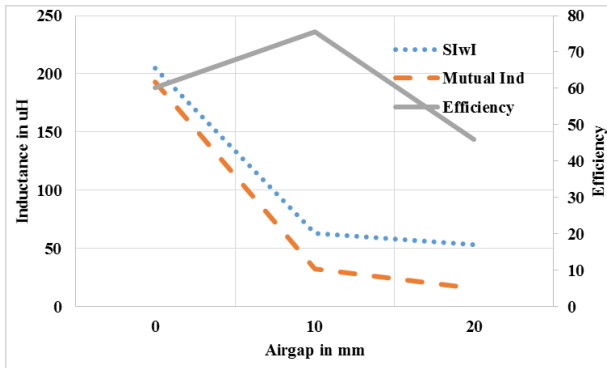


Fig. 3.69 Experimental results plot for vertical separation

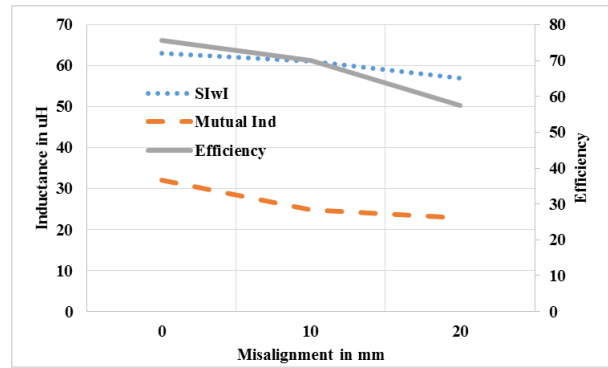


Fig. 3.70 Experimental results for horizontal misalignment at 1 cm vertical separation

(7) U-I core with multiple windings in series on U core side limbs

U-I core combination consists of primary U-core with split winding wound horizontally on side limbs, connected in series and horizontal winding wound on I-core as shown in the Fig. 3.46 (g) is considered for the FEA and experimental verifications.

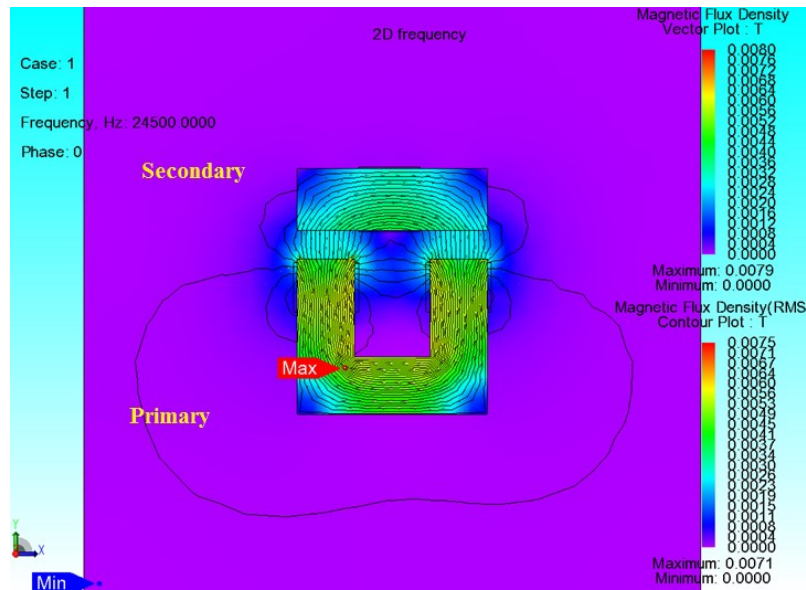


Fig 3.71 FEA results for the U-I WIPT system with split winding on U core connected in series

(7.a) Experimental verification in WRIPT scenario

The self-inductance of the primary and secondary listed in Table-3.16 are measured without the secondary or primary core influence with LCR meter. All the horizontal misalignments are evaluated at a fixed 1 cm vertical separation.

Table-3.16 U-I core system specifications with split winding on U-core connected in series

Parameter	Specification
Primary Self-Inductance	48 μ H
Primary Resistance (DC)	186 m Ω
Secondary Self-Inductance	47 μ H
Secondary Resistance (DC)	93 m Ω
Primary Compensation Capacitance	0.33 μ F
Secondary Compensation Capacitance	0.33 μ F
Operating Frequency	41.5 kHz
Load Power	10 W
Primary no. of turns	11+11
Secondary turns	14



Fig. 3.72 U-I experimental core with series split winding on U-core side limbs

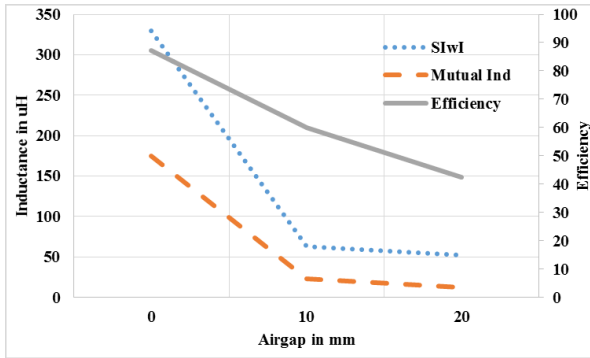


Fig. 3.73 Experimental results plot for vertical separation

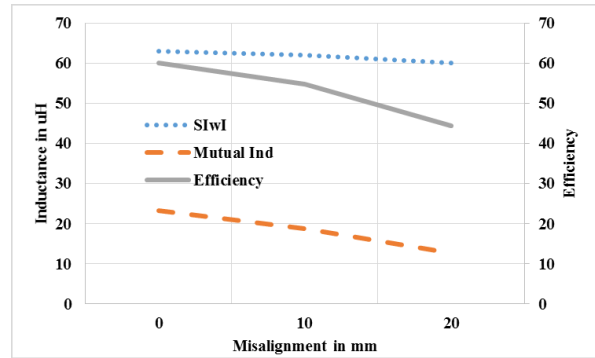


Fig. 3.74 Experimental results for horizontal misalignment at 1 cm vertical separation

(8) U-I core with multiple windings in parallel on U core side limbs

U-I core combination consists of primary U-core with split winding wound horizontally on side limbs, connected in parallel and horizontal winding wound on I-core as shown in the Fig. 3.46 (h) is considered for the FEA and experimental verifications.

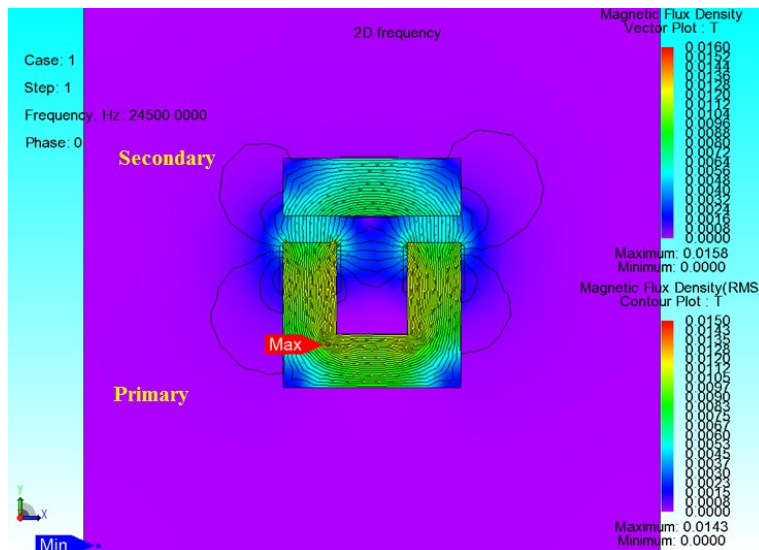


Fig 3.75 FEA results for the U-I WIPT system with split winding on U core connected in parallel

(8.a) Experimental verification in WRIPT scenario

The self-inductance of the primary and secondary listed in Table-3.17 are measured without the secondary or primary core influence with LCR meter. All the horizontal misalignments are evaluated at a fixed 1 cm vertical separation.

Table-3.17 U-I core system specifications with split winding on U-core connected in parallel

Parameter	Specification
Primary Self-Inductance	48 μ H
Primary Resistance (DC)	83 m Ω
Secondary Self-Inductance	47 μ H
Secondary Resistance (DC)	93 m Ω
Primary Compensation Capacitance	0.33 μ F
Secondary Compensation Capacitance	0.33 μ F
Operating Frequency	41.5 kHz
Load Power	10 W
Primary no. of turns	22+21
Secondary turns	14

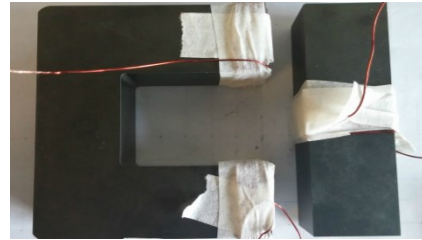


Fig. 3.76 U-I experimental core with parallel split winding on U-core side limbs

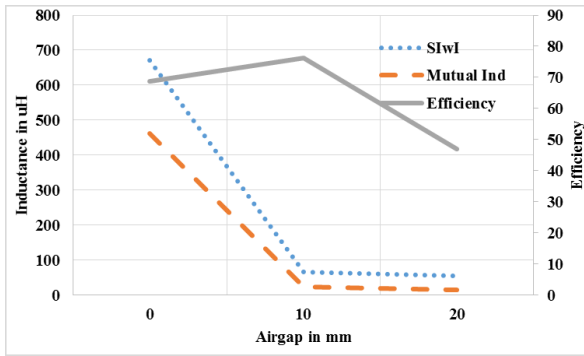


Fig. 3.77 Experimental results plot for vertical separation

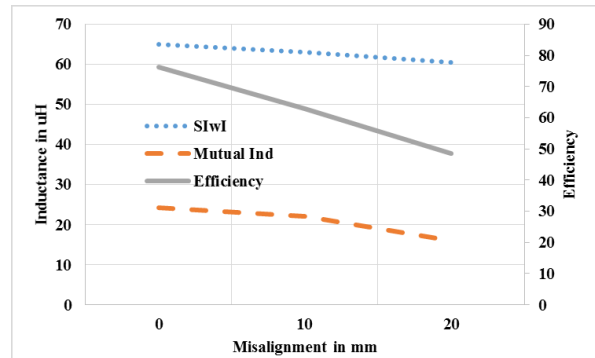


Fig. 3.78 Experimental results for horizontal misalignment at 1 cm vertical separation

(9) U-U core with multiple windings in parallel connected on both cores on side limbs

U-U core combination consists of U-cores with split winding wound horizontally on side limbs, connected in parallel on both primary and secondary as shown in the Fig. 3.46 (j) is considered for the FEA and experimental verifications as shown below.

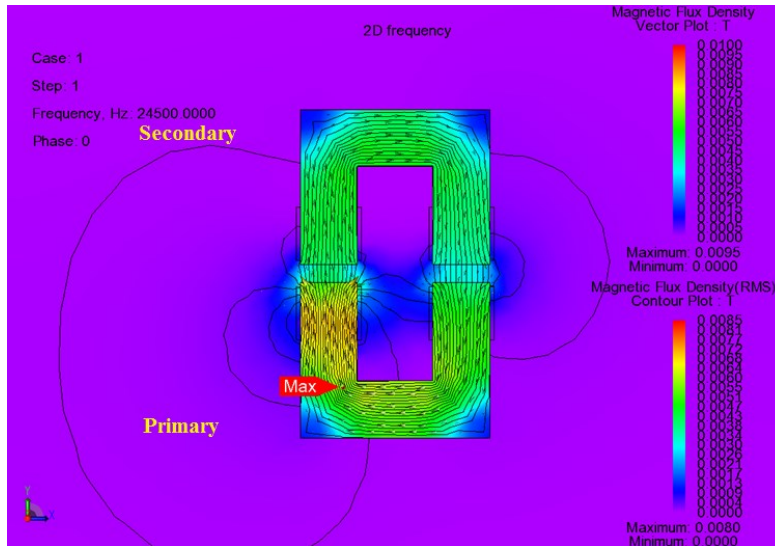


Fig. 3.79 FEA results for the U-U WIPT system with parallel primary and secondary split windings on U core

(9.a) Experimental verification in WRIPT scenario

The self-inductance of the primary and secondary listed in Table-3.17 are measured without the secondary or primary core influence with LCR meter. All the horizontal misalignments are evaluated at a fixed 1 cm vertical separation.

Table-3.17 U-U core system specifications with split series windings on side limbs

Parameter	Specification
Primary Self-Inductance	48 μ H
Primary Resistance (DC)	82 m Ω
Secondary Self-Inductance	47 μ H
Secondary Resistance (DC)	84 m Ω
Primary Compensation Capacitance	0.33 μ F
Secondary Compensation Capacitance	0.33 μ F
Operating Frequency	41.5 kHz
Load Power	10 W
Primary no. of turns	22+21
Secondary turns	22+21



Fig. 3.80 U-U experimental core with split parallel windings on side limbs

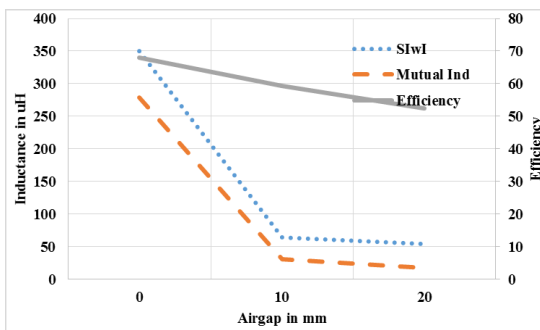


Fig. 3.81 Experimental results plot for vertical separation

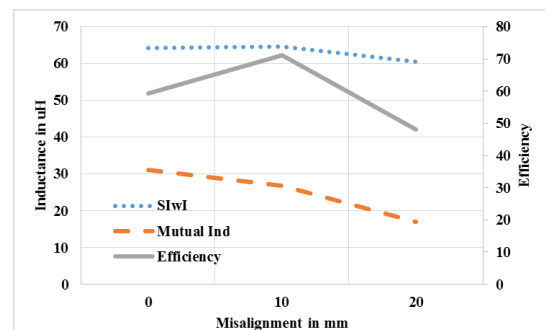


Fig. 3.82 Experimental results for horizontal misalignment at 1 cm vertical separation

(10) U-U core with multiple windings in parallel on primary and series on secondary on side limbs

U-U core combination consists of primary U-core with split winding wound horizontally on side limbs, connected in parallel and split horizontal winding wound in series on secondary U-core as shown in the Fig. 3.46 (i) is considered for the FEA and experimental verifications.

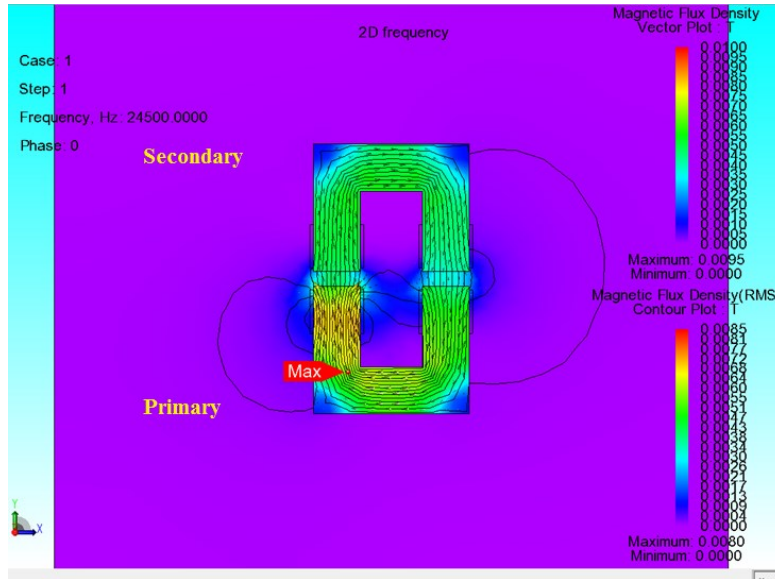


Fig. 3.83 FEA results for the U-U WIPT system with parallel primary and series secondary split windings on U core

(10.a) Experimental verification in WRIPT scenario

The self-inductance of the primary and secondary listed in Table-3.18 are measured without the secondary or primary core influence with LCR meter. All the horizontal misalignments are evaluated at a fixed 1 cm vertical separation.

Table-3.18 U-U core system specifications with split parallel and series windings

Parameter	Specification
Primary Self-Inductance	48 μ H
Primary Resistance (DC)	82 m Ω
Secondary Self-Inductance	47 μ H
Secondary Resistance (DC)	185 m Ω
Primary Compensation Capacitance	0.33 μ F
Secondary Compensation Capacitance	0.33 μ F
Operating Frequency	41.5 kHz
Load Power	10 W
Primary no. of turns	22+21
Secondary turns	11+11



Fig. 3.84 U-U experimental core with split parallel and series windings

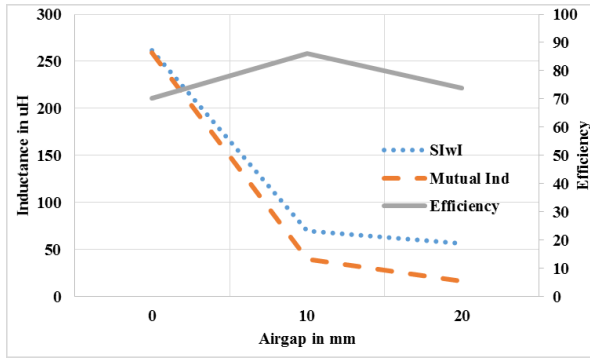


Fig. 3.85 Experimental results plot for vertical separation

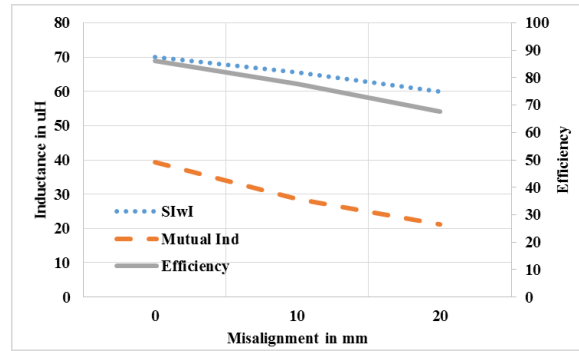


Fig. 3.86 Experimental results for horizontal misalignment at 1 cm vertical separation

The performance of U-U core system with parallel winding on the primary and series winding on secondary placed closer to the airgap gives us the best results so far. As seen from the Fig. 3.85, efficiency at the 1 cm airgap is around 90%. The efficiency under misalignment conditions as seen in Fig. 3.86 is above 70%. Therefore the system exhibits the superior performance over other combinations.

3.3.5 Conclusions and design recommendations for 1.0 KW, 10 cm system

From the FEA analysis and the experimental results obtained for various operating conditions, we can conclude that the U-U core system with split winding is the best design for the final 1.0 kW system. The primary and secondary windings are split into two winding groups connected each on the side limb closer to the airgap of the U-core and they are connected in parallel and series on primary and secondary respectively.

The pole to pole face spacing should be at least 2 times the vertical separation or the airgap. Therefore for a 10 cm system the pole to pole spacing for the U-core design is at least 20 cm.

Chapter-4 1.0 kW prototype design, simulations and Experimental verification

From the analysis in Chapter-3, a prototype is developed for wirelessly transferring power at 10 cm airgap using resonant inductive power transfer to charge an industrial electric vehicle. The required load power is designed to be 1.0 kW. The system block diagram is as shown in Fig. 4.1.

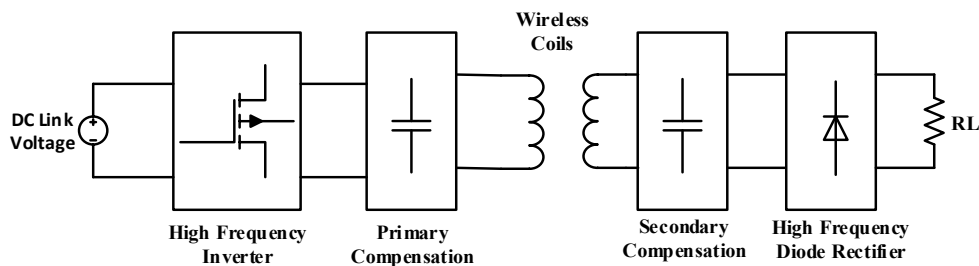


Fig. 4.1 WRIPT block diagram

The main task here is to transfer power from primary to secondary using WRIPT that are separated by 10 cm airgap. Once the secondary induces power, it is rectified and is very simple to cascade a DC/DC converter like buck or boost converter and control the vehicle charging from this stage. Hence, the system is experimentally tested for the input DC to the output DC stage efficiency with a programmable electronic load.

4.1 System design

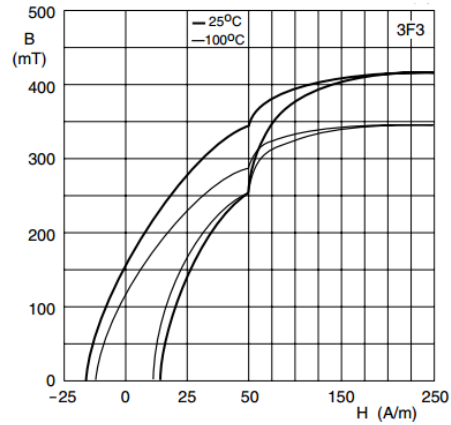
The U-U magnetic core system required for 10 cm airgap should have at least 20 cm side limb separation as per the analysis and recommendation from previous chapter. As the required core geometry cannot be bought off-the-shelf, the cores are constructed as explained below.

4.1.1 Magnetic System Design

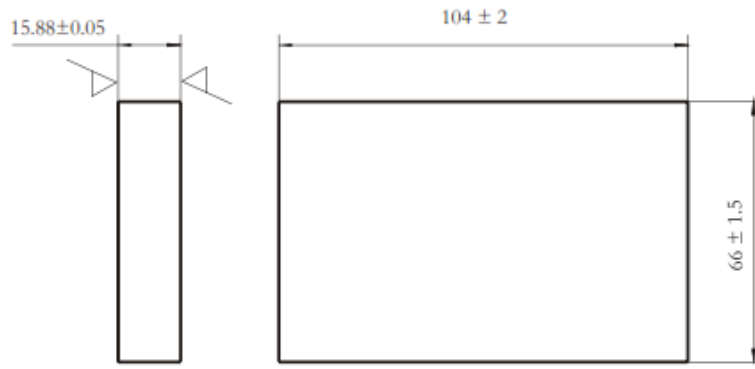
For the WRIPT application, we need a ferrite material that can operate at higher frequencies and material with a very high permeability should be selected. For all these requirements, off-the-shelf available Ferroxcube® 3F3 ferrite material blocks with manufacturer part# BLK104/66/15.9-3F3 are selected to construct the U-core. The material properties [71] are as shown in in Fig. 4.2.

Table-4.1 3F3 Ferrite material Specifications

SYMBOL	CONDITIONS	VALUE	UNIT
μ_i	25 °C; ≤ 10 kHz; 0.25 mT	$2000 \pm 20\%$	
μ_a	100 °C; 25 kHz; 200 mT	≈ 4000	
B	25 °C; 10 kHz; 1200 A/m	≈ 440	mT
	100 °C; 10 kHz; 1200 A/m	≈ 370	
P_v	100 °C; 100 kHz; 100 mT	≤ 80	kW/m ³
	100 °C; 400 kHz; 50 mT	≤ 150	
ρ	DC; 25 °C	≈ 2	Ωm
T_c		≥ 200	°C
density		≈ 4750	kg/m ³



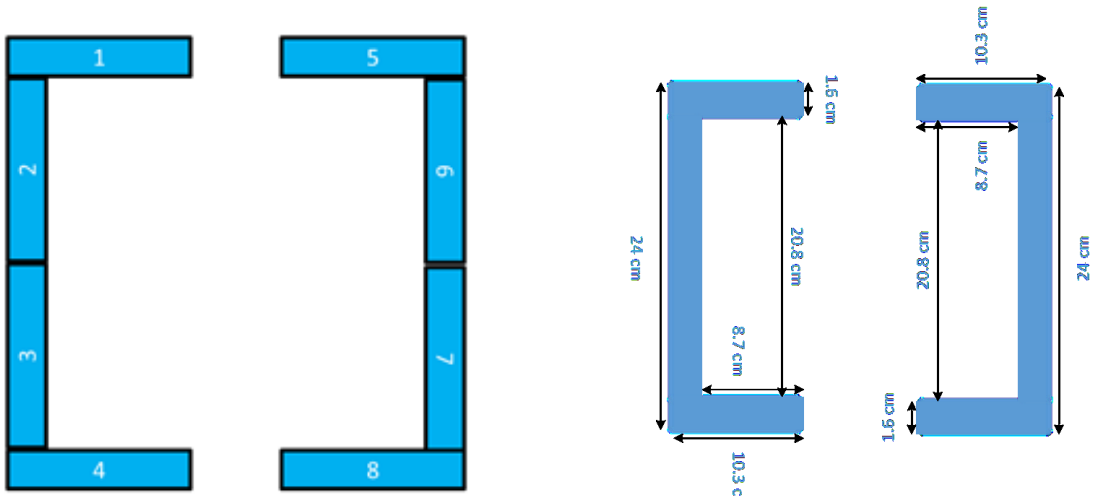
(a) B-H characteristics for 3F3 material



(b) Physical geometry of Fexxrocube 3F3 block BLK104/66/15.9-3F3

Fig. 4.2 Ferroxcube[®] 3F3 ferrite material properties

With the 3F3 block, the best possible U-core geometry is constructed as shown in the below Fig. 4.3.



a) Primary and secondary construction with 4 blocks of ferrite on each

b) Final Ferrite core system geometry

Fig. 4.3. Final U-core system design

As seen, the final geometry formed has a 20.8 cm spacing between the end legs of the ferrite cores.

4.1.2 Final System design specifications

The final system is designed to have the specifications as listed in Table-4.2. 1.0 kW WRIPT system is developed with SP compensation. The main reason for adopting the SP topology is to avoid any voltage stress on the secondary compensation capacitor.

The voltage gain of an SP compensated WRIPT system operating at resonant frequency as derived in 2.3.1 is

$$\left| \frac{V_{out}}{V_{in}} \right| = \frac{1}{k} \cdot \sqrt{\frac{L_S}{L_P}}$$

FEA is carried out on the new design geometry and it is found that the mutual inductance for the system remains almost constant for various primary and secondary self-inductance combinations for a defined airgap. As voltage gain equation is dependent on coupling coefficient and the primary and secondary self-inductances, for a fixed ‘k’ value, we can design different L values for obtaining unity voltage gain. Therefore, two design cases are tried out and experimented to understand the system performance and efficiency.

Case-I: System design with $L_{pri} = L_{sec}$

Case-II System design with $L_{pri} > L_{sec}$ (such that the gain = 1)

These two cases are designed to experiment and evaluate the system for two different voltage gains.

Table-4.2 System design specifications

S.No.	Parameter	Model Name	
		$L_{pri} = L_{sec}$	$L_{pri} > L_{sec}$
1	Primary self-inductance with secondary influence @ 10 cm separation	125 μ H	125 μ H
2	Primary winding dc resistance	30 m Ω	30 m Ω

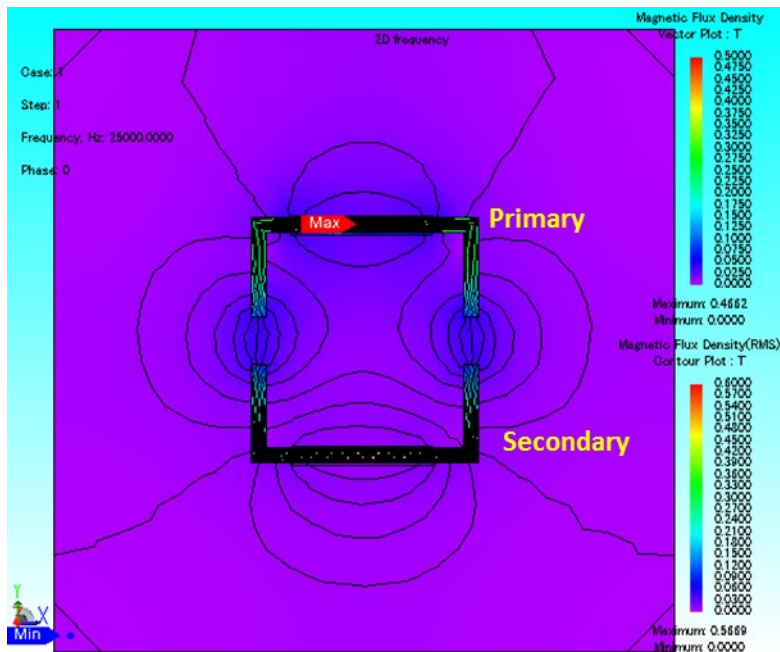
3	Secondary self-inductance with primary influence @ 10 cm separation	125 μ H	21 μ H
4	Secondary winding dc resistance	29 m Ω	14 m Ω
5	Mutual inductance @ 10 cm separation	28.5 μ H	11.5 μ H
6	Input DC Voltage	160 V	275 V
7	Output DC Voltage	360 V	278 V
8	Load Power	1050 W	1050 W
9	Tank Frequency	24.78 kHz	
10	Switching Frequency	24.5 kHz	

The design requirement is to obtain the 400 VDC in the output with a tolerance of $\pm 20\%$. However due to the higher tank currents in the unity voltage gain system, as explained in subsequent sections, the voltage is limited to only around 280 VDC.

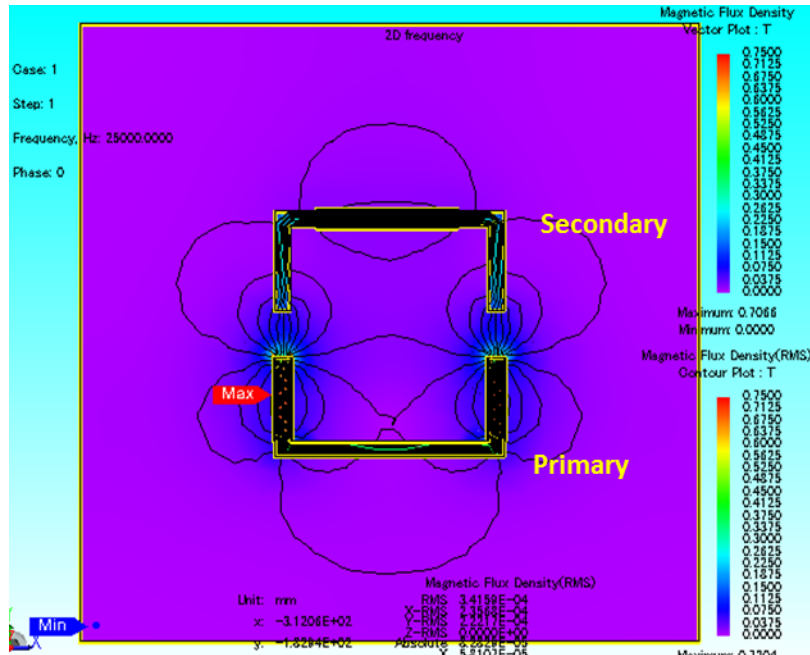
4.1.3 Primary and Secondary inductance design with FEA

To obtain the primary and secondary inductances as per the above table, FEA is done using JAMG to understand the number of turns requirement and design of the magnetic system.

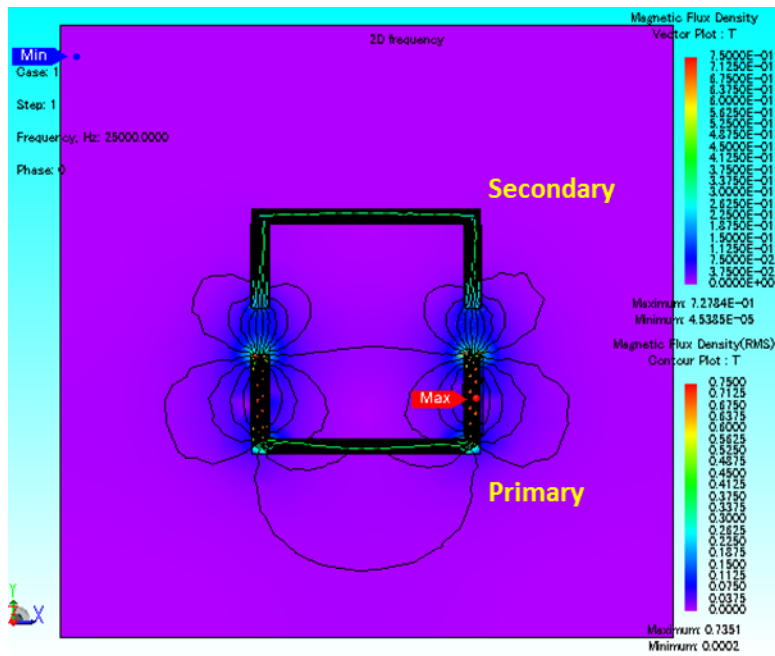
At first, the system leakage flux is studied with a non-split and split windings placed on side limbs, closer to airgap and central limbs on the primary and secondary as shown below.



(a)



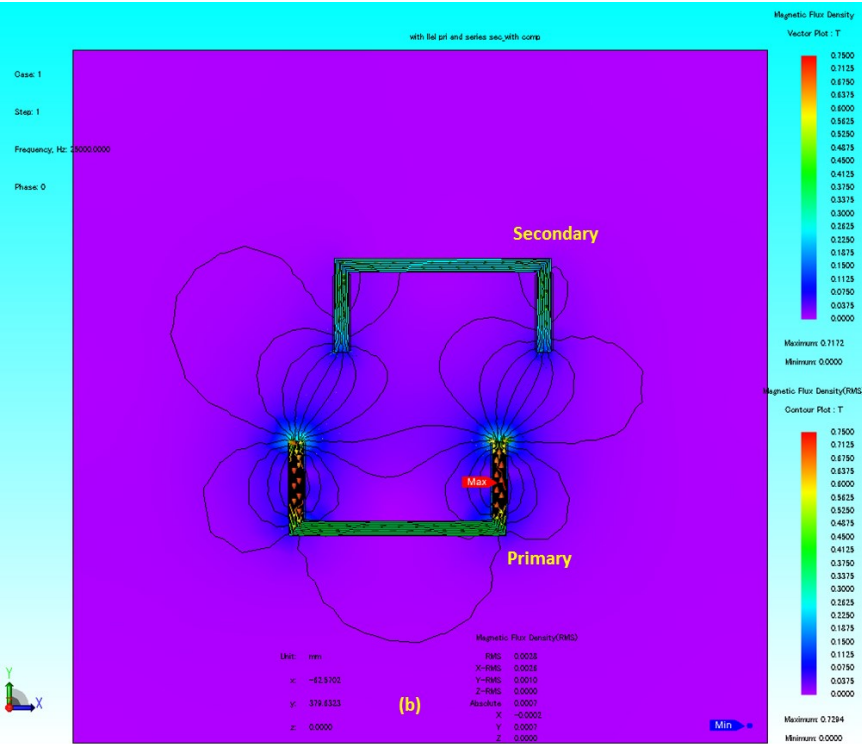
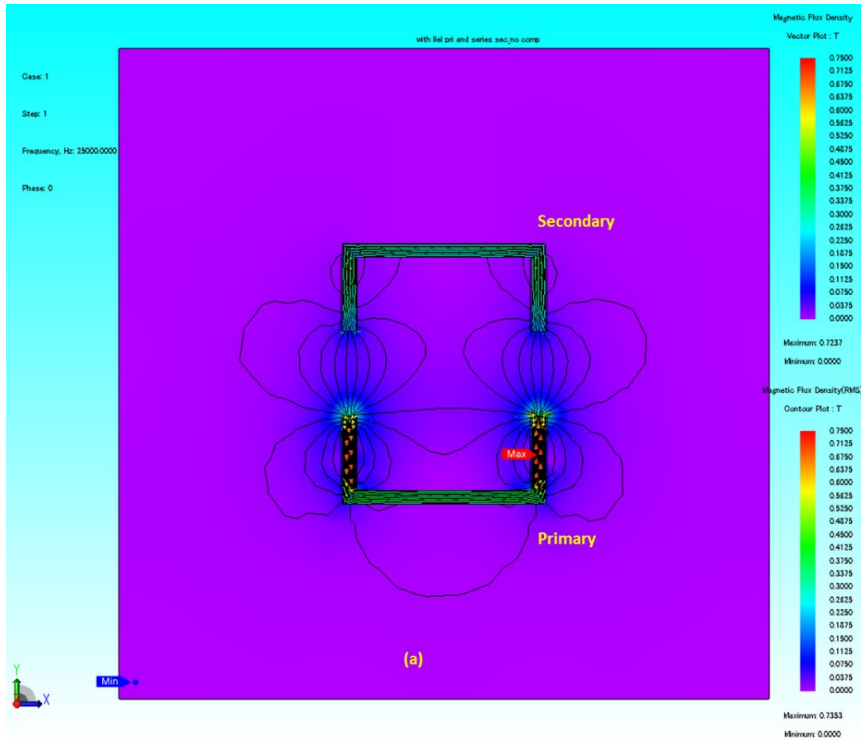
(b)



(c)

Fig. 4.4 WIPT FEA results for U-U core (a) with horizontal winding placed on the central limb of the core (b) with split winding connected in parallel and placed on the side limbs on the primary core and single winding on the secondary central limb (c) With split winding on the primary and secondary core side limbs connected in parallel on primary and series on secondary.

From the FEA analysis, it is seen that the leakage flux is very minimal in the case of the split winding placed on the side limbs closer to the airgap.



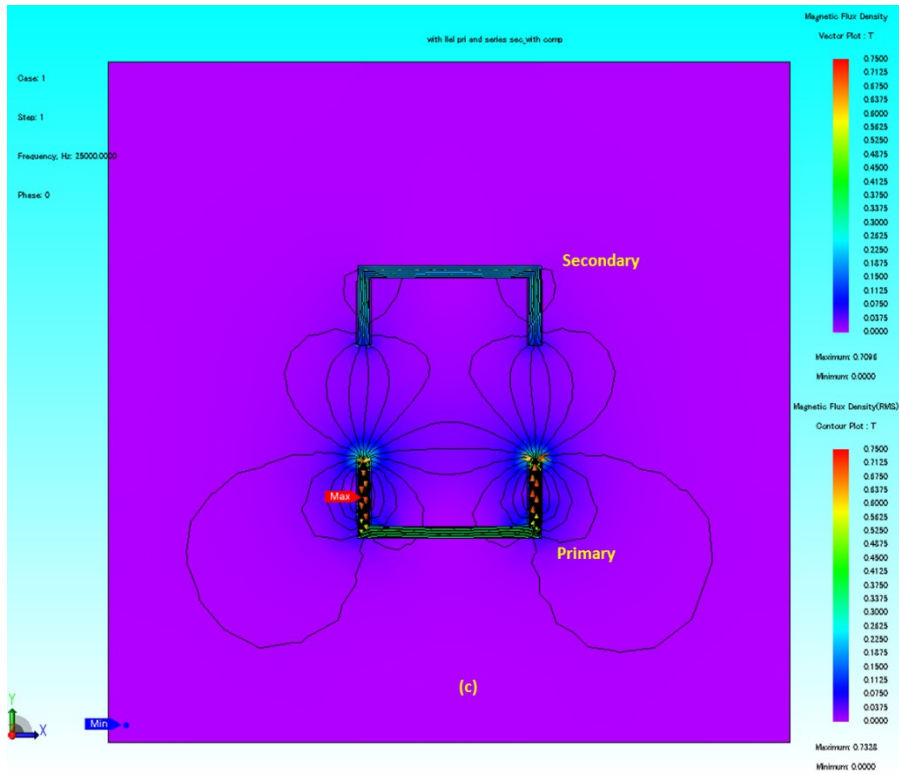


Fig. 4.5 WIPT FEA results for U-U core with split winding connected in parallel on primary and series on secondary
 (a) 10 cm airgap with 0 cm misalignment (b) 10 cm airgap with 5 cm misalignment (c) 15 cm airgap

From the JMAG analysis, the coil design parameters are as listed in Table-4.3.

Table-4.3 Inductance design parameters

Coil Inductance Requirement	Number of Turns
Parallel connected primary inductance of 125 μH	36 Turns/Limb
Series connected secondary inductance of 125 μH	28 Turns/Limb
Series connected secondary inductance of 21 μH	11 Turns/Limb

4.1.4. Litz wire selection and requirements

Litz wire is required to reduce the effects of skin and proximity effects in the conductor for a high frequency operation. We can select the Litz wire each strand diameter based on the frequency of operation. However the total number of strands required depends on the current carrying requirement in the circuit. In order to select the overall effective diameter of the litz wire, we need to calculate the current requirements.

4.1.4.1 Current requirement for $L_{pri} = L_{sec}$

From the specifications in Table-4.2 for $L_{pri} = L_{sec}$ we can theoretically calculate the current requirement in the circuit using the ideal system equivalent circuit shown in Fig. 4.6.

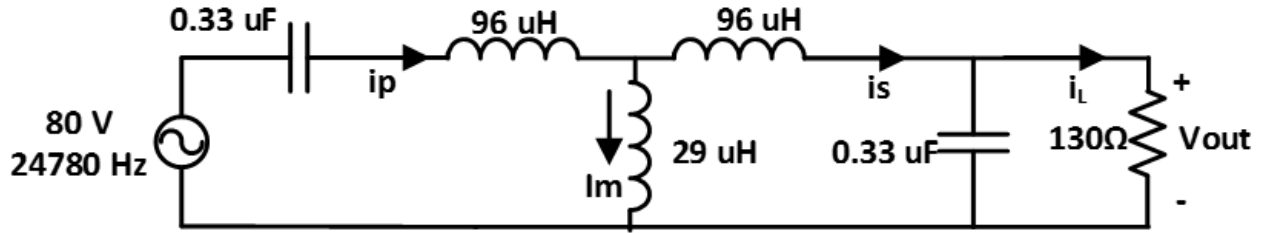


Fig. 4.6 Equivalent circuit model for $L_{pri} = L_{sec}$

Secondary voltage = 360 V

Load power = 1050 W

Load current required = 2.91 A

Current through the capacitor $C_s = 18$ A = Current through the secondary tank and coil.

Therefore the primary tank current is ~ 20 A

Therefore the Litz wire selected should carry a continuous current of at least 22 A with a 10% over design.

For the required ~ 25 kHz operating frequency a 36 AWG wire is selected.

A 90/36 Litz wire**, with 36 AWG and 90 strands is selected that has an approximate continuous current carrying capacity of about 6 A. To carry the required current, 4 wires are connected in parallel and wound on the core.

**We can also select 36 AWG Litz wire with higher number of strands that can carry 22 A current continuously, however due to long supplier lead time, readily available 90/36 wire is selected.

4.1.4.2 Current requirement for $L_{pri} > L_{sec}$

From the specifications in Table-4.2 for $L_{pri} > L_{sec}$ we can theoretically calculate the current requirement in the circuit using the ideal system equivalent circuit shown in Fig. 4.7.

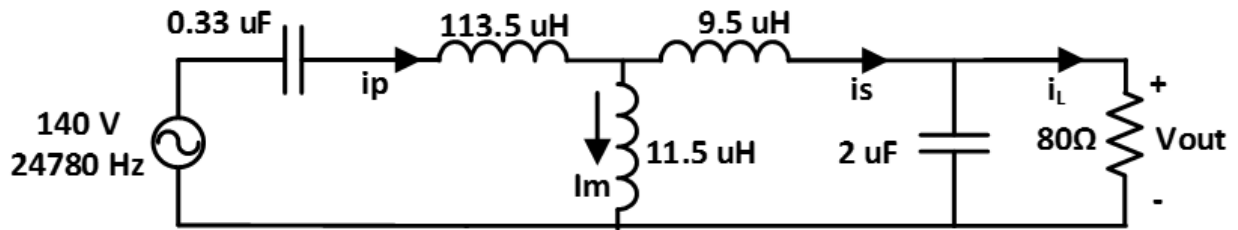


Fig. 4.7 Equivalent circuit model for $L_{pri} = L_{sec}$

Secondary voltage = 280 V

Load power = 1050 W

Load current required = 3.75 A

Current through the capacitor $C_s = 78$ A = Current through the secondary tank and coil.

Therefore the primary tank current is ~ 17 A

Therefore the Litz wire selected should carry a continuous current of at least 85 A on secondary and around 20 A on the primary with a 10% over design.

For the required 25 kHz operating frequency a 36 AWG wire is selected.

A 90/36 SPN Litz wire, with 36 AWG and 90 strands is selected that has an approximate continuous current carrying capacity of about 6 A. To carry the required current, 15 wires are connected in parallel on secondary and 4 wires in parallel on primary and wound on the core.

The final built core with primary and secondary windings is as shown in Fig. 4.8.

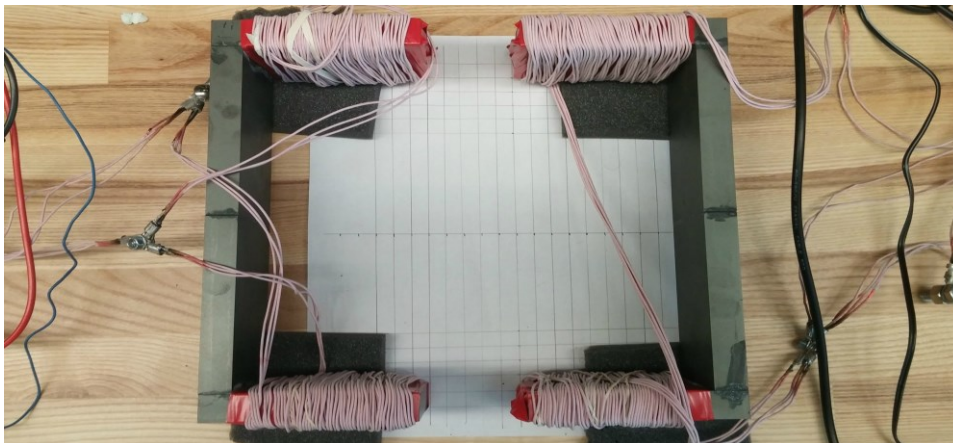


Fig. 4.8 Final build of core with windings

4.1.4. Component selection

The circuit components are selected based on the theoretical calculations, cross verifying with the simulation results. The component list as tabulated in Table-4.4.

Table-4.4 Components used in experimental setup

Component	Supplier	Part#
Inverter IGBT Module	Little Fuse	MG1250S-BA1MM
IGBT driver	Powerex	BG 2C
Compensation Capacitors	0.33 μF	EPCOS (TDK)
	2 μF	EPCOS (TDK)
Secondary Rectifier Diodes	Vishay Semiconductors	VS-20ETF12-M3
Load Filter Capacitor	Vishay Semiconductors	MKP385527125JPI2T0
Micro Controller	Cypress	PSoc 5LP

One of the high frequency IGBT half bridge modules from LittleFuse[®] is selected for the experimental verification. Compensation capacitor rms voltage is calculated theoretically and for high frequency operation, thin film capacitors from Vishay[®] are selected.

4.3 Simulation results for final design system

For the simulation of the final system design, PSIM software package is used. The self-inductance and mutual inductance values obtained from the JMAG FEA analysis for various scenarios are modelled and simulated for 1.0 kW load power.

The simulation circuit for the system is as shown in Fig. 4.9.

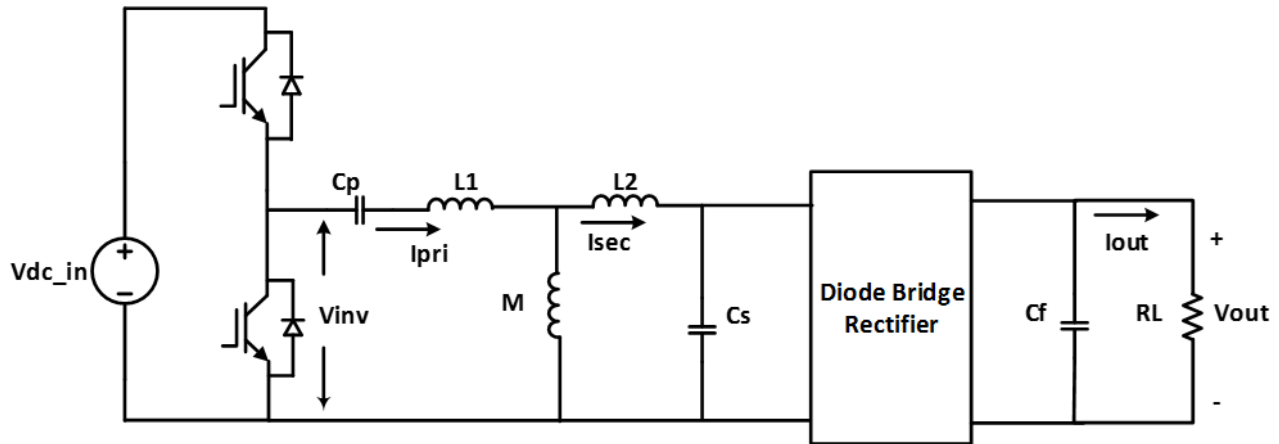


Fig. 4.9 Electrical model and Simulation circuit

Similar to the WRIPT system modelling as explained in section-2.2, the final system is modelled with the obtained self and mutual inductances.

4.3.1 Simulation results for system design with $L_{pri} = L_{sec}$

For 10 cm airgap without misalignment

For the system design with $L_{pri} = L_{sec}$, the self-inductances for both primary and secondary are 125 μH at 10 cm. The mutual inductance is found to be 29 μH .

Therefore the coupling co-efficient is 0.232. And the voltage gain becomes 4.3.

As the voltage gain for Calss-D inverter is almost half, the overall system gain becomes ~ 2.2 .

$$L_1 = L_{pri} - M = 125 \mu\text{H} - 29 \mu\text{H} = 96 \mu\text{H}$$

$$L_2 = L_{sec} - M = 125 \mu\text{H} - 29 \mu\text{H} = 96 \mu\text{H}$$

The compensation capacitor required for the 24.78 kHz tank frequency is 0.33 μF .

Load resistor for the 1.0 kW power at 360 VDC is 130 Ω

For a fixed switching frequency of 24.5 kHz and 50% duty cycle, we can obtain the simulation results as shown in Fig. 4.10.

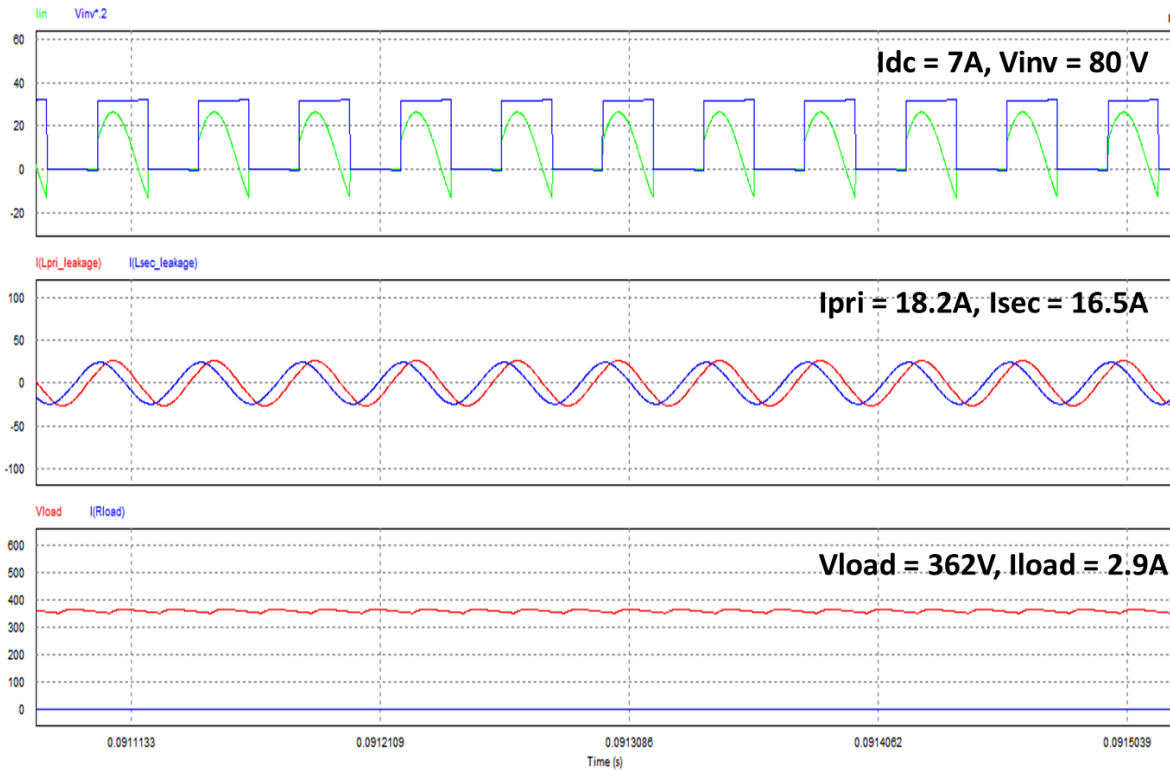


Fig. 4.10 Simulation results for $L_{pri} = L_{sec}$ and @ 10 cm airgap with zero horizontal misalignment

4.3.2 Simulation results for system design with $L_{pri} > L_{sec}$

For 10 cm airgap without misalignment

For the system design with $L_{pri} > L_{sec}$, the self-inductances for primary and secondary are 125 μH and 21 μH respectively at 10 cm. The mutual inductance is found to be 11.5 μH .

Therefore the coupling co-efficient is 0.2245. And the voltage gain becomes ~ 1.9 .

As the voltage gain for Calss-D inverter is almost half, the overall system gain becomes ~ 1 .

$$L_1 = L_{pri} - M = 125 \mu\text{H} - 11.5 \mu\text{H} = 113.5 \mu\text{H}$$

$$L_2 = L_{sec} - M = 21 \mu\text{H} - 11.5 \mu\text{H} = 9.5 \mu\text{H}$$

The compensation capacitor required for the 24.78 kHz tank frequency is 0.33 μF for primary and 2 μF for secondary.

Load resistor for the 1.0 kW power at 280 VDC is 78.5 Ω

For a fixed switching frequency of 24.5 kHz and 50% duty cycle, we can obtain the simulation results as shown in Fig. 4.11.

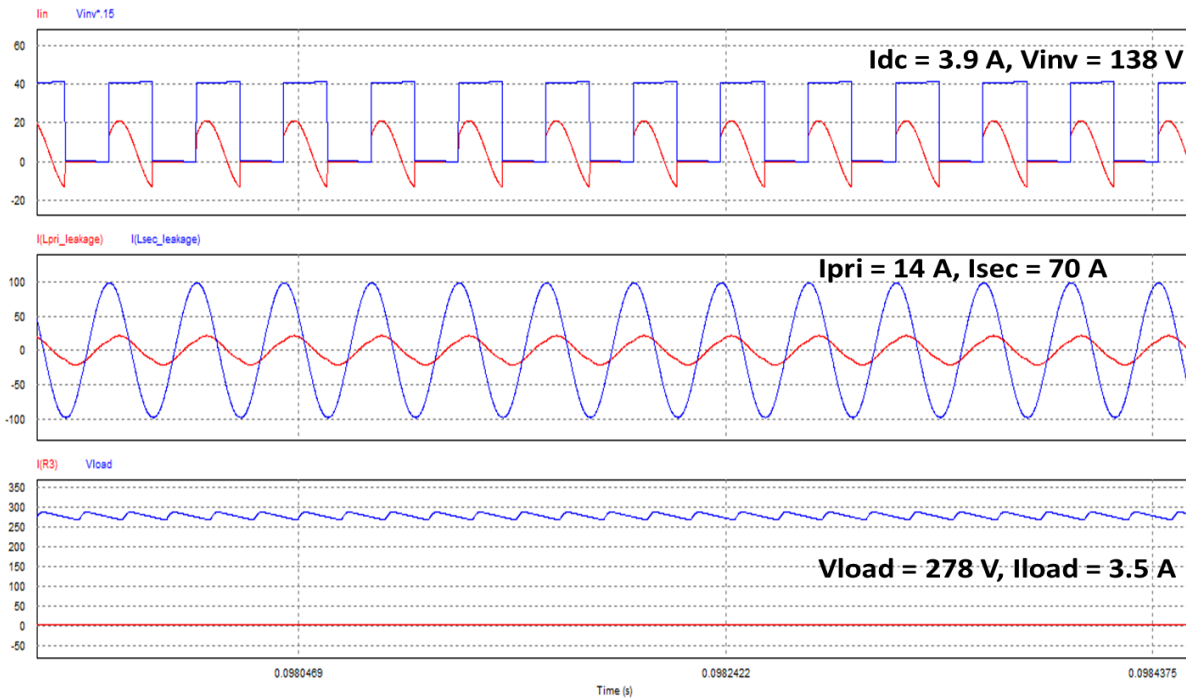


Fig. 4.11 Simulation results for $L_{pri} > L_{sec}$ and @ 10 cm airgap with zero horizontal misalignment

For $L_{pri} > L_{sec}$ and in an SP compensated system, as the secondary capacitor is larger, the secondary tank current is larger than the primary tank.

4.4 Experimental results for final design system

The experimental circuit for the designed WRIPT system is as shown in Fig. 4.12. Various operating conditions are tested for input DC to output DC stage efficiency measurement.

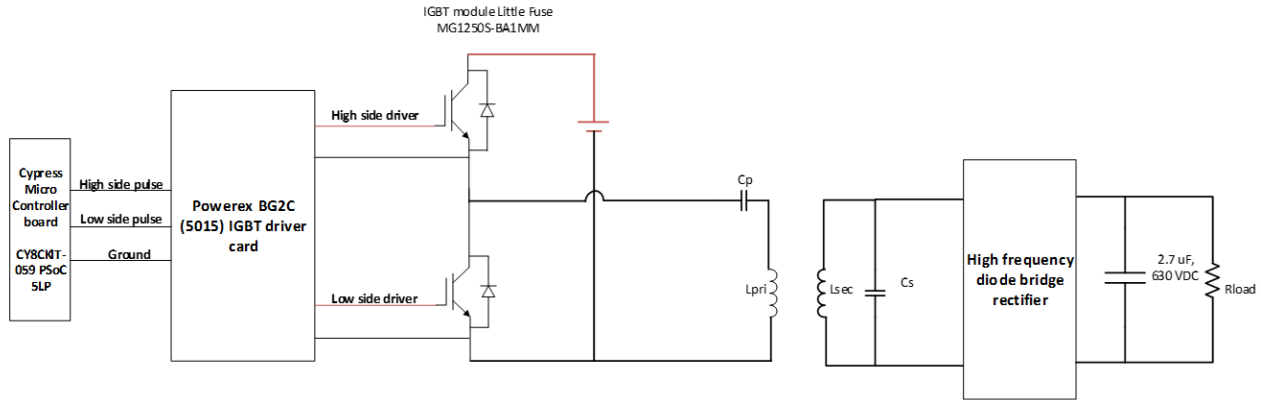


Fig. 4.12. Experimental circuit for WRIPT system

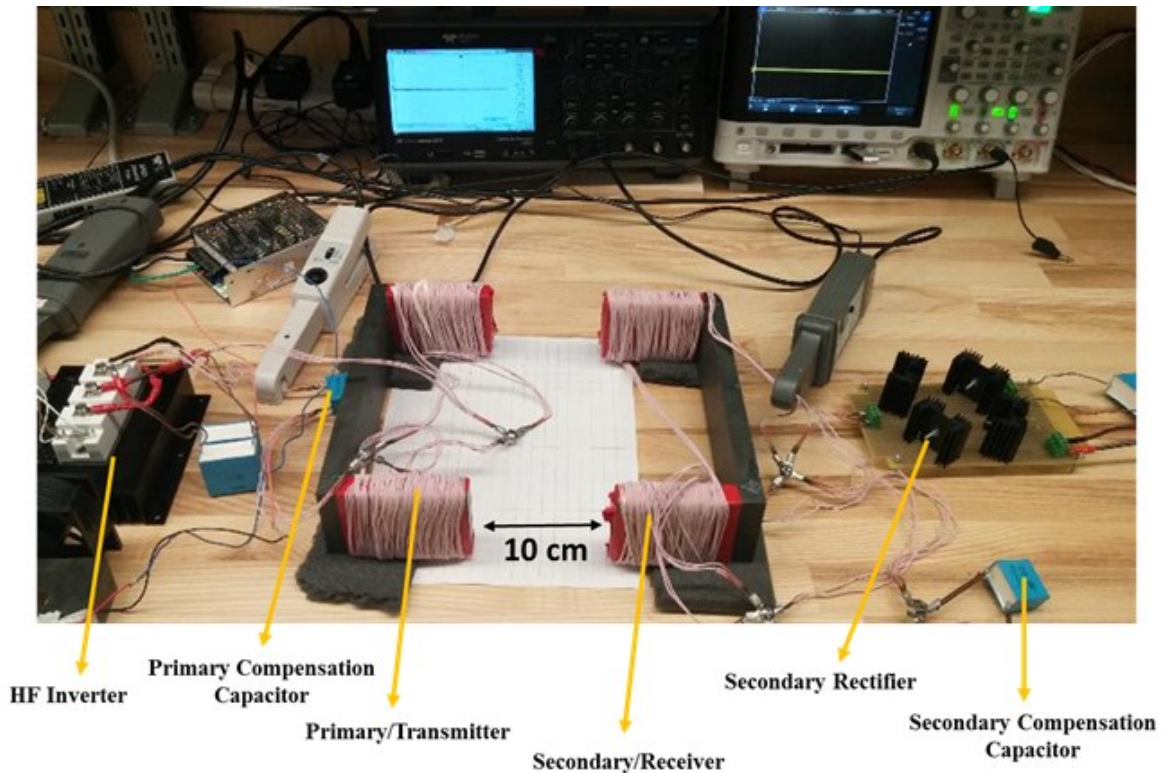


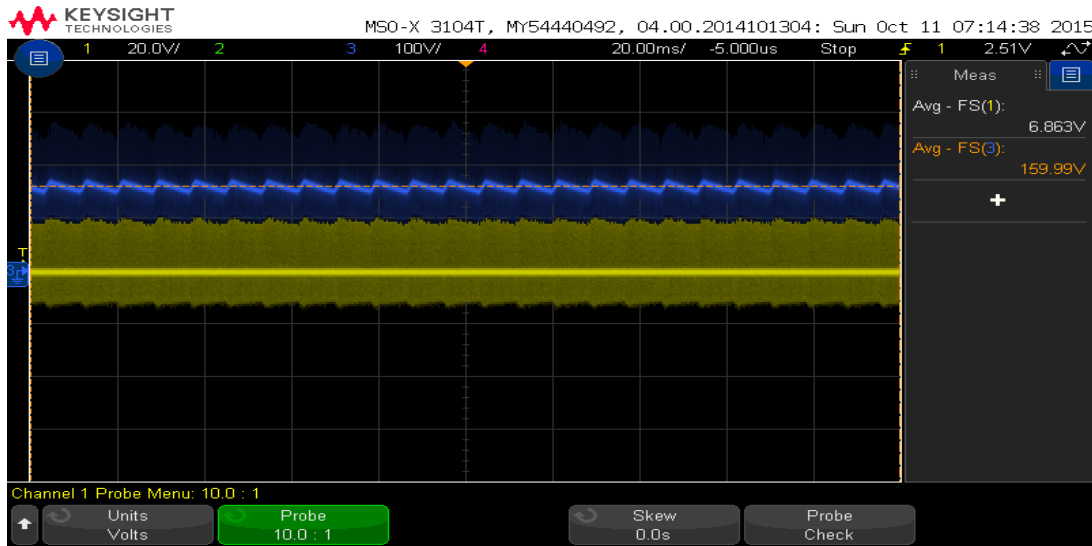
Fig. 4.13. Experimental setup for $L_{pri} = L_{sec}$ and @ 10 cm airgap with zero horizontal misalignment

4.4.1 Experimental results for $L_{pri} = L_{sec}$ system

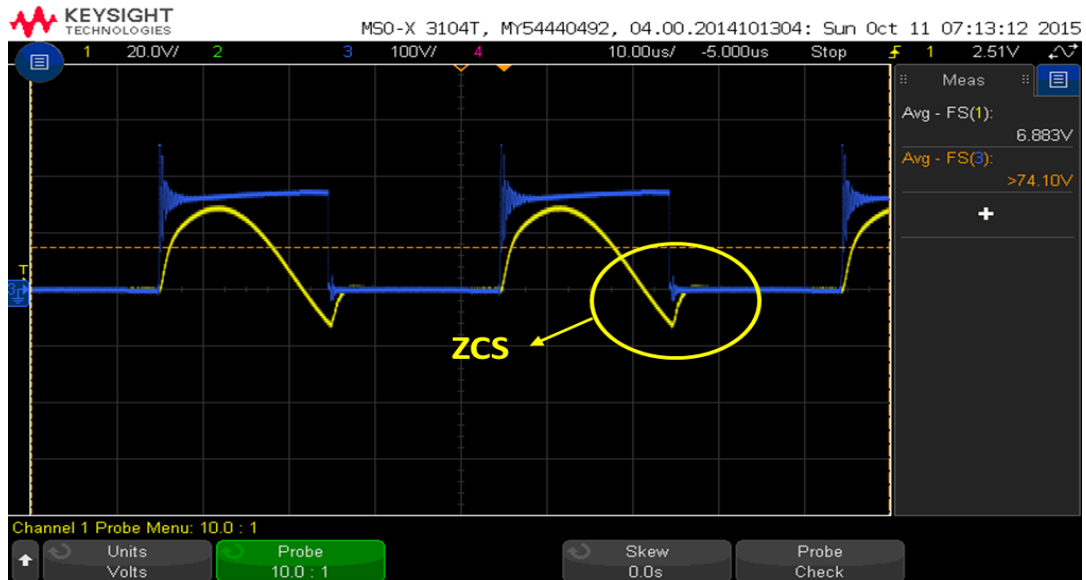
For all the experiments, a dead band of 750 nS is introduced at the rising edge of the PWM pulse and is switched with a 50% duty cycle.

(a) Results for $L_{pri} = L_{sec}$ system @ 10 cm airgap with zero horizontal misalignment

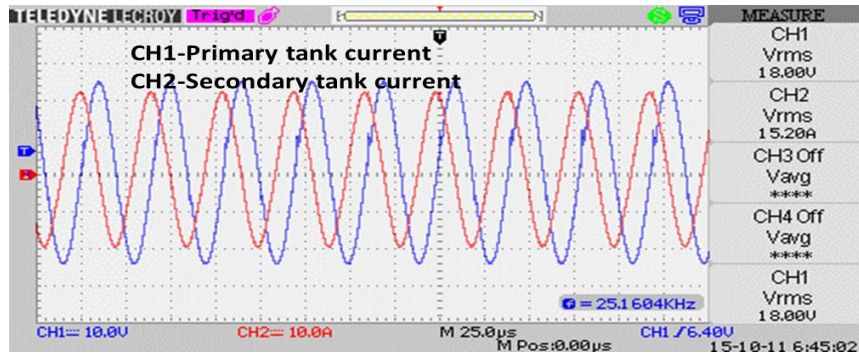
The experimental setup for 10 cm airgap is as shown in Fig. 4.13. Experimental results for the system with $L_{pri} = L_{sec}$ are as shown below.



(a)



(b)



(c)

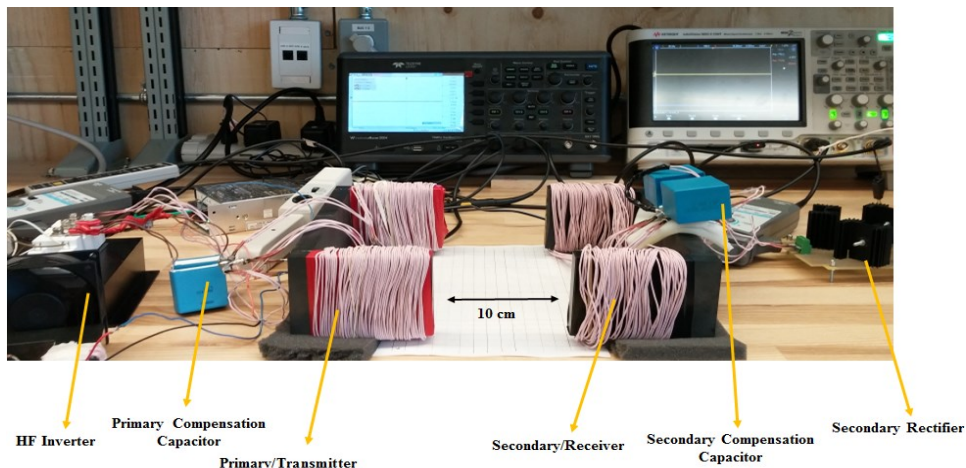


(d)

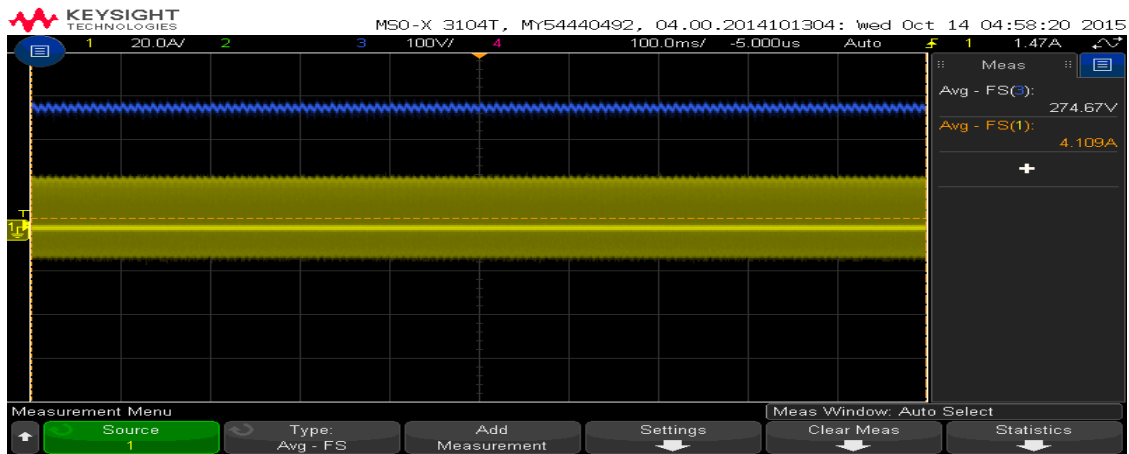
Fig. 4.14 Experimental results for for $L_{pri} = L_{sec}$ and @ 10 cm airgap without zero horizontal misalignment (a) DC link voltage and current (b) Device voltage and current (c) Primary and secondary tank currents (d) Load voltage, current and power

4.4.2 Experimental results for $L_{pri} > L_{sec}$ system

(a) Results for $L_{pri} > L_{sec}$ system @ 10 cm airgap with zero horizontal misalignment are as shown below.



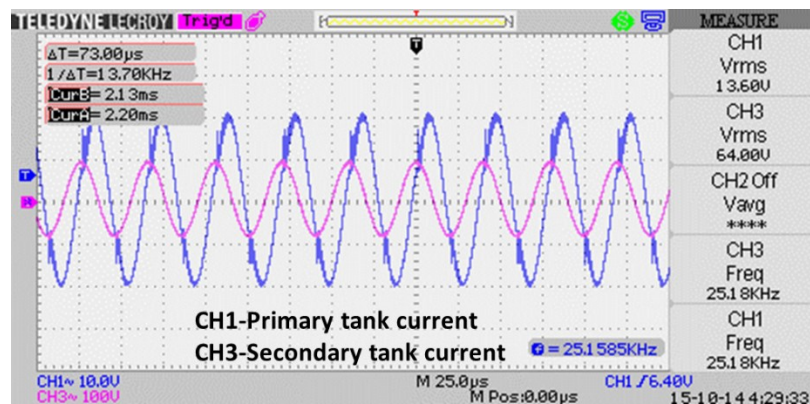
(a)



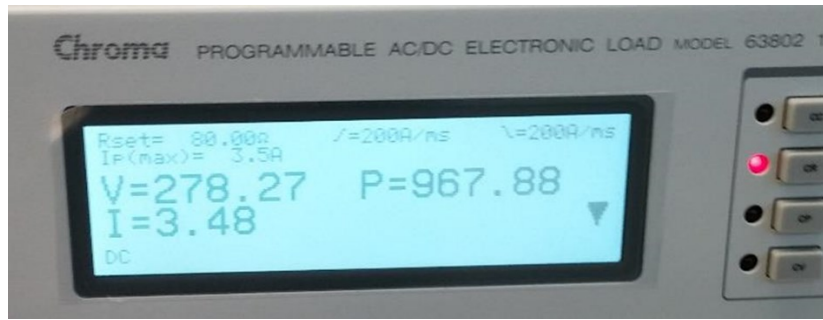
(b)



(c)



(d)

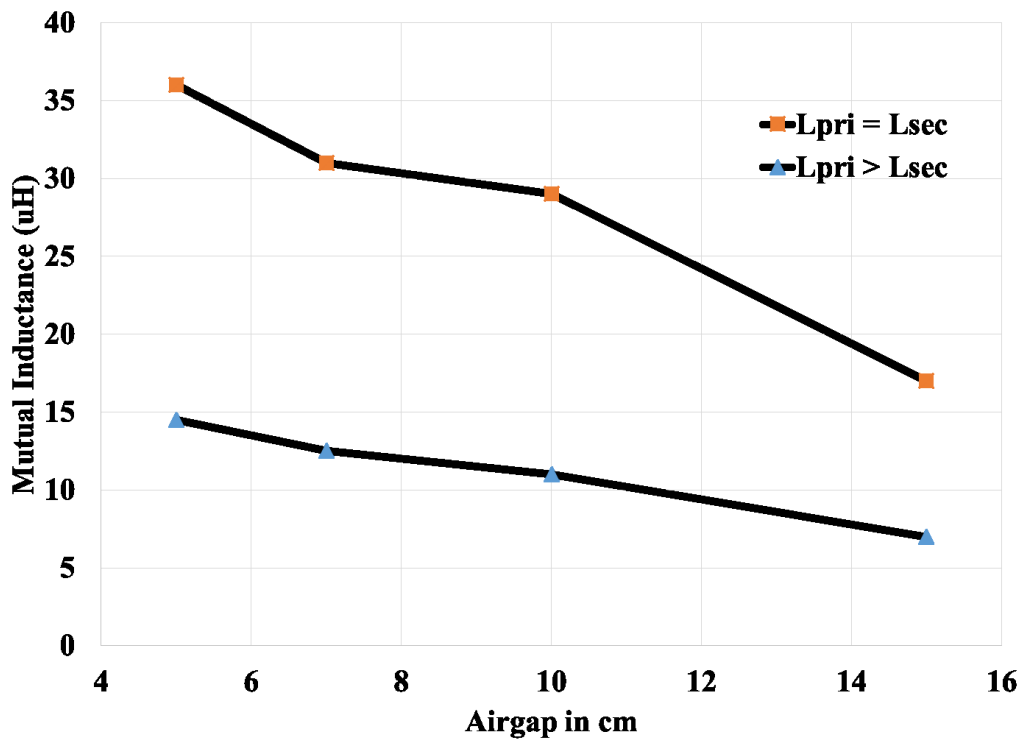


(e)

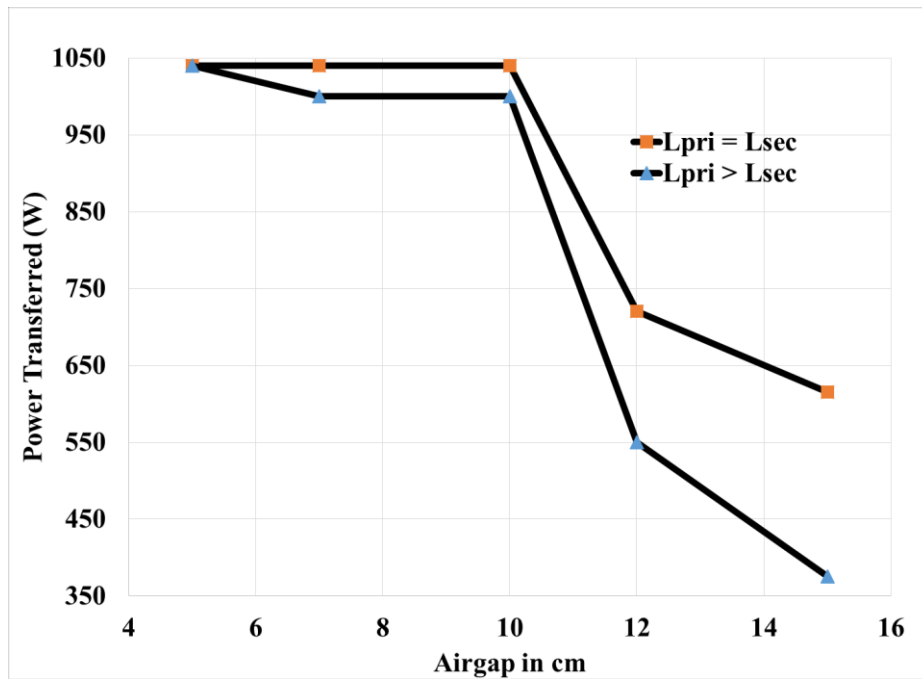
Fig. 4.15 Experimental results for for $L_{pri} > L_{sec}$ and @ 10 cm airgap without zero horizontal misalignment (a) DC link voltage and current (b) Device voltage and current (c) Primary and secondary tank currents (d) Load voltage, current and power

4.5. Experimental Results compilation and comparison

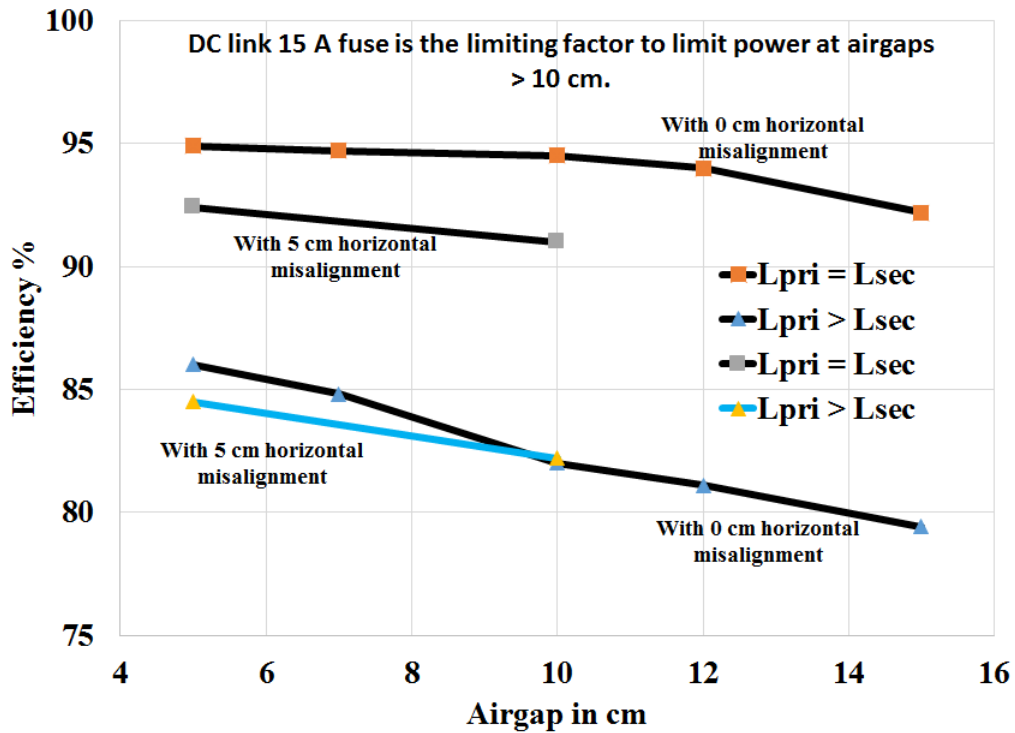
With the obtained experimental results, various graphs are plotted as shown in Fig. 4.16.



(a)



(b)



(c)

Fig. 4.16 (a) Trend of mutual inductance with respect to airgap for both voltage gain systems (b) Power transfer vs airgap plot (c) DC to DC power transfer efficiency with variation in airgap

From the above graphs, we see that the system performance with $L_{pri} > L_{sec}$ is poor compared to the system with $L_{pri} = L_{sec}$. This is due to lower value of self-inductance on the secondary receiver. Due to lower inductance, to resonate at the primary frequency, the capacitor required is large. The larger capacitor connected in parallel on the secondary will circulate larger secondary tank current, which causes larger Ohmic losses, hence the efficiency is poor.

The system is loaded with 1050 W till 10 cm and after that the system would not allow load to reach 1050 W due to the 15 A over load fuse in the DC link.

4.5. Magnetic field radiation

The power transfer in the WRIPT system over large airgap is achieved by a high frequency magnetic field. Due to larger airgaps, in a WRIPT system there exists a large amount of leakage flux. This leakage flux will cause a magnetic radiation surrounding the power transfer coils. High frequency leakage magnetic field links with nearby metal parts and induces eddy currents. This is extremely dangerous for people with pace makers or any such sensitive medical devices. Also it is seen that continuous exposure of human body to the magnetic field causes many health hazards. Therefore it is very vital to design the WRIPT system with low magnetic radiation. In high power WRIPT systems, the system design should also include the shielding design for suppressing the magnetic field radiation.

Safety regulations from International Commission on Non-Ionizing Radiation Protection (ICNIRP) and wireless charging standard SAE J2954 enforces the designers to meet the magnetic radiations.

In this research work, ferrite core based transmitter and receiver are designed that can reduce the magnetic radiation, by providing the very low reluctance path through the core itself. As seen from the FEA analysis, the leakage flux into the transmitter and receiver surroundings is less for the designed final system. For the system with $L_{pri} = L_{sec}$ magnetic radiation is measured using 3D axis Magnetometer. The results are as shown in Fig. 4.18.

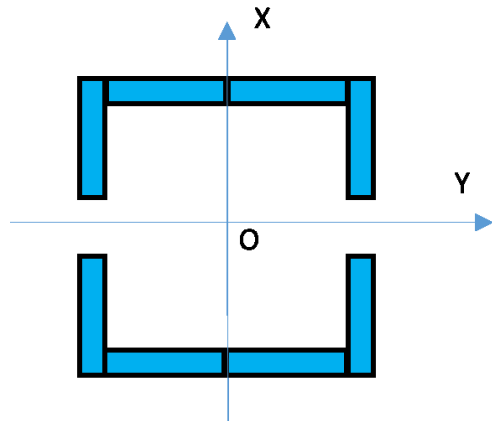


Fig. 4.17 Magnetic radiation measurement axis

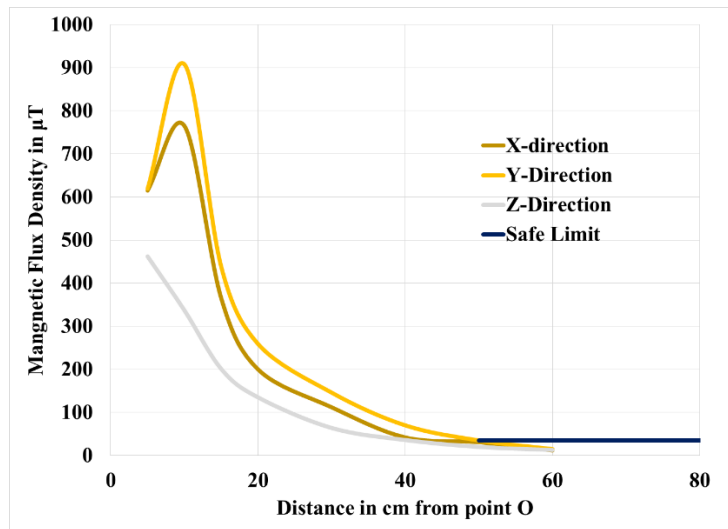


Fig. 4.18 Magnetic flux density in XYZ direction from point O.

The WRIPT regulation SAE J2954 and ICNIRP states that the safe limit for magnetic radiation should not exceed 27 μT after 60 cm from the center of the coils. As seen from the measurement results, the designed system meeting the standard requirement without any extra shielding. With further optimization of the system design we can easily reduce the peak radiation at closer distances.

In this design, there is no extra shielding is designed. We can say that the design inherently has a reduced magnetic radiation.

4.6 System comparison with circular coil design

Most popular circular coil can be compared to the novel U-U core RIPT wireless system. Fig. 4.19, shows top view and side view of the circular and U core systems' primary transmitter. Each limb on the U core forms a pole pair. In the design of U-core WRIPT system, opposite poles on the limbs have no much effect than the poles closer to the airgap. This is due to the fact that they make a magnetic circuit with least reluctance path through the core.

It is seen from the Fig. 4.19, that the circular coil has a pole to pole spacing of $\frac{1}{2}d$, whereas the U-core has a pole to pole spacing of d . While it is in operation, the U-core has less pole to pole leakage flux than the circular coil. For the same size, the U-core offers very high reluctance to the leakage magnetic path between pole to pole as opposed to the circular coil whose reluctance path

for leakage flux is half that of the U-core. This will enable U-core to push useful flux on to secondary and have more effective coupling than circular coils. Hence, for the same size U-core primary can push power to secondary more efficiently than the circular core. The only problem with U-core system design is that when the misalignment between the primary and secondary is 90° , the coupling is almost zero. However in electric vehicle charging applications, it is very unlikely to have misalignment of 90° .

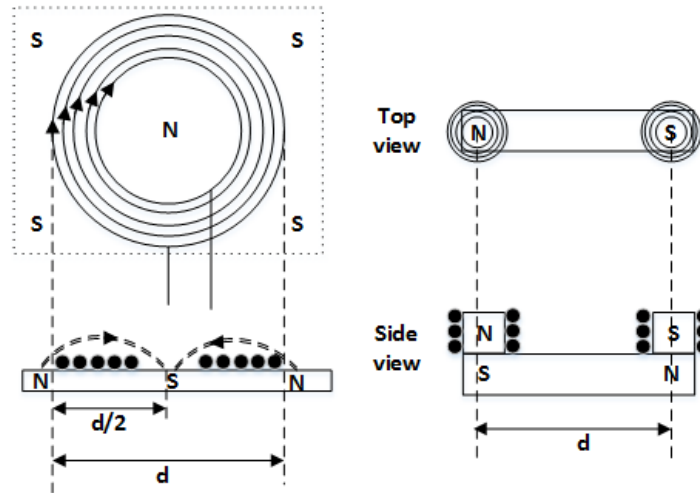


Fig. 4.19 pole to pole spacing in circular coil and U core MPTS

The pole to pole spacing 'd' should be larger than the required vertical separation, so that the magnetic flux finds the least reluctance path through the secondary instead of leaking directly between the primary poles. The system has a very high coupling when 'd' is at least 2 times the vertical separation. When compared, circular coil or pancake geometries would require a significantly larger diameter to achieve similar coupling efficiencies at a given airgap. For example, to design a 15 cm airgap system, U-core primary will have 30 cm pole to pole spacing whereas the pancake coil design requires a diameter of about 40-45 cm on the primary side.

4.7 Conclusion

FEA is carried out on the final U-U core geometry with split winding and at various airgaps and misalignments. Two system were designed with $L_{pri} = L_{sec}$ and $L_{pri} > L_{sec}$. From the experimental results on final design, it is seen that the system with $L_{pri} = L_{sec}$ operates at a the DC to DC efficiency of 94.7% at 10 cm airgap and 91% at 10 cm airgap and 5 cm misalignment.

However for the system with $L_{pri} > L_{sec}$, the performance of the system is very poor. This is due to the below facts;

- a. The mutual inductance is very low due to low secondary inductance.
- b. As secondary capacitance value is larger for maintaining the input tank frequency due to the inductance imbalance condition, the secondary tank current is very large.
- c. As a result of secondary larger current, and low mutual inductance, the primary current is also considerably larger than that we saw in the case of $L_{pri} = L_{sec}$.
- d. As a result of point 'c', the device current is also high.
- e. Above all larger currents are resulting in high Ohmic losses in the system which is the main reason for loss of efficiency.

Magnetic radiation is also measured while conducting experiments using a magnetometer and observed that the magnetic radiation results are well within the safety limits posed by the WRIPT charging standards.

Chapter-5 Control of Class-D Amplifier in a Series-Parallel Compensated WRIPT System for Achieving Unity Voltage Gain

To charge an IEV from a 400 VDC input, it is very important to understand the voltage gain characteristics of the system. As seen from the voltage gain characteristics from section-2.3 of this thesis, when operated at resonance frequency, SP system voltage gain is dependent on coupling co-efficient and primary and secondary self-inductances. However, from the gain plot, we can see that unity gain can be achieved by varying the switching frequency as seen in Fig. 5.1. Alternatively, we can achieve required gain by changing the fundamental component of the inverter output voltage by duty cycle control.

In this work, a class-D amplifier is used to drive the WRIPT system. There are two control techniques to achieve the unity voltage gain viz. variable frequency control and fixed frequency control. In the fixed frequency control, the switching frequency is constant and the duty cycle and amplitude control are done. On the other hand, in the variable frequency control, the switching frequency is varied to achieve the required voltage gain.

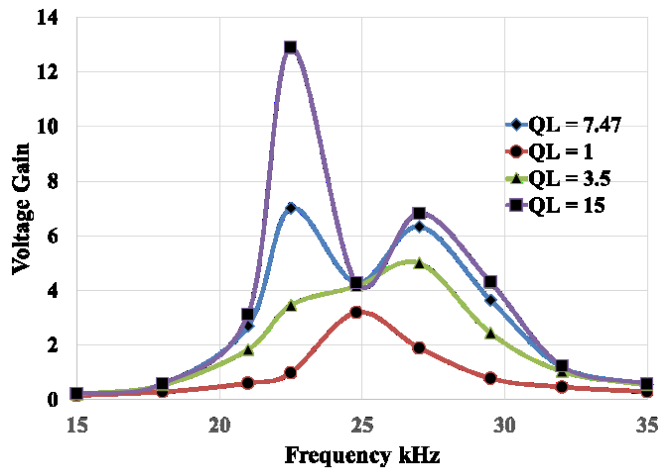


Fig. 5.1 SP Voltage gain characteristics

It is clear that for the SP system to give unity voltage gain, we should operate the converter at 50% duty cycle at either ~ 20 kHz or ~ 30.5 kHz which gives an advantage of zero current and zero voltage switching respectively. However from equation (2.32), at higher frequencies and fixed input voltage, the tank currents are very high, also IGBTs cannot be used at higher frequencies. It is seen that operating at 19.5 kHz, due to more circulating currents, the efficiency numbers are very less. Hence there needs to be a control scheme to achieve unity voltage gain at higher operating efficiency.

Table-5.1 System design specifications

Parameter	Value
Primary Inductance L_p	125 μ H
Secondary Inductance L_s	125 μ H
Mutual Inductance @ 10 cm airgap	29 μ H
Tank Frequency	24780 Hz
Primary capacitor C_p	0.33 μ F
Secondary capacitor C_s	0.33 μ F
Input DC link voltage	400 VDC
Required output DC voltage	400 VDC
Output Power P_L	1000 W
Load resistance R_L	160 Ω
Quality factor Q_L	7.47

5.1 Fixed Frequency (ω_o) Firing Angle Control

In the fixed frequency firing angle control method, the fundamental component of the input voltage to the primary resonant tank is controlled in the class-D inverter to achieve the unity voltage gain. Two controls are presented for achieving the required unity gain design; $\alpha\alpha$ -DB control and α -DB- α control.

5.1.1. $\alpha\alpha$ -DB control

This control is better understood with the help of the circuit operation and waveforms as shown in Fig. 5.2. As the name suggests, in $\alpha\alpha$ -DB control switch S1 and switch S2 are turned on for 0 to α and α to 2α respectively, and from 2α to 360° , there will be a dead band and no active device conduction, only body diode conducts during this time.

The operation of the converter is explained in different modes of operation as shown below;

Mode-1 ($t_0 < t < t_1$): In this mode of operation, switch S1 is turned on, which gives $V_{inv} = V_{in}$. During this mode, the current through primary inductor increases and it gets charged.

Mode-2 ($t_1 < t < t_2$): Here, S1 is turned off and S2 is turned on. During this mode $V_{inv}=0$ and the inductor will discharge through S1 and this supplies the load power till 2α while charging primary capacitor.

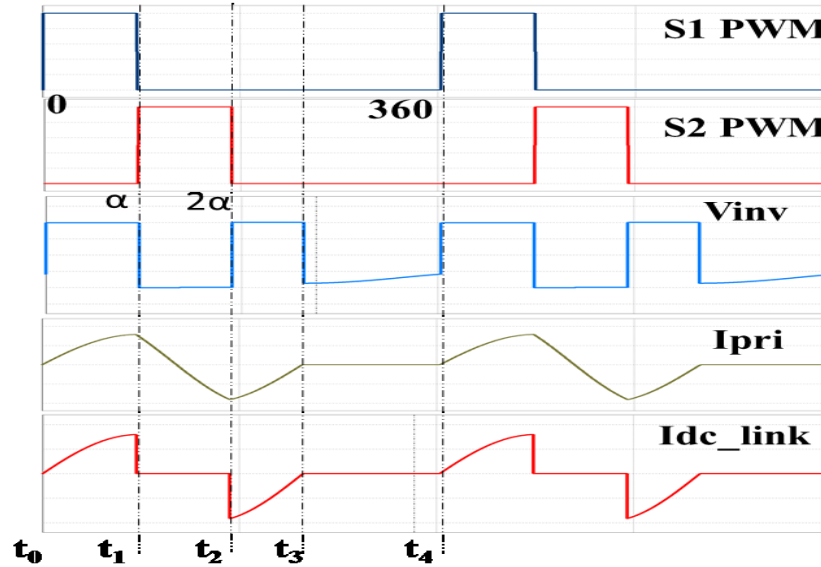


Fig. 5.2 $\alpha\alpha$ -DB control operating waveforms

Mode-3 ($t_2 < t < t_3$): Here, switch S2 is turned off. As the inductor is fully discharged, now primary capacitor will discharge in the opposite direction to inductor discharge. The capacitor finds the path through D1 and source. Hence the $V_{inv} = V_{in}$.

Mode-4 ($t_3 < t < t_4$): Here the energy stored in the primary inductor and capacitor are completely discharged. The operation now will be due to the secondary stored tank energy. The unknown voltage V_{inv} level is due to secondary current.

Doing FFT for the V_{inv} , we get the fundamental component of the inverter voltage responsible for the power transfer. From the known factors, and using equation (2.34), we can obtain the output voltage V_{out} . FFT is done to obtain the input voltage fundamental component necessary for obtaining desired V_{out} for any given design. Thus we can get required α value. For the design specifications as given in Table-5.1, required $\alpha = 111^\circ$.

5.1.2. α -DB- α control

As the name suggests, in α -DB- α control switch S1 and switch S2 are turned on for 0 to α and 180° to $180^\circ + \alpha$ respectively, and from α to 180° and $180^\circ + \alpha$ to 360° , there will be a dead band as shown in the Fig. 5.3. The operation of the converter with α -DB- α control is explained as;

Mode-1 ($t_0 < t < t_1$): In this mode of operation, switch S1 is turned on, which enables $V_{inv} = V_{in}$. During this mode, the current through primary inductor increases and it gets charged.

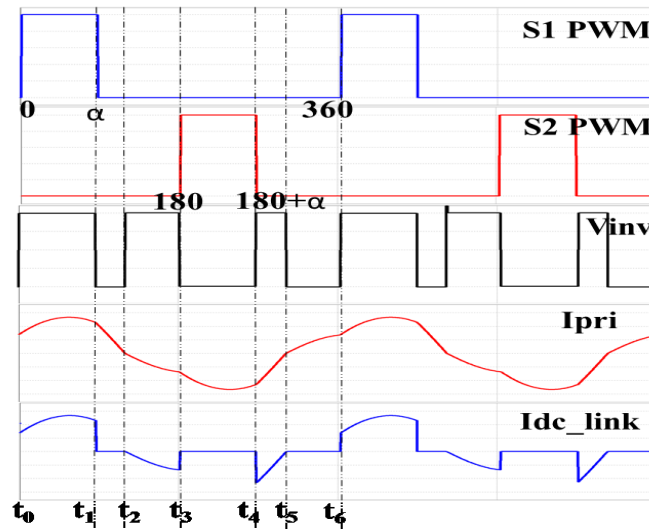


Fig. 5.3 α -DB- α control operating waveforms

Mode-2 ($t_1 < t < t_2$): Here, S1 is turned off. During this mode $V_{inv} = 0$ and the primary inductor will discharge till the current reaches zero at t_2 .

Mode-3 ($t_2 < t < t_3$): Here, the primary capacitor will be dominant and discharges via D1 and source till the switch S2 is turned on. Therefore, $V_{inv} = V_{in}$.

Mode-4 ($t_3 < t < t_4$): In this mode, switch S2 is turned on, primary capacitor find its discharge path through S2. Capacitor discharges till S2 is turned off. During this mode, the primary inductor is also being charged.

Mode-5 ($t_4 < t < t_5$): Soon as the S2 is turned off, primary inductor will discharge through D1 and source till the capacitor gets charged to source voltage. Therefore, here $V_{inv} = V_{in}$.

Mode-5 ($t_5 < t < t_6$): In this mode the capacitor will discharge through diode D2 and charges the primary inductor. This mode continues till the switch S1 is turned on.

As discussed in previous control method, doing FFT for the V_{inv} , we get the fundamental component of the inverter voltage responsible for the power transfer to the secondary. From the known factors, and using equation (2.34), we can obtain the output voltage V_{out} . FFT is done to obtain the input voltage fundamental component necessary for obtaining desired V_{out} for any given design. Thus we can get required α value. For the design specifications as given in Table-5.1, required $\alpha = 86^\circ$.

5.2. Results and Comparison

Non-ideal SPICE simulation is carried out with practical component ratings for design specifications as given in Table-5.1. Simulation are done with variable frequency (VF) and fixed duty cycle at 50% on both inductive region (30.25 kHz) and capacitive region (20.3 kHz). Also fixed frequency (FF) 24.8 kHz, α -DB control and α -DB- α control conditions are simulated. Table-5.2 summarizes the simulation results for a 1000 W load power.

Table-5.2 Simulation Results For Achieving Unity Voltage Gain.

Control Technique	DC link current	Primary tank current	Secondary tank current	Load Voltage	Load current
(A) VF Control, fixed duty cycle (30.25 kHz)	3.17 A	37 A	21.2 A	401.5 V	2.76 A
(B) VF Control, fixed duty cycle (20.3 kHz)	3.02 A	27 A	15.3 A	400 V	2.58 A
(C) FF (24.8 kHz) α -DB control	2.91 A	17.5 A	17.8 A	400 V	2.75 A
(D) FF (24.8 kHz) α -DB- α control	2.9 A	16.7 A	17.6 A	400 V	2.75 A

The efficiency versus power transfer plots for various control schemes as shown in the Table-6.2 are shown in Fig. 5.4.

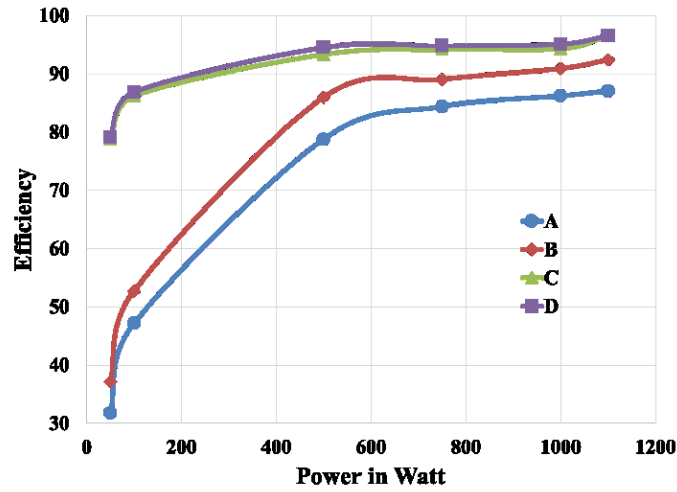


Fig. 5.4 Power transfer efficiency plot with different control schemes

5.3 Conclusion

Series-Parallel compensated wireless inductive power transfer system driven by Class-D amplifier circuit is analyzed and various control schemes are explained for achieving unity voltage gain. From the SPICE simulation results using non-ideal components, it is understood that the fixed frequency $\alpha\alpha$ -DB and α -DB- α control schemes gives the best efficiency for wide range of operation. α -DB- α control gives us the better efficiency as it has less device conduction time compared to other control schemes.

A combined use of fixed frequency control with firing angle control can also be used for achieving ZVS or ZCS. Here, frequency is fixed either above the resonant frequency or below the resonant frequency depending on which soft switching is required.

Chapter-6 Wireless charging of an IEV

Electric vehicles and plug-in hybrid electric vehicles are becoming the next generation transportation replacing the internal combustion engine vehicles as they produce zero tail pipe emissions, more efficient and less noisy. IEVs like fork lifts, stock chasers, golf-karts, sports ATVs, snowmobiles, airport cargo trucks, etc., have existed in market much before the present day electric cars. All the EVs and PHEVs have battery packs that are charged using an on-board or off-board charging equipment. On-board charging can be done using a contact based [3]–[6] or contact less charging [7]–[11]. IEVs uses a 24 VDC to 48 VDC battery packs on-board vehicle. In a commonly used IEV on-board conductive charger topology, an isolated transformer is used both in hard-switching and soft-switching topologies. With the use of wireless charging technology, the power transfer system inherently possess a galvanic isolation. As the IEVs have battery pack voltage in the range of 24 to 48 VDC, it is very cost effective and efficient to use wireless charging without any additional isolation in the design. Wireless charging is possible using electromagnetic power transfer and electro static power transfer [22],[23]. In a WRIPT system, power is transferred from the primary to secondary through a large airgap using high frequency magnetic field. The novel U-U core WRIPT system as seen in chapter-4 is considered for the design of an IEV charging system without using extra isolation transformer. A Class-D amplifier is selected as the high frequency inverter topology for its reduced components, power handling capacity and easy control. Due to unique WRIPT voltage gain characteristics, we need to employ control techniques as discussed in Chapter-5 to charge a 24 VDC to 48 VDC IEV from the most commonly used 400 V APFC DC link stage. For simplicity sake, the output is loaded with a resistor after the rectification in the simulations. It is very simple to control the battery charging from the primary side control. Also once we have a rectified DC voltage on the secondary, it is easy to control the battery charging by cascading a DC to DC converter on the secondary.

In this chapter, SS and SP compensated WRIPT systems are simulated with the specifications as listed in the Table-6.1. As discussed in the chapter-5, we can control the class-D inverter circuit for obtaining required system voltage gain. For charging a 48 V battery pack, here we use fixed frequency duty cycle control for a class-D amplifier circuit and the system is simulated with non-

ideal components with the specifications from Table-6.1. For achieving ZVS, a frequency little over the resonant frequency is chosen to be fixed for WRIPT system.

Table-6.1 Specification for IEV charging using WRIPT

Parameter	Specification
Primary inductance L_{pri}	125 μ H
Secondary inductance L_{sec}	125 μ H
Mutual inductance	29 μ H
Tank frequency	24.780 kHz
DC link input voltage	400 VDC
Max. output rectifier voltage	56 VDC
Switching frequency	25.500 kHz
Load resistance	@ 1 kW = 3 Ω

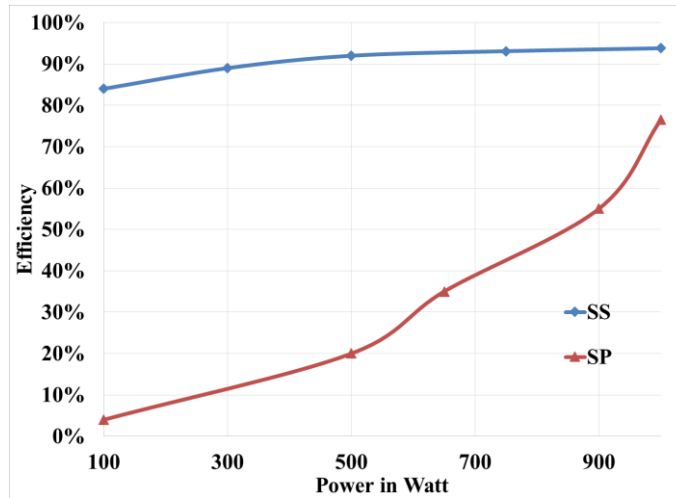


Fig. 6.1 Efficiency vs Load power for IEV charging

The primary current in SP compensated WRIPT system is given as

$$i_p = \frac{j\omega L_s \cdot i_s + V_{out}}{j\omega M} \quad \text{and} \quad i_s = i_L + i_{C_s} = \frac{V_{out}}{R_L} + j\omega C_s \cdot V_{out} \quad (6.a)$$

With the non-ideal simulation results, the input DC to output DC stage efficiency versus load power is plotted as shown in Fig. 6.1. It is seen that the SS compensated WRIPT system is more efficient for IEV charging than SP compensated WRIPT system. Low efficiency in SP WRIPT system for IEV charging is due to very large primary current. The primary current as seen from (6.a) will be affected when the load resistance is very small as in case of IEV charging. Therefore for low voltage gain applications like IEV charging, SS compensated WRIPT system is very efficient.

Chapter-7 Conclusion and Future Work

Conclusion

Ferrite core based magnetic power transfer systems like E-E, E-I, ETD-ETD, Planar-E core, U-I, U-U combinations have been evaluated for wireless resonant inductive power transfer applications. Initial investigations on aforementioned systems indicate that the U-I and U-U core combinations better suites the requirement of WRIPT applications. Further investigations using FEA analysis and experiments were carried out on U-I and U-U cores with split windings. These indicate that the U-U core with split winding wound on side limbs and connected in parallel and series on the primary and secondly respectively performs very well in misalignment and large airgap scenarios. From the results, it is understood that the minimum pole to pole spacing required for an efficient power transfer is 2 times the design airgap.

A novel magnetic power transfer system is designed for a 1.0 kW power transfer and 10 cm airgap. Electrical model for the system is developed and simulation results obtained were very closely matching with experimental results. The system is experimented and tested with two design scenarios where $L_{pri} = L_{sec}$ and $L_{pri} > L_{sec}$. From the experimental results on final design, it is seen that the system with $L_{pri} = L_{sec}$ operates at a the DC to DC efficiency of 94.7% at 10 cm airgap and 91% at 10 cm airgap and 5 cm misalignment.

However for the system with $L_{pri} > L_{sec}$, the performance of the system is very poor. This is due to the below facts;

- a. The mutual inductance is very low due to low secondary inductance.
- b. As secondary capacitance value is larger for maintaining the input tank frequency due to the inductance imbalance condition, the secondary tank current is very large.
- c. As a result of secondary larger current, and low mutual inductance, the primary current is also considerably larger than that we saw in the case of $L_{pri} = L_{sec}$.
- d. As a result of point 'c', the device current is also high.
- e. Above all larger currents are resulting in high Ohmic losses in the system which is the main reason for loss of efficiency.

Magnetic radiation is also measured while conducting experiments using a magnetometer and observed that the magnetic radiation results are well within the safety limits posed by the WRIPT charging standards.

Class-D inverter control is understood and for designing the system with unity voltage gain using SP compensated WRIPT system. PSIM simulations are carried out on various control methods for achieving 400 VDC input to 400 VDC output using SP WRIPT system. From the fixed frequency and variable frequency control options, the fixed frequency operation is seen to be more efficient. In particular fixed frequency α -DB- α control schemes gives the best efficiency for wide range of operation. α -DB- α control gives us the better efficiency as it has less device conduction time compared to other control schemes.

A 48 V, 1.0 kW IEV charging system is simulated for the final U-U core system design specifications using class-D converter with fixed frequency α -DB- α control. It is simulated using SS and SP compensated WRIPT systems. From the non-ideal component simulation results, it is seen that the SS system can charge an IEV with 48 V battery pack more efficiently than an SP system. Therefore, to charge an IEV or for transferring power with very low voltage gain, it is wise to design SS compensated WRIPT system.

Future Work

Since this work is very novel, there is a lot of scope for improvement and many things should be investigated. The designed system is considered only for the proof of concept. Future work can be extended but not limited to the below points;

1. To optimize the magnetic system design and test for better higher efficiencies for airgap vs pole to pole spacing.
2. To investigate the winding pitch and length of winding spread on the core limbs vs its effect on mutual inductance and the leakage flux.
3. To investigate the effect of area of cross section in maximizing the mutual inductance in the system.

4. To investigate and mathematically prove why the primary parallel winding and secondary series winding configuration is more efficient than the counterparts.
5. To investigate WIPT compensation techniques like LCC and double side LCC which were recently presented in the literature on this novel magnetic system.
6. To investigate and identify the key factors that play a major role in reducing the magnetic radiation for the designed novel system.
7. To investigate how coil span, coil spread length on the limb and number of turns are affecting the magnetic radiation.
8. Investigating the magnetic radiation for higher power levels for fast charging applications using this novel magnetic system design.

References

- [1] D. Naunin, “Electric Vehicle,” *Proc. IEEE Int. Symp. Ind. Electron.*, vol. 1, pp. 11–24, 1996.
- [2] K. Rajashekara, “Present Status and Future Trends in Electric Vehicle Propulsion Technologies,” *IEEE J. Emerg. Sel. Top. Power Electron.*, vol. 1, no. 1, pp. 3–10, 2013.
- [3] S. Li, J. Deng, and C. C. Mi, “Single-stage resonant battery charger with inherent power factor correction for electric vehicles,” *IEEE Trans. Veh. Technol.*, vol. 62, no. 9, pp. 4336–4344, 2013.
- [4] B. Gu, S. Member, J. Lai, and N. Kees, “Hybrid-Switching Full-Bridge DC – DC Converter With Minimal Voltage Stress of Bridge Rectifier , Reduced Circulating Losses , and Filter Requirement for Electric Vehicle Battery Chargers,” vol. 28, no. 3, pp. 1132–1144, 2013.
- [5] B. Gu, C. Y. Lin, B. F. Chen, J. Dominic, and J. S. Lai, “Zero-voltage-switching PWM resonant full-bridge converter with minimized circulating losses and minimal voltage stresses of bridge rectifiers for electric vehicle battery chargers,” *IEEE Trans. Power Electron.*, vol. 28, no. 10, pp. 4657–4667, 2013.
- [6] A. Khaligh and S. Dusmez, “Comprehensive topological analysis of conductive and inductive charging solutions for plug-in electric vehicles,” *IEEE Trans. Veh. Technol.*, vol. 61, no. 8, pp. 3475–3489, 2012.
- [7] D. J. Thrimawithana and U. K. Madawala, “A generalized steady-state model for bidirectional ipt systems,” *IEEE Trans. Power Electron.*, vol. 28, no. 10, pp. 4681–4689, 2013.
- [8] J. M. Miller, O. C. Onar, and M. Chinthavali, “Primary-Side Power Flow Control of Wireless Power Transfer for Electric Vehicle Charging,” *IEEE J. Emerg. Sel. Top. Power Electron.*, vol. 3, no. 1, pp. 147–162, 2015.
- [9] J. M. Miller, P. T. Jones, J.-M. Li, and O. C. Onar, “ORNL Experience and Challenges Facing Dynamic Wireless Power Charging of EV’s,” *IEEE Circuits Syst. Mag.*, vol. 15, no. 2, pp. 40–53, 2015.
- [10] S. Li and C. Mi, “Wireless Power Transfer for Electric Vehicle Applications,” *Emerg. Sel. Top. Power Electron. IEEE J.*, vol. PP, no. 99, p. 1, 2014.

- [11] J. Deng, S. Member, F. Lu, and T. Nguyen, “Development of a High Efficiency Primary Side Controlled 7kW Wireless Power Charger,” 2014.
- [12] “Wikipedia (english) http://en.wikipedia.org/wiki/James_Clerk_Maxwell (2012-01-26).”
- [13] “Wikipedia (english) http://en.wikipedia.org/wiki/Oliver_Heaviside (2012-01-26).”
- [14] “Wikipedia (english) http://en.wikipedia.org/wiki/Nicola_Tesla (2012-01-26).”
- [15] “Wikipedia. (Updated: March 19, 2006) ‘Wireless energy transfer’ Wikimedia Foundation, Inc. http://en.wikipedia.org/wiki/Wireless_energy_transfer,” *Wikipedia. (Updated March 19, 2006) “Wireless energy Transf. Wikimedia Found. Inc. Http://en.wikipedia.org/wiki/wireless_energy_trans.*
- [16] “Cynthia Boyko & Stu McCormick. (Updated: February 6, 2001). by Friends of CRC, <http://www.friendsofrc.ca/Projects/SHARP/sharp.html>.”
- [17] A. L. Spring, “INTRODUCING WIRELESS CHARGING Charge where you are,” 2015.
- [18] K. W. Klontz, D. M. Divan, D. W. Novotny, and R. D. Lorenz, “Contactless power delivery system for mining applications,” *Ind. Appl. IEEE Trans.*, vol. 31, no. 1, pp. 27–35, 1995.
- [19] G. Roberts, P. Hadfield, M. E. Humphries, F. Bauder, and J. M. G. Izquierdo, “Design and evaluation of the power and data contactless transfer\ndevice,” *1997 IEEE Aerosp. Conf.*, vol. 3, pp. 523–533, 1997.
- [20] “<http://www.electric-vehiclenews.com/2015/08/uk-to-test-dynamic-wireless-charging.html>.”
- [21] C. Mi, D. Ph, and F. Ieee, “Development of an Extremely Efficient Wireless EV Charger Definition of Wireless Power,” pp. 1–22.
- [22] J. Dai, S. Member, and D. C. Ludois, “A Survey of Wireless Power Transfer and a Critical Comparison of Inductive and Capacitive Coupling for Small Gap Applications,” *IEEE Trans. Power Electron.*, vol. 30, no. 11, pp. 6017–6029, 2015.
- [23] J. Dai, S. Member, D. C. Ludois, and M. Ieee, “Wireless Electric Vehicle Charging via Capacitive Power Transfer Through a Conformal Bumper,” pp. 3307–3313, 2015.
- [24] J. T. H. Sergio Ramos, George R. Woody, Ray G. Radys, “Inductive charging system employing a fluid-cooled transformer coil and transmission cable,” *US Patents# US6396241 B1*, vol. 2, no. 12, 2002.
- [25] R. D. L. Keith W. Klontz, Deepakraj M. Divan, Donald W. Novotny, “Contactless battery

charging system,” *US Patents# US5341083 A*, pp. 0–4, 1984.

- [26] I. S. Suh and J. Kim, “Electric vehicle on-road dynamic charging system with wireless power transfer technology,” *Proc. 2013 IEEE Int. Electr. Mach. Drives Conf. IEMDC 2013*, pp. 234–240, 2013.
- [27] S. Jeong, Y. J. Jang, and D. Kum, “Economic Analysis of the Dynamic Charging Electric Vehicle,” *IEEE Trans. Power Electron.*, vol. 30, no. 11, pp. 6368–6377, 2015.
- [28] S. Lukic and Z. Pantic, “Cutting the Cord: Static and Dynamic Inductive Wireless Charging of Electric Vehicles,” *IEEE Electrif. Mag.*, vol. 1, no. 1, pp. 57–64, 2013.
- [29] C. Manolatos, M. J. Khan, S. Fan, P. R. Villeneuve, H. A. Haus, and J. D. Joannopoulos, “Coupling of modes analysis of resonant channel add-drop filters,” *IEEE J. Quantum Electron.*, vol. 35, no. 9, pp. 1322–1331, 1999.
- [30] A. Pevere and R. Petrella, “Design of a high efficiency 22 kW wireless power transfer system for EVs fast contactless charging stations.”
- [31] W. Li, M. Tabaddorl, C. Mi, U. L. Llc, P. Road, and N. Il, “Optimization and Safety Evaluation of a 3 . 3 kW Wireless EV Charger,” 2015.
- [32] H. H. Wu, A. Gilchrist, K. D. Sealy, and D. Bronson, “A high efficiency 5 kW inductive charger for EVs using dual side control,” *IEEE Trans. Ind. Informatics*, vol. 8, no. 3, pp. 585–595, 2012.
- [33] H. Sakamoto, K. Harada, Y. Matsuo, and F. Nakao, “Large Air-Gap Coupler for Inductive Charger,” vol. 35, no. 5, pp. 3526–3528, 1999.
- [34] C. Qiu, K. T. Chau, T. W. Ching, and C. Liu, “Overview of Wireless Charging Technologies for Electric Vehicles,” *J. Asian Electr. Veh.*, vol. 12, no. 1, pp. 1679–1685, 2014.
- [35] J. M. Miller, O. C. Onar, C. White, S. Campbell, C. Coomer, L. Seiber, R. Sepe, and A. Steyerl, “Demonstrating Dynamic Wireless Charging of an Electric Vehicle,” *IEEE Power Electron. Mag.*, no. March, 2014.
- [36] D. Sadarnac, S. Loudot, A. Caillierez, and A. Jaafari, “Dynamic inductive charging for electric vehicle: modelling and experimental results,” *7th IET Int. Conf. Power Electron. Mach. Drives (PEMD 2014)*, pp. 1.7.01–1.7.01, 2014.
- [37] T. Loewel, C. Lange, and F. Noack, “Identification and positioning system for inductive

- charging systems,” *2013 3rd Int. Electr. Drives Prod. Conf. EDPC 2013 - Proc.*, pp. 1–5, 2013.
- [38] Z. Cheng, Y. Lei, K. Song, and C. Zhu, “Design and Loss Analysis of Loosely Coupled Transformer for an Underwater High-power Inductive Power Transfer System,” *IEEE Trans. Magn.*, vol. 9464, no. c, pp. 1–1, 2014.
- [39] T. Nagashima, X. Wei, E. Bou, S. Member, E. Alarcón, S. Member, and M. K. Kazimierczuk, “Analysis and Design of Loosely Inductive Coupled Wireless Power Transfer System Based on Class- DC-DC Converter for Efficiency Enhancement,” vol. 62, no. 11, pp. 2781–2791, 2015.
- [40] C. R. Sullivan, “Optimal choice for number of strands in a litz-wire transformer winding,” *IEEE Trans. Power Electron.*, vol. 14, no. 2, pp. 283–291, 1999.
- [41] O. H. Stielau and G. a Covic, “Design of loosely coupled inductive power transfer systems,” *Power Syst. Technol. 2000. Proceedings. PowerCon 2000. Int. Conf.*, vol. 1, pp. 85–90 vol.1, 2000.
- [42] G. Elliott and J. Boys, “Magnetically coupled systems for power transfer to electric vehicles,” *Drive Syst. 1995.*, no. 95, 1995.
- [43] T. Bieler, M. Perrottet, V. Nguyen, and Y. Perriard, “Contactless Power and Information Transmission,” *Ind. Appl.*, vol. 38, no. 5, pp. 1266–1272, 2002.
- [44] A. Esser, H. C. Skundenly, and H.-C. Skudelny, “A New Approach to Power Supplies for Robots,” *IEEE Trans. Ind. Appl.*, vol. 27, no. 5, pp. 872–875, 1991.
- [45] K. Yamamoto, T. Maruyama, K. Kondo, and T. Kashiwagi, “A Study on the circuit configuration with capacitors to compensate the power factor for high-power contactless power transformer,” *2013 Int. Conf. Electr. Mach. Syst.*, pp. 2233–2238, 2013.
- [46] N. Jamal, S. Saat, and A. Z. Shukor, “A study on performances of different compensation topologies for loosely coupled inductive power transfer system,” *Proc. - 2013 IEEE Int. Conf. Control Syst. Comput. Eng. ICCSCE 2013*, vol. 2, no. 1, pp. 173–178, 2013.
- [47] K. Aditya and S. S. Williamson, “Comparative study of Series-Series and Series-Parallel compensation topologies for electric vehicle charging,” *IEEE Int. Symp. Ind. Electron.*, pp. 426–430, 2014.
- [48] Y.-X. Guo and R. Jegadeesan, “Efficient Inductive Power Transfer for biomedical

- applications,” *2012 IEEE Int. Work. Electromagn. Appl. Student Innov. Compet.*, no. 6, pp. 1–2, 2012.
- [49] J. Deng and S. Member, “Magnetic Integration of LCC Compensated Resonant Converter for Inductive Power Transfer Applications,” *Energy Convers. Congr. Expo.*, pp. 660–667, 2014.
- [50] F. Lu and H. Hofmann, “Output Power and Efficiency Sensitivity to Circuit Parameter Variations in Double-Sided LCC- Compensated Wireless Power Transfer System,” pp. 597–601, 2015.
- [51] W. Li, C. C. Mi, S. Li, J. Deng, T. Kan, and H. Zhao, “Integrated LCC Compensation Topology for Wireless Charger in Electric and Plug-in Electric Vehicles,” *IEEE Trans. Ind. Electron.*, vol. 0046, no. c, pp. 1–1, 2015.
- [52] M. Budhia, G. a. Covic, and J. T. Boys, “Design and optimization of circular magnetic structures for lumped inductive power transfer systems,” *IEEE Trans. Power Electron.*, vol. 26, no. 11, pp. 3096–3108, 2011.
- [53] H. Son, J. Kim, Y. Park, and K. Kim, “Efficiency Analysis and Optimal Design of a Circular Loop Resonant Coil for Wireless Power Transfer,” no. L, pp. 849–852, 2010.
- [54] R. Bosshard, J. Muhlethaler, J. W. Kolar, and I. Stevanovic, “Optimized magnetic design for inductive power transfer coils,” *Conf. Proc. - IEEE Appl. Power Electron. Conf. Expo. - APEC*, no. Apec, pp. 1812–1819, 2013.
- [55] S. Mutashar, M. a. Hannan, S. a. Samad, and A. Hussain, “Design of Spiral Circular Coils in Wet and Dry Tissue for Bio-Implanted Micro-System Applications,” *Prog. Electromagn. Res.*, vol. 32, no. August, pp. 181–200, 2013.
- [56] S. Mutashar, M. A. Hannan, S. A. Samad, and A. Hussain, “Analysis and optimization of spiral circular inductive coupling link for bio-implanted applications on air and within human tissue,” *Sensors (Switzerland)*, vol. 14, no. 7, pp. 11522–11541, 2014.
- [57] P. Schumann, T. Diekhans, O. Blum, U. Brenner, A. Henkel, and R. B. Gmbh, “Compact 7 kW Inductive Charging System with Circular Coil Design,” 2015.
- [58] A. Manuscript and W. P. Transmission, “NIH Public Access,” no. IMD, 2012.
- [59] H. Takanashi, Y. Sato, Y. Kaneko, S. Abe, and T. Yasuda, “A large air gap 3 kW wireless power transfer system for electric vehicles,” *2012 IEEE Energy Convers. Congr. Expo.*

ECCE 2012, pp. 269–274, 2012.

- [60] M. Chigira, Y. Nagatsuka, Y. Kaneko, S. Abe, T. Yasuda, and A. Suzuki, “Small-size lightweight transformer with new core structure for contactless electric vehicle power transfer system,” *IEEE Energy Convers. Congr. Expo. Energy Convers. Innov. a Clean Energy Futur. ECCE 2011, Proc.*, pp. 260–266, 2011.
- [61] T. D. Nguyen, S. Li, W. Li, and C. C. Mi, “Feasibility study on bipolar pads for efficient wireless power chargers,” *Conf. Proc. - IEEE Appl. Power Electron. Conf. Expo. - APEC*, pp. 1676–1682, 2014.
- [62] W. Zhang, S. C. Wong, C. K. Tse, and S. Member, “A Novel Transformer for Contactless Energy Transmission Systems Qianhong Chen Xinbo Ruan,” *Flux*, no. 29, pp. 3218–3224, 2009.
- [63] C. Fernandez, O. Garcia, R. Prieto, J. a. Cobos, S. Gabriels, and G. Van Der Borcht, “Design issues of a core-less transformer for a contact-less\application,” *APEC. Seventeenth Annu. IEEE Appl. Power Electron. Conf. Expo. (Cat. No.02CH37335)*, vol. 1, no. 1, pp. 339–345, 2002.
- [64] A. Zaheer, H. Hao, G. A. Covic, and D. Kacprzak, “Investigation of multiple decoupled coil primary pad topologies in lumped IPT systems for interoperable electric vehicle charging,” *IEEE Trans. Power Electron.*, vol. 30, no. 4, pp. 1937–1955, 2015.
- [65] W. Zhang, S. Member, J. C. White, A. M. Abraham, and C. C. Mi, “Loosely Coupled Transformer Structure and Interoperability Study for EV Wireless Charging Systems,” vol. 30, no. 11, pp. 6356–6367, 2015.
- [66] M. Budhia, J. T. Boys, G. A. Covic, and C. Y. Huang, “Development of a single-sided flux magnetic coupler for electric vehicle IPT charging systems,” *IEEE Trans. Ind. Electron.*, vol. 60, no. 1, pp. 318–328, 2013.
- [67] H. Hsieh, T. Huang, and S. Shih, “An Inductive Wireless Charger for Electric Vehicle by using LLC Resonance with Matrix Ferrite Core Group,” pp. 1637–1643, 2015.
- [68] M. Definition, “E-Core Transformer,” pp. 1–34.
- [69] A. J. M. Flat and P. Grove, “Models of Simple Iron Cored Electromagnets,” no. Rectangle 2, 2014.
- [70] G. Tao, C. Liu, Y. Diao, X. Zhang, and B. Pi, “Design and Implementation of Inductive

Coupling Power Transfer Device Based on Structural Parameters Analysis,” *Int. J. u- e- Serv. Sci. Technol.*, vol. 6, no. 5, pp. 67–78, 2013.

- [71] “Ferrocube 3F3 Material,” <http://www.ferrocube.com/FerrocubeCorporateReception/datasheet/3f3.pdf>, no. October, 2008.

Annexure-I

System Power Loss Calculations

Consider the loss modelled circuit diagram of the WRIPT system as shown below. R_{1sat} and R_{2sat} are the resistors modelled for the IGBT saturation voltage. Capacitors have an equivalent series resistance ESR which will cause the Ohmic losses. Also the primary and secondary coils have Ohmic losses due to the coil resistances. Diode forward drop can be modelled using resistors as $R_{fd1} \dots 4$.

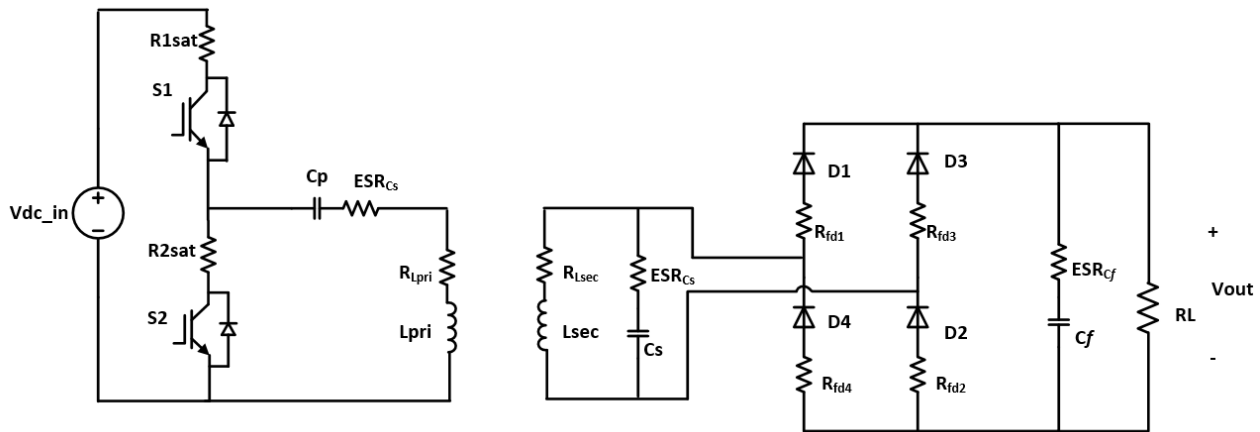


Fig. Loss modelled system circuit

The main reasons for the power loss in the WRIPT system are

- i) Switching and conduction losses in the high frequency inverter.
- ii) Ohmic loss in primary compensation capacitor and the primary coil.
- iii) Ohmic losses in the secondary compensation capacitor and secondary coil.
- iv) Switching and conduction loss in the secondary side high frequency diode bridge rectifier.
- v) Ohmic loss in the output filter capacitor.

From the known parameters in the case of $L_{pri}=L_{sec}$, we can compute the power loss in the system for each of the case shown above

i) Switching and conduction losses in the high frequency inverter.

a) Switching losses

Switching losses in the IGBTs are the turn on and turn off losses. Due to the overlap of the rising and falling slope in the IGBT voltage, at high switching frequency, it causes power losses as shown below.

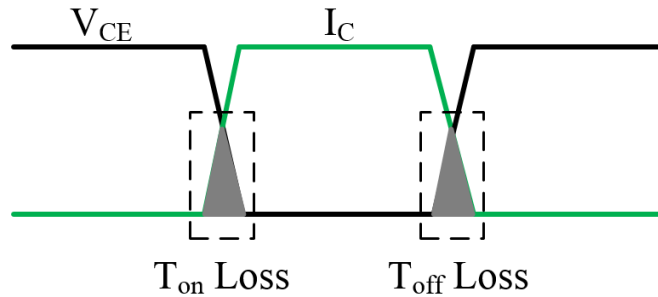


Fig. IGBT switching losses

Also due to zero current switching, the turn off losses are almost eliminated.

In the experimental verification as discussed in the chapter-4, a dead band of 750 ns is introduced in the IGBT switching between the switch S1 and S2. This will reduce switching losses between the switching transition between switches S1 and S2.

Therefore only turn ON losses are present in the system.

b) Conduction losses

From the IGBT datasheet, for the average DC link current of 6.9 A, saturation voltage is ~1.35 V.

For simplicity sake, diode conduction is neglected and the total conduction duration is considered to be for IGBT.

Therefore the conduction losses are $2 \times 6.9 \times 1.35 = 18.63$ W.

ii) Ohmic loss in primary compensation capacitor and the primary coil.

The ESR of primary capacitor as per capacitor datasheet is 13 m Ω and the primary tank rms current is 18 A.

Therefore, the Ohmic loss is $(18)^2 \times 0.013 = 4.2$ W

The primary coil resistance is found to be 30 mΩ, and for primary rms current of 18 A, the Ohmic loss is $18^2 \cdot 0.03 = 9.72$ W.

iii) Ohmic losses in the secondary compensation capacitor and secondary coil.

The ESR of secondary capacitor as per capacitor datasheet is 13 mΩ and the primary tank rms current is 15.2 A.

Therefore, the Ohmic loss is $(15.2)^2 \cdot 0.013 = 3$ W

The primary coil resistance is found to be 30 mΩ, and for primary rms current of 15.2 A, the Ohmic loss is $15.2^2 \cdot 0.03 = 7$ W.

iv) Switching and conduction loss in the secondary side high frequency diode bridge rectifier.

For 3A average current, the diode drop from the datasheet is 0.85 V. Ohmic loss in the diode bridge can be calculated as $2 \cdot (3 \cdot 0.85) = 5.1$ W

v) Ohmic loss in the output filter capacitor.

The ESR of filter capacitor as per capacitor datasheet is 33 mΩ and the average current flowing through it is 1.6 A.

The ohmic loss is calculated as $16^2 \cdot 0.033 =$ almost zero.

Now the total loss can be sum of all the above losses, which is ~48 W.

Load power is 1040 W.

Total input power is $1040 + 48 = 1088$ W

Total efficiency is $1040/1088 = 95.5\%$

We have seen that the experimental efficiency is 94.7%, however the computed efficiency is 65.5%. The difference in the efficiency number is due to the the neglected switching losses in the high frequency diode bridge and the turn on losses in the high frequency inverter. Form the calculations, we see that the inverter has more conduction losses. We can reduce this using SiC or GaN devices in the inverter. Also optimizing the coils on primary and secondary, we can reduce the Ohmic losses in the coils.